Department
Chemie und Pharmazie

Friedrich-Alexander-Universität
Naturwissenschaftliche Fakultät

Dehydrogenation of liquid organic hydrogen carriers under model catalytic conditions on Ni(111) and Pt(111)

Dehydrierung von Wasserstoffspeichermolekülen unter modellkatalytischen Bedingungen auf Ni(111) und Pt(111)

Der Naturwissenschaftlichen Fakultät
der Friedrich-Alexander-Universität Erlangen-Nürnberg
zur Erlangung des Doktorgrades Dr. rer. nat.

vorgelegt von

Johann Steinhauer

aus Tschimkent

Als Dissertation genehmigt von der Naturwissenschaftlichen Fakultät
der Friedrich-Alexander-Universität Erlangen-Nürnberg

Tag der mündlichen Prüfung:	20.09.2022
Vorsitzender des Promotionsorgans:	Prof. Dr. Wolfgang Achtziger
Gutachter:	PD Dr. Christian Papp
	Prof. Dr. Peter Wasserscheid

Table of contents

1. Introduction

As of today, carbon-based fossil fuels like oil, coal and natural gas are the main driver of the global economy. Fossil fuels exhibit relatively high energy densities and are available in different aggregate states, offering energy for various applications. They are used in combustion engines to propel vehicles, in power plants for the production of electricity, or for heating. As the global population is expected to grow to 9.6 -12.3 billion people[1] in 2100, the demand for primary energy is also expected to remain on a steep upward trajectory. Moreover, urbanization further increases the trend for higher energy consumption.[2]

Non-renewable energy sources, however, are responsible for the emission of greenhouse gases, which in turn are responsible for global warming and extreme weather phenomena.[3-9] The impact of greenhouse gases like CO_2 on global warming and the environment is studied and documented extensively. The global emission of carbon dioxide from 1965 to 2020 is presented in Figure 1.[10] Except during economic recessions, carbon dioxide emissions increased in all periods.

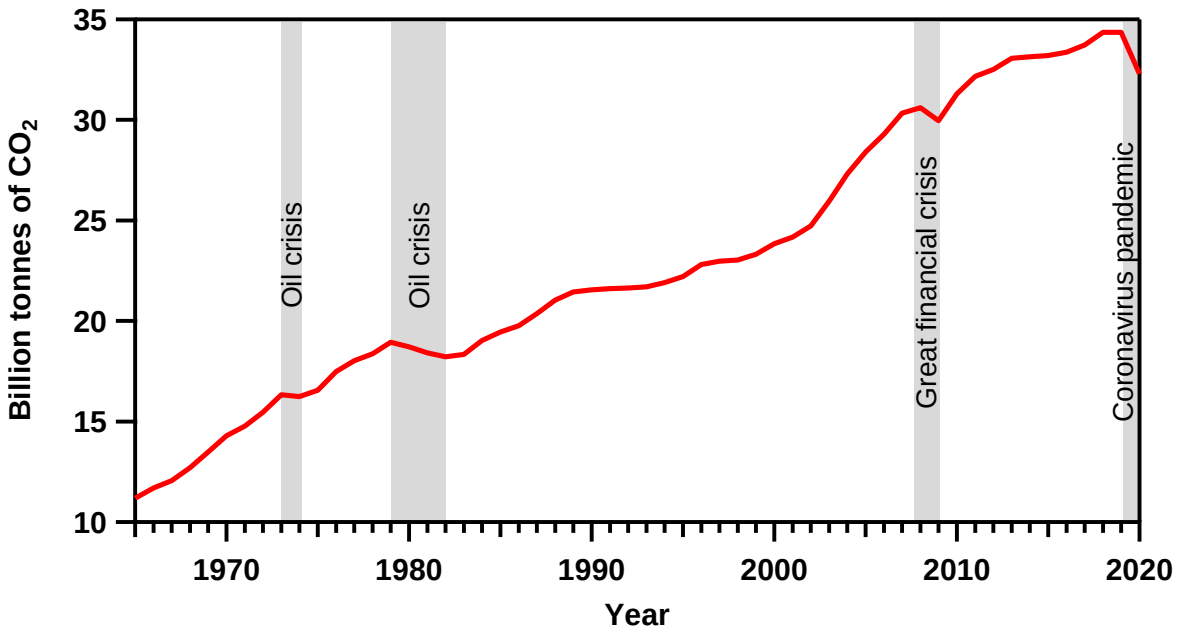

Figure 1: Global carbon dioxide emissions between 1965 and 2020.[10] Economic recessions are highlighted with grey color.

The emission of the greenhouse gas carbon dioxide is related to the total consumption of oil, coal, and gas, which has steadily increased over the last decades. The global consumption of primary energy in exajoules for different types of fuel is depicted in Figure 2.

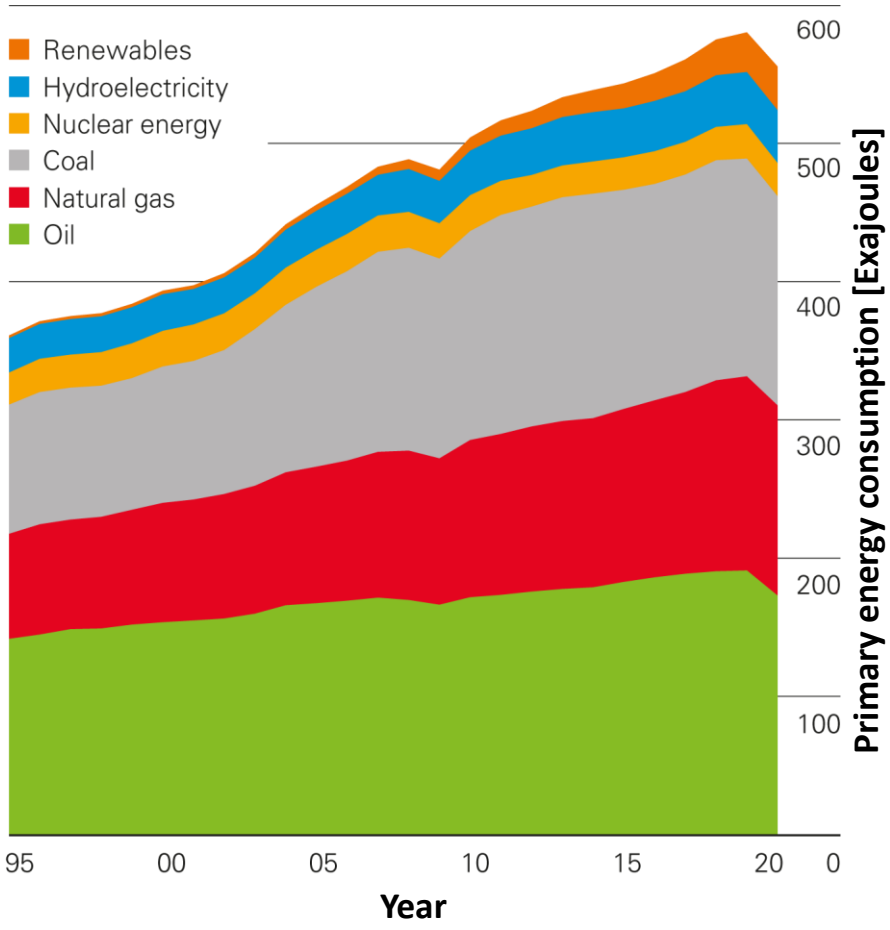

Figure 2: Global consumption of primary energy by fuel from 1995 to 2020.[10]

Merely eleven percent of the world's primary energy demand was satisfied by renewable energy sources like solar power, wind energy and hydroelectricity in 2020.[10] Despite the growing share of renewables, the demand for carbon-based fuels has still increased in the presented time period. At the same time, public and political awareness towards a more sustainable and greener energy production is growing. In the course of this development, the Paris Climate Agreement was negotiated during the 21st United Nations Climate Conference.[11-13] The agreement aims to limit global warming to below two degrees Celsius compared to the pre-industrial era, therefore limiting the use of CO_2-emitting fuels.[11, 14]

In addition to the positive impact on the climate, renewable energy sources would also provide geopolitical independence for nations, which have low non-renewable energy

reserves, as fossil fuels are not distributed evenly around the world.[15] Renewable energy sources are also not equally distributed around the world, but most nations have access to at least one form of renewable energy, such as wind, solar, or hydropower. At the moment, political crises or escalations in energy-exporting countries often threaten the energy supply of industrialized nations.[16] Furthermore, a beneficial impact of a higher share of renewable energies on economic growth was demonstrated.[17-18]

However, many renewables, including wind and solar, have the decisive disadvantage that they are not capable to provide base-load power.[19-20] The weakness of solar and wind energy is that it is subject to day and night cycles.[20] Additionally, seasonal changes have an influence on the energy yield of these renewable energies.[21] Currently, when there is a high energy consumption and low renewable energy production, the gap is closed by ramping up conventional power plants that run on fossil fuels.[22] Despite the growing market share of renewable energy sources, the demand for the conventional power plants is therefore still high. This leads to the necessity of two parallel energy systems with supply chains, which have to be maintained and financed. One solution is the installation of large-scale energy storage systems that smooth out the power peaks and troughs. The general idea is that an oversupply of renewable energy during favorable weather conditions is stored and consumed during times of undersupply.

So far, only hydropower has become commercially viable as an energy storage solution. In this physical storage technique, water is pumped into a higher basin by electric pumps and, when energy is required, is fed back through an electricity-generating turbine. This solution is relatively inexpensive, is very well understood, and is theoretically not subject to any size limitation. Hydroelectric storage facilities have high efficiencies but relatively low energy storage densities.[23-24] Furthermore, the output rate can be adjusted quickly to meet energy demand.[22] However, this method is only suitable for geographically favorable areas and is therefore not universally applicable, such as in the lowlands or dry regions. In addition, flooding of larger areas conflicts with human-used lands and environmental protection efforts.

Another proposed physical storage technique is the use of compressed air.[22-23] Surplus energy is used to drive electric pumps that compress air into a reservoir. Like for hydroelectric plants, a quick response time can be realized upon energy demand. Due to the low energy density (2.9 kWh/m^3 at 20 bar) and the need for large reservoirs, it is

discussed to store compressed air in subterranean caverns.[23] This fact limits the use of compressed air to geologically suitable areas.

In addition to physical storage methods, there are also ways to store energy in electrical form. Excess energy can be stored electrically in supercapacitors.[25-27] Supercapacitors are characterized by very fast charge and discharge times. Some modern supercapacitors have nano-architecture electrodes.[28-30] Metal oxides are integrated into carbon materials like carbon nanotubes (single- and multi-wall), graphene or carbon fiber papers.[31] Supercapacitors have a high power density of around 10 kW/kg.[32] As a consequence, high currents can be delivered by supercapacitors. However, only relatively low energy storage densities of ~5-10 Wh/kg are achieved.[32]

Another electrical energy storage technique are batteries.[33-36] Lead acid batteries are a mature technology and have comparably low costs.[22] On the flip side, these batteries are dangerous for the environment and an expensive recycling process is needed after around 500 – 1500 cycles.[22] Lithium-ion batteries on the other hand have higher energy storage capacities (theoretically up to ~280 Wh/kg)[37], but are more expensive due to the used rare raw materials. Moreover, damaged lithium-ion batteries (e.g., in car accidents) can lead to fires with high heat, which are difficult to extinguish. At the moment, sodium-ion batteries are also being developed, which do not require the relatively expensive raw material lithium.[38] Compared to lithium-ion cells, these offer a slightly lower energy density, but have a higher level of safety. In the future, sodium-ion batteries could play an important role especially in stationary energy storage systems where weight is not a critical factor.

Excess energy can also be used for the electrolysis of water to produce hydrogen and oxygen.[39-43] Hydrogen has a relatively low volumetric storage density of 3 Wh/L, but high gravimetric storage density of 33 kWh/kg. Hydrogen is typically stored physically under high pressures at around 700 bar or liquified at temperatures below -253 °C. These storage methods under harsh conditions, however, pose a risk to end users and require advanced techniques for storage, distribution and refueling. Different methods have been proposed, in order to avoid hydrogen storage in elemental form. Basically, the proposals can be divided into two different approaches: The first approach is to store hydrogen chemically in a non-reversible reaction. In such cases, hydrogen reacts with other gases/compounds to form fuels like methanol, methane, or formic acid. These fuels are

then available for thermal utilization and for use in internal combustion engines. The combustion of these fuels, however, is again emitting greenhouse gases.[44] The second approach is to use reversible hydrogen storage materials, which themselves can be divided in physical and chemical storage classes. In reversible physical storage techniques, metal hydrides or high-surface materials such as zeolites, nanotubes or graphene are used to store hydrogen through adsorption.[45-48]

A promising class of chemical and reversible hydrogen storage materials are so-called liquid organic hydrogen carriers (LOHCs).[49-67] These LOHCs are dehydrogenated and rehydrogenated, without being decomposed and are stored under ambient conditions. The application of LOHCs is presented in Figure 3.

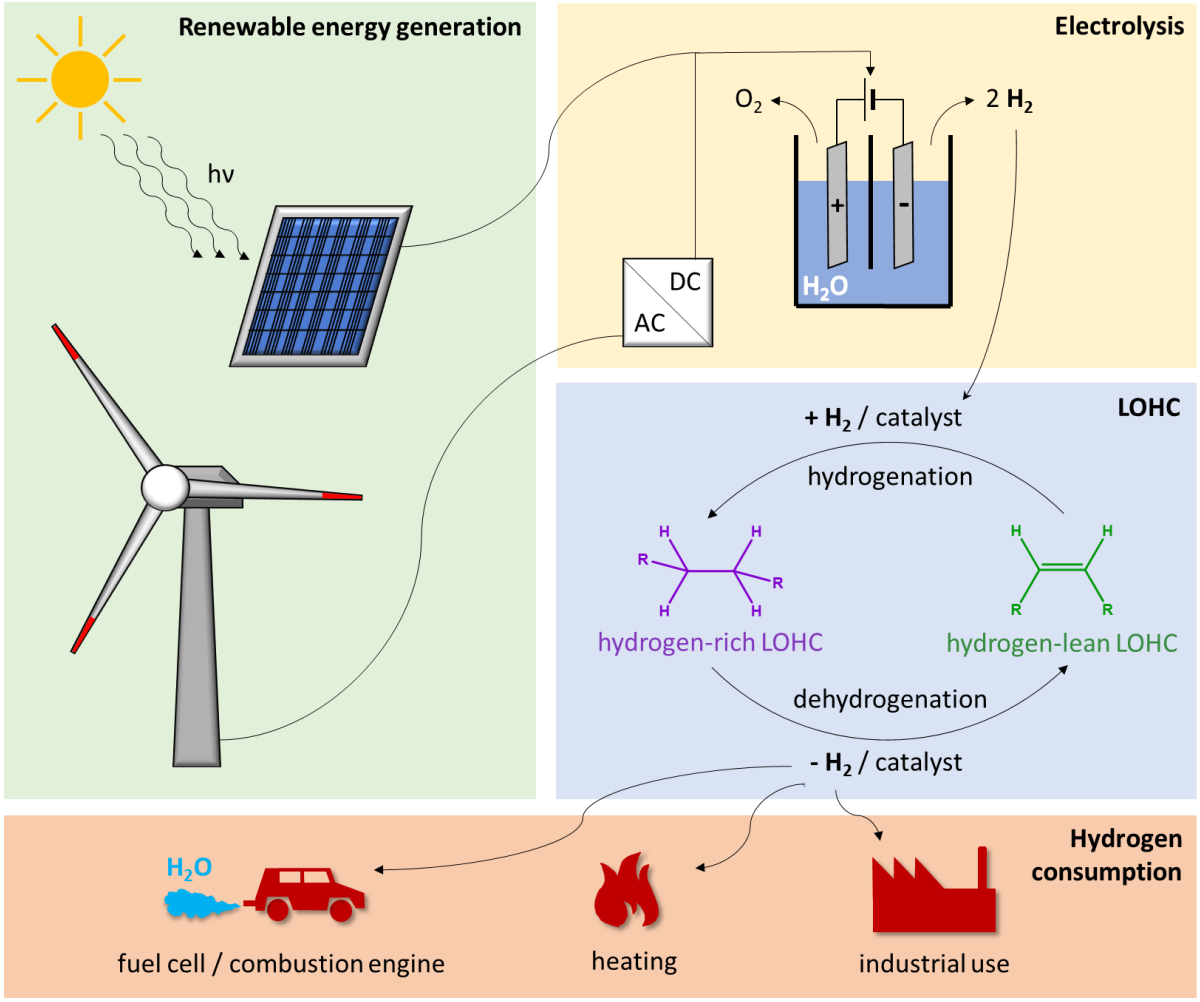

Figure 3: Schematic illustration of an LOHC cycle.

Ideally, electricity is generated by renewable energy sources like wind and solar power. This electricity is subsequently used for the catalytic electrolysis of water, which produces hydrogen and oxygen. In the next step, a hydrogen- and energy-lean LOHC compound is

catalytically hydrogenated to form a hydrogen- and energy-rich LOHC species. Afterwards, the hydrogen-rich compound can be distributed like any other liquid fossil fuel under ambient conditions, using the already existing infrastructure for diesel and gasoline. The stored hydrogen can be unloaded from the hydrogen-rich LOHC through catalytic dehydrogenation and be used for industrial application, for heating purposes or for the propulsion of vehicles. The resulting hydrogen-lean LOHC species is then returned under ambient conditions for rehydrogenation.

The concept of a LOHC fueled car is presented in Figure 4.[23] The tank of a LOHC car has to have one chamber for the hydrogen-rich LOHC and one for the hydrogen-lean species, which is returned during the refueling process for rehydrogenation. Such a tank could be realized with a movable separator or an inflatable bag, as depicted in Figure 4. The hydrogen-rich LOHC ("loaded carrier") is transferred from the tank to the hydrogen generator, where the LOHC is catalytically dehydrogenated. As continuous heating is necessary for the hydrogen production, the waste heat from the subsequent combustion of the hydrogen could be used.

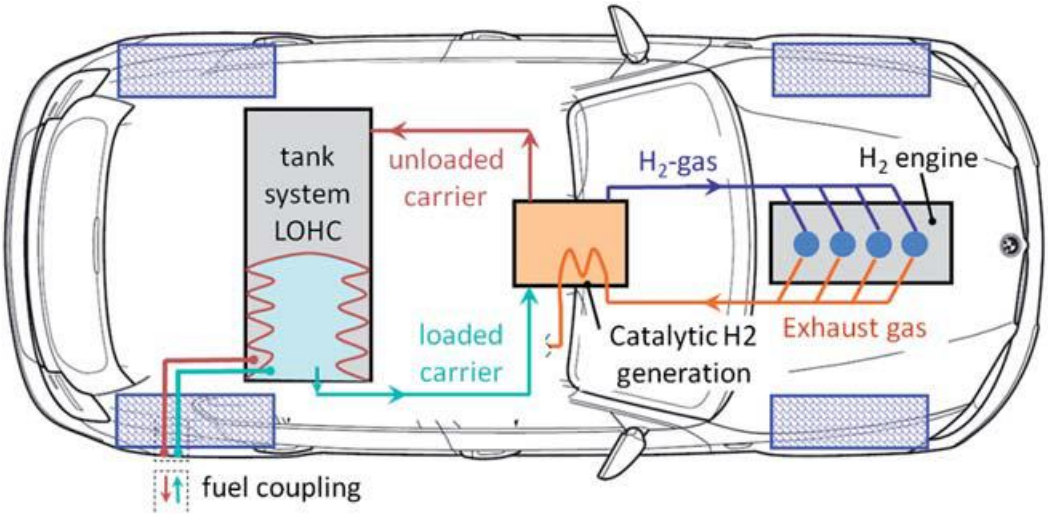

Figure 4: Use of a LOHC system in a car.[23]

Instead of the shown combustion engine, a fuel cell could also be used for the oxidation of hydrogen. However, when a fuel cell system is applied, the waste heat is not sufficient for the operation of the catalytic hydrogen generator.[23] In this case, an additional heating source has to be considered. This could be achieved by burning small amounts of hydrogen or electric heating by a direct LOHC fuel cell. After the dehydrogenation, the unloaded LOHC material is transferred back to the tank system. During the refueling

process, the hydrogen-lean substance is returned for rehydrogenation, while the hydrogen-rich substance is refueled.

Suitable LOHC candidates require low melting points, low dehydrogenation temperatures and high energy storage capacities.[55] Moreover, low toxicity and availability in large scale are desired.[68-69] An extensively studied heterocyclic LOHC system consists of the hydrogen rich H_{12}-N-ethylcarbazole (H12-NEC) with a hydrogen storage capacity of 5.8 wt% and the hydrogen-lean N-ethylcarbazole (NEC).[49, 70-74] Another prominent LOHC system uses the hydrogen rich compound H_{18}-dibenzyltoluene (H18-DBT) with a hydrogen storage capacity of 6.2 wt% and the hydrogen-lean counterpart dibenzyltoluene (DBT).[49, 75-78]

This work focuses on the dehydrogenation side of the LOHC cycle and investigates the model catalytic reaction behavior of different N- and O-heterocyclic LOHC systems on nickel (Ni(111)) and platinum (Pt(111)). The presented experiments were performed under ultra-high vacuum (UHV) conditions using the techniques high-resolution X-ray photoelectron spectroscopy (HR-XPS), temperature programmed desorption (TPD) and near-edge X-ray absorption fine structure (NEXAFS), which will be described in Chapters 2.2., 2.3., and 2.4. The combination of these three methods allowed for detailed insights into the temperature-induced reaction pathways of the LOHC candidates and the occurring intermediates. After the presentation of the experimental setups in Chapter 3 the results for different LOHCs will be discussed in Chapters 4-7.

An overview over the studied LOHC candidates on Ni(111) and Pt(111) is presented in Figure 5.

Chapter 4 presents the N-heterocyclic LOHC system indole/indoline/octahydroindole and its reaction behavior on Ni(111). In addition to that, the reaction mechanisms are compared to the reaction behavior on Pt(111), which was investigated in previous studies.

Chapter 5 discusses the reactions of the N-heterocyclic LOHC compounds 2,2'-bipyridine/2,2'-bipiperidine on Ni(111).

Chapter 6 focuses on the two chemically closely related N-heterocyclic LOHC systems pyridine/piperidine and pyrrole/pyrrolidine on Ni(111).

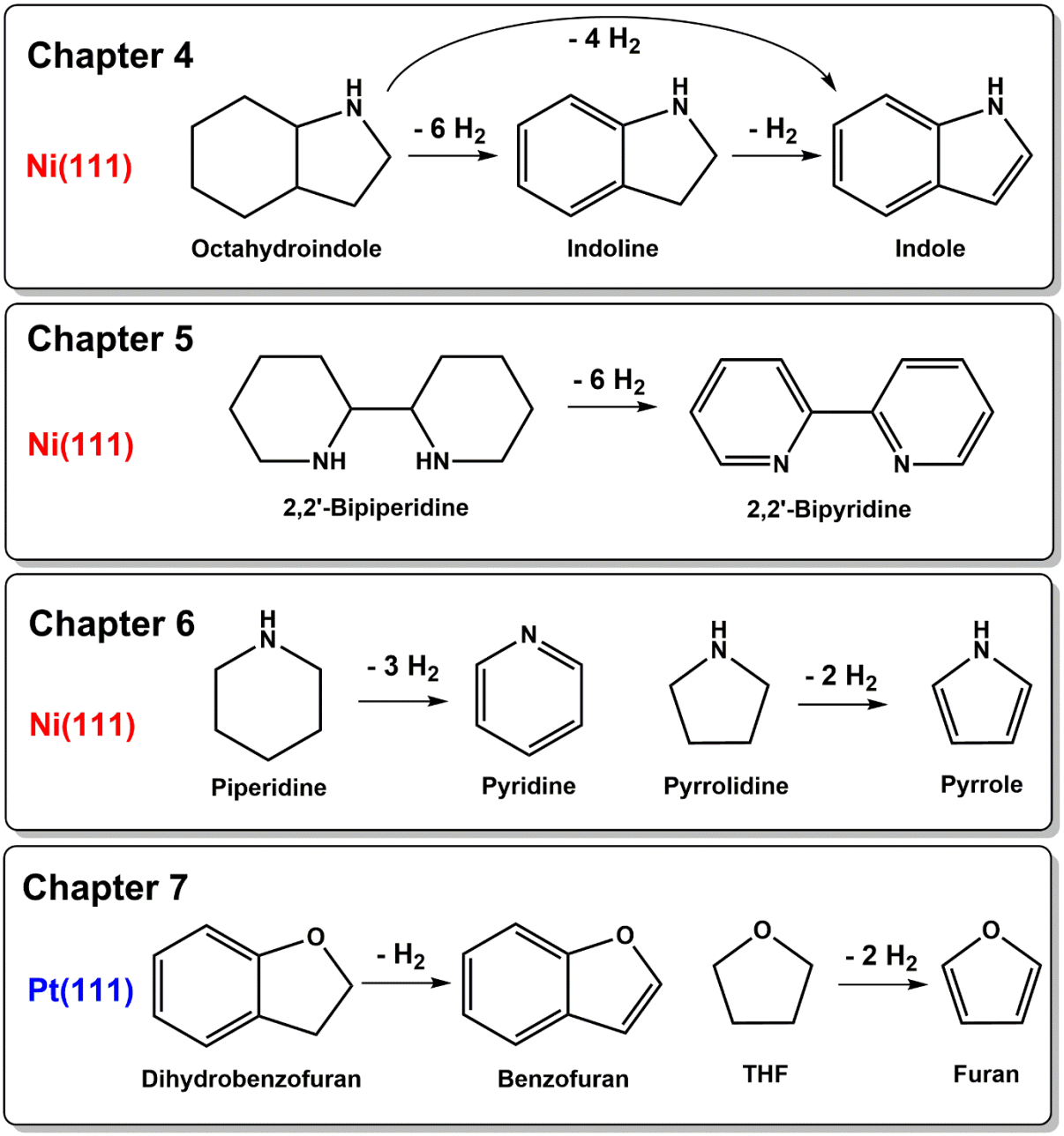

Figure 5: Overview over the studied LOHC candidates, the respective chapters and catalysts.

In Chapter 7, the dehydrogenation behavior of the O-heterocyclic LOHC compounds furan/THF and benzofuran/dihydrobenzofuran on Pt(111) is discussed. These O-heterocyclic compounds are the structural analogues to pyrrole/pyrrolidine and indole/indoline.

A conclusion and a comparison between the LOHC systems is presented in Chapter 8 and the results of this work are summarized in Chapter 9 (English) and Chapter 10 (German).

2. Fundamentals and Techniques

2.1. Synchrotron based radiation

Synchrotron radiation was used in the X-ray photoelectron spectroscopy experiments in this thesis. This section focuses on the creation of synchrotron radiation and its properties.

When charged particles with relativistic velocity are forced on a curved trajectory by magnetic fields, an electromagnetic radiation called synchrotron radiation is emitted.[79-81] This radiation is oriented in tangential direction towards the movement of the charged particles. The energy loss of the relativistic particles is given by:[82]

$$\Delta E = \frac{E^4 (Ze)^2}{3\varepsilon_0 R (m_0 c^2)^4} \quad (1)$$

with E being the kinetic energy of the particle, Z the charge number of the particle, e the elementary charge, ε_0 the electrical field constant, R the radius of the curvature, m_0 the mass of the particle and c the speed of light. This equation demonstrates that the generation of synchrotron radiation is particularly efficient when the particles have a small mass. Therefore, electrons are used in synchrotron facilities when a maximum flux of photons is desired. Moreover, the emitted energy depends on the fourth power of the kinetic energy, which favors an acceleration of the charged particles to velocities near the speed of light.

A schematic drawing of a synchrotron radiation facility is presented in Figure 6. Modern synchrotron facilities, like e.g., BESSY II at the Helmholtz-Zentrum Berlin, are typically operated as electron storage rings. In these setups, an electron gun or microtron is used to inject electrons into a booster synchrotron, where the electrons are accelerated to relativistic energies before being transferred into a storage ring with larger diameter. Bending magnets are installed at the booster synchrotron and the storage ring and force the electrons on a curved trajectory.

The synchrotron radiation is produced by bending magnets, wigglers or undulators. The latter two are installed in straight sections and consist of a periodic array of dipole

magnets.[83-85] The transition between an undulator and a wiggler is described by the dimensionless undulator strength parameter K in the equation

$$K = \frac{e\,B\,\lambda_u}{2\,\pi\,c\,m_e} \qquad (2)$$

with B being the magnetic field, λ_u the spatial period of the magnets, c the speed of light and m_e the mass of an electron.[86] A wiggler is given for values of $K > 1$ and an undulator is defined by a value of $K \leq 1$. Wigglers produce a relatively high electron oscillation amplitude and a broad energy spectrum, whereas the smaller deflection of the electrons within an undulator creates a narrower energy range due to interference of the produced light. As a consequence, the radiation from undulators has a higher degree of coherence than radiation produced by wigglers.

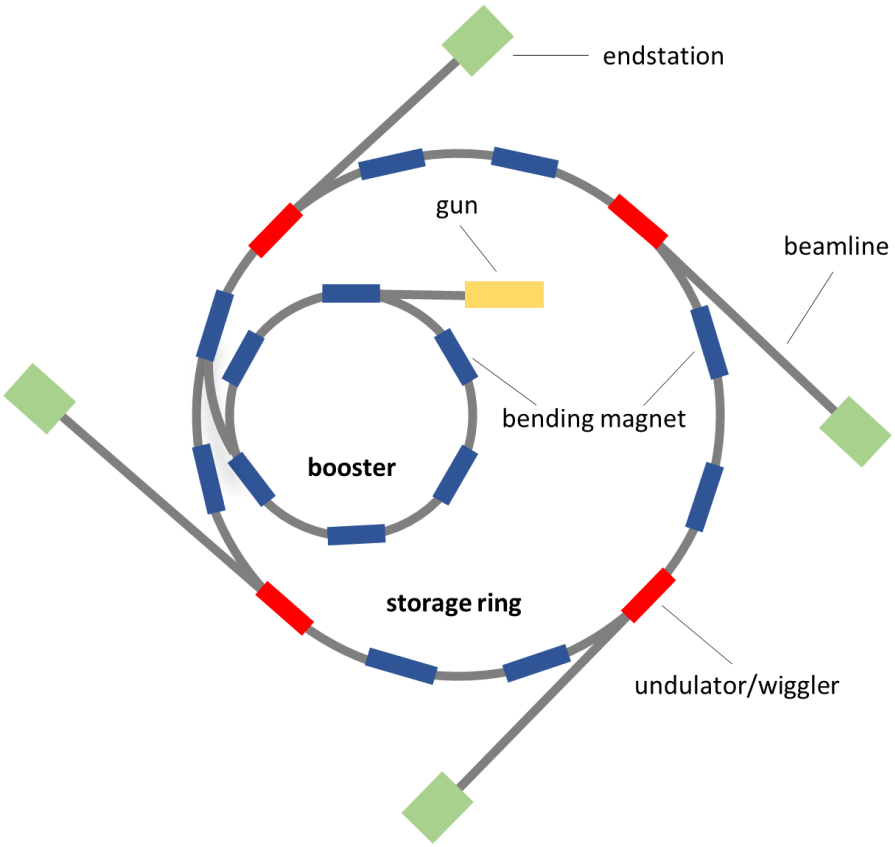

Figure 6: Sketch of a synchrotron facility with electron gun/microtron, booster ring and storage ring.

Losses of electrons circulating inside the storage ring are countered by the injection of further electrons from the booster synchrotron. Energy losses of electrons inside the

storage ring occur when the relativistic electrons pass bending magnets, the undulators/wigglers, or collide with residual gas particles in cavities.

In contrast to laboratory X-ray sources, synchrotrons provide a significantly higher flux of photons. This feature shortens the duration of measurements by around three orders of magnitude. Furthermore, synchrotron radiation has a high brilliance, which improves the spectral resolution. Since the excitation energy is freely and continuously adjustable, a high photoemission cross section can be achieved. Synchrotron radiation is of great interest for a wide range of research projects. Typical applications of synchrotron radiation are high-resolution X-ray photoelectron spectroscopy, near-edge absorption fine structure, circular dichroism spectroscopy, X-ray diffraction and radiological imaging.[87-93]

All high-resolution XP spectra presented in this thesis have been recorded at the beamlines UE56-2 PGM 1 and UE56-2 PGM 2 of the synchrotron BESSY II of the Helmholtz-Zentrum Berlin.

2.2. X-ray photoelectron spectroscopy

X-ray photoelectron spectroscopy (XPS), also known as electron spectroscopy for chemical analysis (ESCA), is a widely used surface-sensitive analysis technique. This method is based on the photoelectric effect, which was discovered by Hertz in 1887.[94-95] In 1905, Albert Einstein delivered the quantum mechanical explanation for this phenomenon and was honored with the Nobel Prize in Physics for his work in 1922.[96-97] The breakthrough of XPS and its routine use in laboratories came only after Kai Siegbahn improved the experimental setup and necessary equipment in 1954.[98-99] Usually, an excitation energy of 100 - 10,000 eV is used in XPS experiments, which results in an ionization of core electrons.[100] A technique closely related to XPS is ultraviolet photoelectron spectroscopy (UPS), which uses lower excitation energies of 5 - 100 eV. As a result, predominantly valence electrons are excited in UPS experiments.

In XPS experiments, a sample with the work function Φ_S is irradiated with X-rays of the energy hv. Electrons with the binding energy E_B are released and leave the sample with the kinetic energy E_{kin}, which is measured using an electron energy analyzer. The energy conservation is described with the following equation:[101]

$$E_{kin} = hv - E_B - \Phi_S \quad (3)$$

When the work function Φ_S of a solid is unknown, the Fermi level can be used as a reference for the kinetic energy E_{kin} and the binding energy E_B. For this purpose, a conductive connection is established between the analyzer and the sample, thus achieving a uniform Fermi level. Consequently, the equation (3) can be changed as follows with Φ_A being the work function of the analyzer:[101]

$$E_{kin,A} = hv - E_B - \Phi_A \quad (4)$$

The photoemission process with the relevant energy levels is depicted in Figure 7.

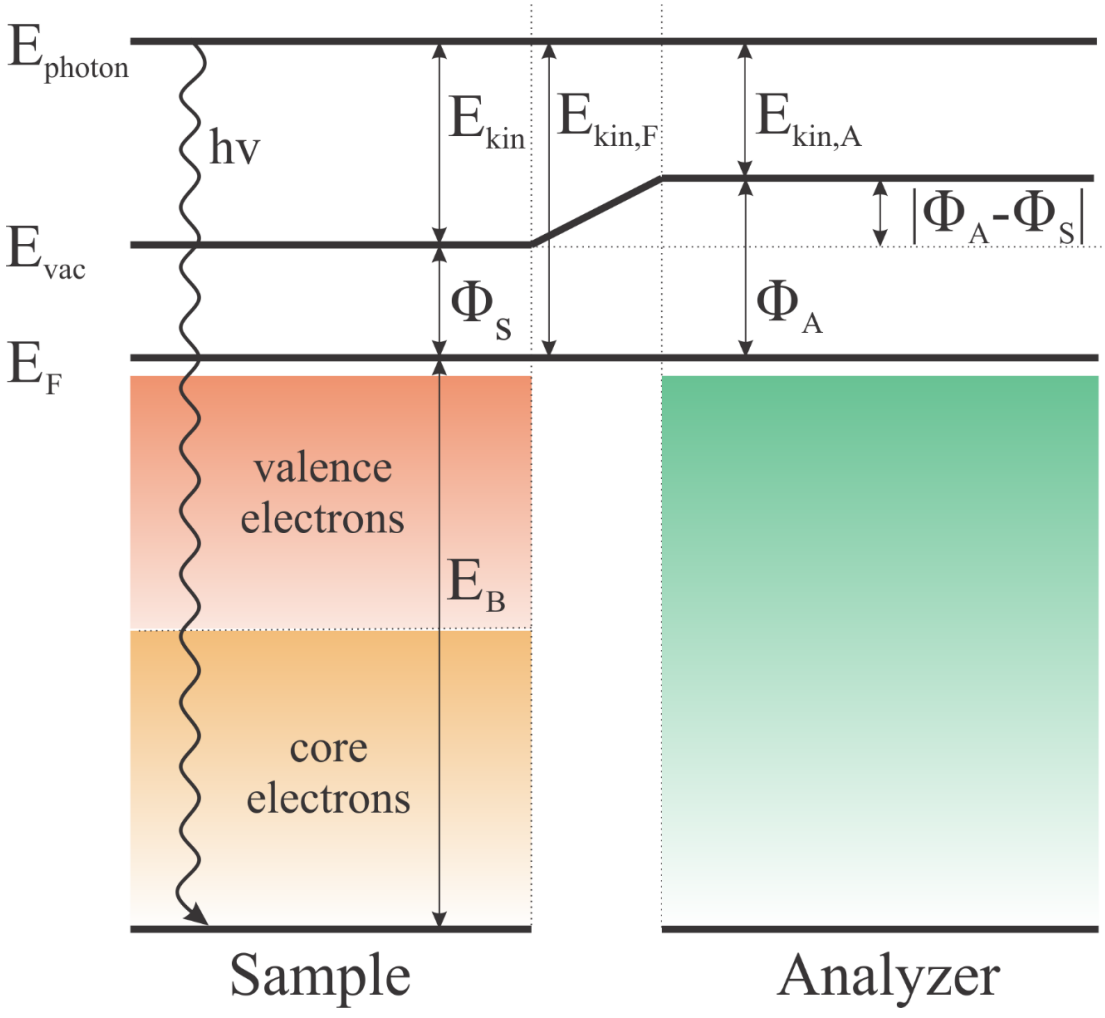

Figure 7: Schematic drawing of the energy levels in a X-ray photoelectron spectroscopy experiment. Photon energy: E_{photon}, vacuum level: E_{vac}, Fermi level: E_F, binding energy: E_B, kinetic energy of an electron in the vacuum: E_{kin}, kinetic energy of an electron correlated to the Fermi level: $E_{kin,F}$, measured kinetic energy of an electron by the analyzer: $E_{kin,A}$, work function of the sample: Φ_S, work function of the analyzer: Φ_A.

XPS is a surface sensitive technique.[101-104] The surface sensitivity of XPS is influenced by the inelastic mean free path $\lambda_{electron}$ of a photoelectron (IMFP), which is in turn defined by the kinetic energy of the photoelectron and by the sample characteristics.

The inelastic mean free path is the average distance, which electrons travel within a specimen before inelastic scattering occurs. As only primary electrons are used in XPS, i.e., electrons that did not experience losses, the surface sensitivity can be easily adjusted at a synchrotron facility (see Chapter 2.1) through variation of the photon energy.

In most publications, XP spectra are presented with an increasing binding energy to the left of the x axis. Exemplary XP survey spectra of a Ni(111) surface covered with an organic adsorbate (acetone) and a clean Ni(111) surface are presented in Figure 8:

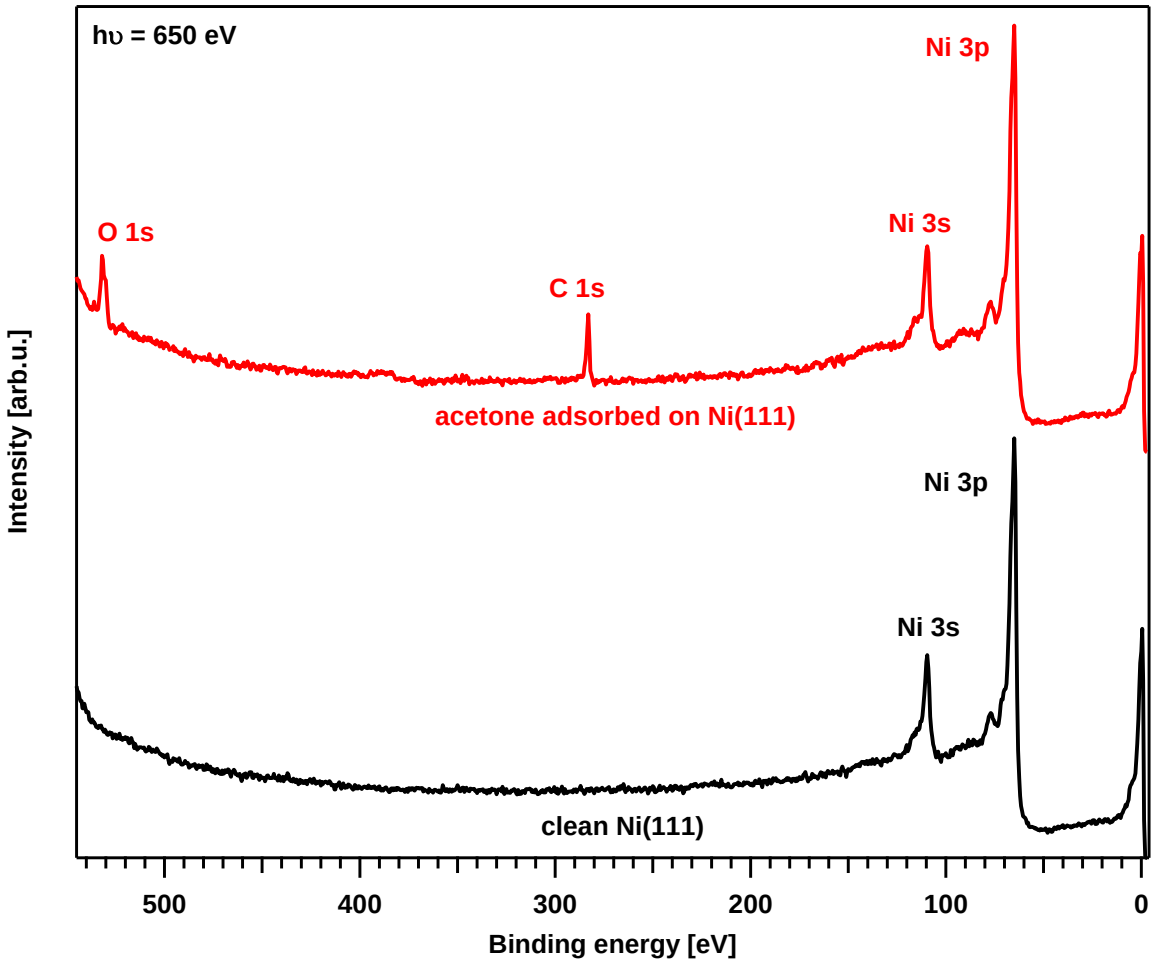

Figure 8: Two exemplary XP spectra. Bottom: Clean Ni(111) surface. Top: Ni(111) surface after adsorption of acetone.

The above spectra demonstrate, that XPS provides information about the elements of a specimen. The bottom XP spectrum in Figure 8 shows a clean Ni(111) surface, with solely

nickel signals, while the top spectrum shows additional C 1s and O 1s signals, revealing the presence of carbon and oxygen after adsorption of acetone. Different chemical elements show a unique core level energy, which can be used for a qualitative and quantitative analysis of the sample composition. In addition to that, the so-called chemical shift provides further information on the oxidation states, binding situations, adsorption sites and chemical environment of the probed atoms. The chemical shift is a superposition of initial and final state effects. Initial state effects describe the change in binding energy caused by neighboring atoms in absence of photoexcitation. Partial charges at the respective atoms cause attractive or repulsive Coulomb interactions. The partial charges are influenced by e.g., electronegativity of neighboring atoms or the oxidation state and thus changes in their energy, corresponding well to results obtained by DFT calculations. Final state effects also contribute to the observed chemical shift, as relaxation of electrons occurs after photoionization. Additional signals in XP spectra are induced by final state effects. A “shake up” process is observed, when a second electron moves into an unoccupied state (e.g., the valance band) during photoionization, which causes additional signals (satellites) at higher binding energies.[105-107] “Shake off” processes also generate satellites at higher binding energies and are caused by the removal of a second electron into the vacuum during the ionization.[105-106] Moreover, a vibrational fine structure of adsorbates can be observed in high-resolution XP spectra due to excitations of vibrations in the final state (during ionization) and which are explained by the Franck-Condon principle.[108-109] Vibrational excitations cause signals at higher binding energies, compared to the adiabatic signal. For instance, C-H vibrations cause additional signals with a shift of around 0.35 - 0.4 eV to higher binding energies, while the intensity of the signals is proportional to the number of hydrogen atoms attached to the carbon atom.[108]

As mentioned before, XPS spectra provide quantitative information about the abundance of chemical elements on a surface, as the photoionization cross section is independent of the chemical environment. For a quantitative analysis, the peak background, which is caused by inelastic scattering of photoelectrons, has to be subtracted first. Thereafter, the signal intensity integrals are compared with known and well-defined structures, like e.g., one saturated layer of graphene on Ni(111). In this example, two monolayers (2 ML) of carbon are found, which amounts to two carbon atoms per nickel surface atom.[110]

2.3. NEXAFS

Near-edge X-ray absorption fine structure (NEXAFS) is an absorption spectroscopy and widely used in solid surface analysis.[111-115] In contrast to the photoemission technique XPS, the photon energy is varied, while the change in absorption is measured. NEXAFS experiments are performed at synchrotron facilities, where the excitation energy can be changed continuously. NEXAFS focuses only on the so-called near edge, which starts at the absorption edge and reaches to ~20 eV after the edge.[116] Different NEXAFS setups are used today, which use different techniques to measure the absorption. One technique is to measure the transmission of photons through thin solid samples, thin liquid films or gases. Accordingly, the loss of intensity of photons is measured. Other techniques are summarized under the term electron yield and detect the emission of electrons upon X-ray absorption. One common method is called total electron yield (TEY), where all electrons emitted from a specimen are detected through the measured sample current. In contrast to that, partial electron yield (PEY) experiments only detect ejected electrons above a certain kinetic energy. The electrons with an energy below a certain threshold are sorted out by a retardation potential before reaching the detector. In Auger electron yield experiments (AEY) only electrons within a certain energy range can pass to the detector. In this thesis, only PEY NEXAFS experiments were carried out. The technical setup is described in detail in Chapter 3.2.

When the photon energy approaches the energy of core level electrons, the absorption probability increases. These core electrons can be excited into unoccupied states which leads to a steep increase in photon absorption, creating the so-called absorption edge. Moreover, an excitation of core electrons above the ionization threshold can occur. In this process, mainly transitions into unbound σ* orbitals (of carbon atoms) are witnessed, which typically produce broad signals in a NEXAFS spectrum. A schematic drawing of core level electron excitation through X-ray absorption is depicted in Figure 9.

The signal intensities in NEXAFS spectra are influenced by the density of unoccupied states and the selection rules. The orientation of the electric field vector of polarized radiation in respect to the orientation of the orbitals in molecules has an influence on signal intensities. Therefore, NEXAFS can be used as a tool to determine the orientation of adsorbates on a surface by tilting the sample in respect to the incoming radiation or changing the polarization of the radiation. In this thesis, NEXAFS was used to gain insights

into the orientation of aromatic compounds by measuring at normal (0° tilt angle of the sample in respect to the radiation) and grazing (70° tilt angle of the sample in respect to the radiation) incidence. The NEXAFS experiments in this work focused on the C *K*-edge and therefore on the C 1s electronic transitions. Here, the π* and σ* transitions were most important to study the orientation of the LOHC molecules on the surface.

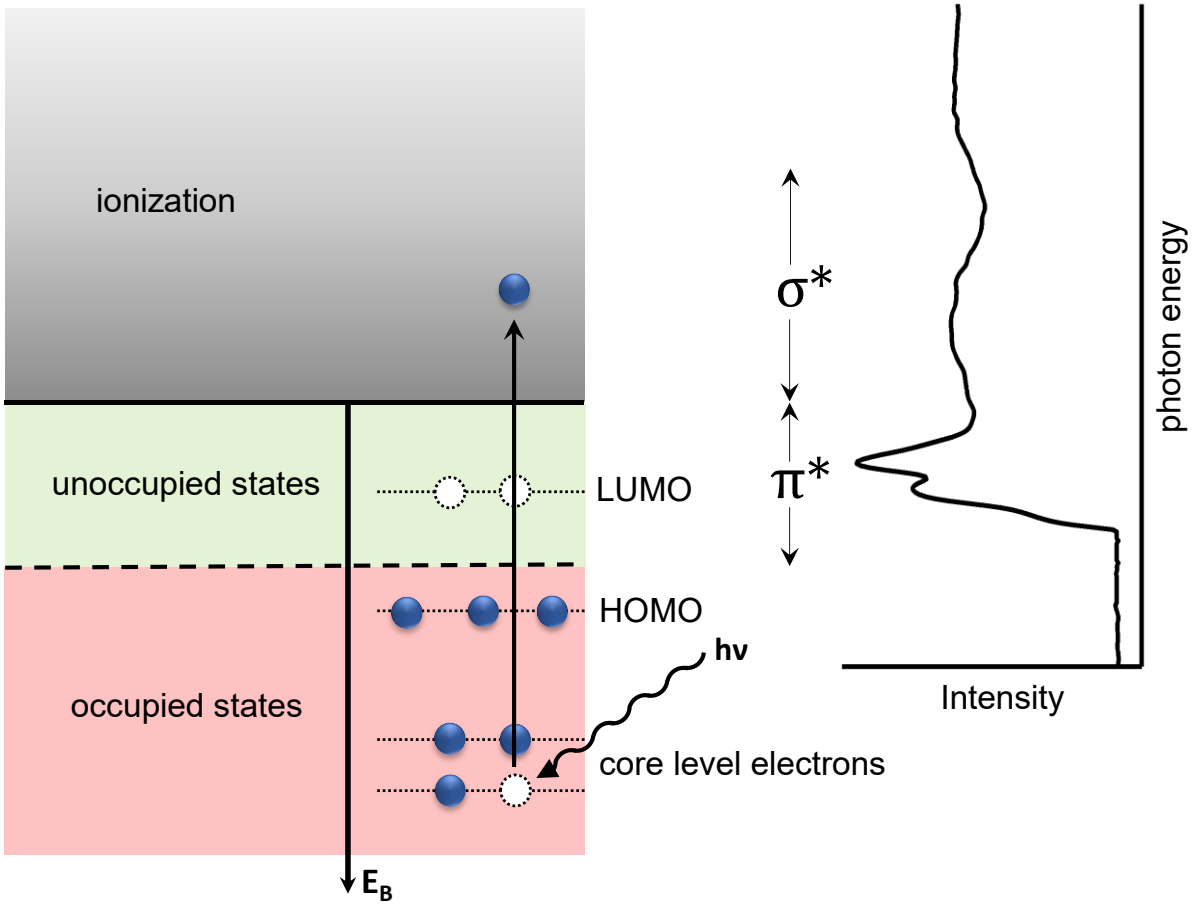

Figure 9: Schematic drawing of core level electron excitation through X-ray absorption. An exemplary NEXAFS spectrum of an organic molecule is presented on the right-hand side. The excitation of core electrons into unoccupied states (LUMO: lowest unoccupied molecular state) results in π-signals, whereas an excitation above the ionization threshold produces σ*-signals. HOMO: highest occupied molecular orbital.*

One challenge in NEXAFS spectroscopy at synchrotron facilities is that the intensity of the X-ray radiation changes with the photon energy. The change in photon flux is typically relatively high compared to the produced signals by the adsorbed molecules. Accordingly, a background correction is necessary. In this work, reference spectra of clean Ni(111)

were recorded prior to the adsorption of aromatic molecules. The NEXAFS spectra of the aromatic compounds were subsequently divided by the reference spectra.

2.4. Temperature programmed desorption

Temperature programmed desorption (TPD), also known as thermal desorption spectroscopy (TDS), is a technique, which monitors desorbing molecules from a surface with a mass spectrometer while the sample temperature is increased linearly.[117-123] TPD experiments are carried out under UHV conditions and on well-defined surfaces. In this thesis, TPD was mainly used for the detection of desorbing hydrogen released from LOHC molecules. TPD experiments in combination with HR-XPS and NEXAFS allowed for detailed insights into surface reaction mechanisms of LOHCs.

In a first step, the substance to be investigated is adsorbed onto a well-defined surface. Subsequently, the sample is heated with a linear heating ramp (e.g., 3 K/s as used in this work), and desorbing molecules are analyzed by a mass spectrometer. The partial pressure p_i of a compound is proportional to the measured ion current I_{ion}:

$$I_{ion} \sim p_i\ (t, T) \tag{5}$$

A so called Feulner cup can increase the quality of TPD experiments significantly.[124] The tube-shaped Feulner cup is attached to the mass spectrometer and is positioned in front of the sample during the heating process. The relatively small internal volume leads to a high partial pressure p_i of the desorbing compound inside the Feulner cup and therefore a high ion current I_{ion}.

The Polanyi-Wigner equation describes the desorption rate r_{des} of a chemical species from a surface:[120, 125-126]

$$r_{des} = -\frac{d\Theta}{dt} = \nu_n \cdot \Theta^n \cdot \exp -\left(\frac{E_{des}}{RT}\right) \tag{6}$$

thereby Θ is the surface coverage (ML), t the time, ν_n the preexponential desorption factor, n the desorption order, E_{des} the activation energy for desorption, R the gas constant, and T the temperature. This equation assumes that readsorption of previously

desorbed compounds can be neglected due to a very high pumping rate of the vacuum system. This condition is well fulfilled with the used setup.

The desorption order n is tied to the kinetics of the desorption. A typical zero-order process occurs, when multilayers are desorbing. In zero-order kinetics, the desorption rate r_{des} is independent from the total surface coverage Θ. It is assumed that the reservoir of molecules on the surface is infinitely large. When the supply of molecules from the multilayers fades, a sudden drop follows the desorption maximum. First-order kinetics are characterized by a unimolecular desorption where the desorption rate r_{des} is proportional to the number of adsorbed molecules. A unimolecular desorption shows an asymmetric desorption peak-shape, with a shallow intensity rise and a sharp decay after the signal maximum is reached. The position of the desorption signal is independent from the surface coverage Θ in first-order kinetics. Second-order kinetics are observed, when a recombinative desorption occurs. The desorption rate r_{des} is proportional to the square of the surface coverage Θ ($r_{des} \sim I_{ion} \sim \Theta^2$) for second-order kinetics.[125] Moreover, symmetric peak shapes are recorded, which shift to lower temperatures with increasing coverages.

An approximation of the desorption energy E_{des} for first-order kinetics is given by the Redhead-equation:[126]

$$E_{des} = RT_p \left[ln\left(\frac{v_1 T_p}{\beta_H}\right) - 3{,}64 \right] \tag{7}$$

with T_p being the temperature of the desorption peak maximum, β_H the heating rate (K/s) of the sample and v_1 the frequency factor (s^{-1}). Typically, the frequency factor is unknown, but often the value of 10^{-13} s^{-1} is used as an approximation. The desorption energy calculated with this method should be considered as a rule of thumb. Moreover, the determination of the desorption peak maximum can be difficult for multiple peak patterns. More accurate results are calculated using more advanced analysis techniques like the "leading edge method" by Habenschaden-Küppers.[127-128] This method takes also into account, that the frequency factor depends on the temperature.[129] Other popular analysis techniques are the "complete analysis method," the "Chan-Aris-Weinberg method", the "Arrhenius method" and the "shape analysis method".[129-132]

The TPD spectra presented in this work have been recorded with a quadrupole mass spectrometer (QMS). A QMS consists of an ionization unit, an acceleration unit, an analyzer, which consists of four parallel cylindrical rods (quadrupole) and a detector. The ionization unit consists of a filament, that emits electrons, which themselves are accelerated and ionize inflowing sample molecules. Subsequently, the ionized sample molecules are accelerated by the acceleration unit towards the analyzer. Inside the analyzer, four parallel rods in a quadrupole arrangement create oscillating electric fields and only sample ions with a specific mass-to-charge ratio (m/z) can pass and reach the detector.

3. Experimental setups

In this chapter, the experimental setups for high resolution XPS (HR-XPS), near-edge X-ray absorption fine structure (NEXAFS) and temperature programmed desorption (TPD) experiments are presented, and the corresponding UHV machines with their equipment are discussed.

3.1. Synchrotron-UHV-apparatus

HR-XPS experiments were performed at the beamlines UE56/2 PGM1/2 of the synchrotron facility BESSY II of the Helmholtz-Zentrum Berlin. A custom-made transportable UHV apparatus (see Figure 10) was installed as end station of the beamline.[133]

Figure 10: Picture of the synchrotron UHV apparatus.[133]

The UHV machine consists of an analysis chamber, a preparation chamber and a supersonic molecular beam and sits on movable stands, which allows for three-dimensional movement and thus precise alignment relative to the X-ray beam of the synchrotron. The analysis chamber is equipped with a hemispherical electron energy analyzer (Omicron EA 125 HR U7), a quadrupole mass spectrometer (Pfeiffer Vacuum Prisma QMS 200) and a dosing system for LOHCs. The preparation chamber houses a sputter gun (Specs, IQE 11/35, Ar^+-ions, ≤5 kV) electron beam evaporators and LEED optics. The analysis chamber and preparation chamber are connected to a separate dosing system, which is used to dose organic substances. A manipulator is used to transfer the sample between both chambers and allows for liquid nitrogen cooling, enabling temperatures down to 110 K. The sample, which is mounted to the manipulator head is heated via a bifilar coil during continuous XPS measurements up to 550 K with a linear heating ramp of 0.5 K/s. This heating method minimizes electrical fields, which could influence the trajectory of photoelectrons. Sample temperatures up to 1300 K are achieved through direct resistive heating of the crystal. For this purpose, tantalum wires are spot welded directly to the edges of the crystal. The presented spectra are referenced to the Fermi edge of Ni(111) or Pt(111), and exposures are calculated in Langmuir ($1L = 133*10^6$ Pa*s). Moreover, all presented XP spectra were recorded at normal emission (90°) and were fitted using Doniach-Šunjić profiles convoluted with Gaussian functions. Excitation energies of 380 eV (C 1s), 500 eV (N 1s) and 650 eV (O 1s) were used, with overall resolutions of 200 meV (C 1s) and 300 meV (N 1s and O 1s). To avoid beam damage, each spectrum was measured on a new spot on the sample.

3.2. NEXAFS detector setup

Like the HR-XPS measurements, the presented NEXAFS experiments were performed at the beamlines UE56/2 PGM1/2 of the synchrotron BESSY II of the Helmholtz-Zentrum Berlin in the UHV apparatus presented in Chapter 3.1. The home-built NEXAFS detector setup enables partial electron yield (PEY) experiments and is mounted to the analysis chamber of the synchrotron apparatus. A schematic drawing of the PEY detector is shown in Figure 11. A grounded shielding grid is mounted in front of the sample to reduce the effect of any electric fields on the measurements. Between the shielding grid and the channeltron (Photonis 4716), a repulsion grid is positioned and is set to negative voltages

(V3: -240 V for C 1s, -340 V for N 1s) during PEY experiments. The electrons, which have passed the repulsion grid, are then pre-accelerated by a positive voltage (V2: +200 V). The signal gain is subsequently achieved by the positive voltage (V1: +1400 – +3000 V). The signal is then tapped at the anode with a picoammeter. During NEXAFS experiments, the photon energy is varied in a continuous mode by moving the undulator and the monochromator synchronously while the anode signal is recorded.

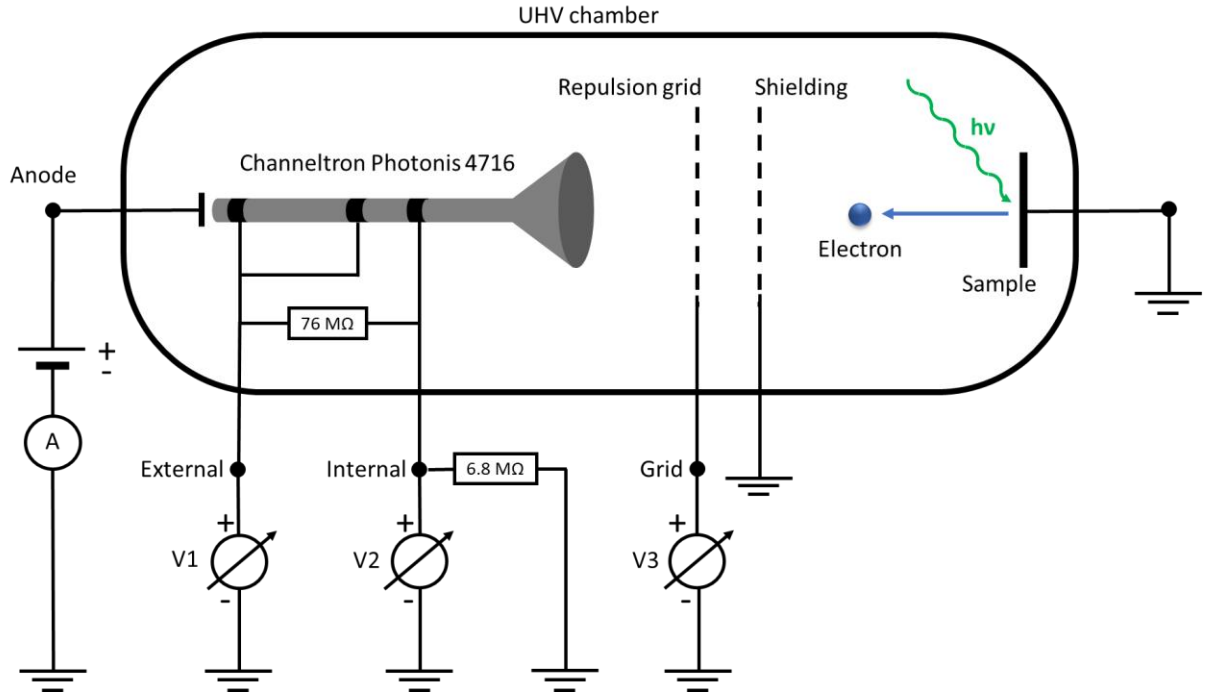

Figure 11: NEXAFS setup and wiring of the partial electron yield detector.[134]

3.3. TPD UHV setup

The presented TPD experiments were performed in a separate UHV apparatus. This machine consist of only one UHV chamber, which is used for both preparation and analysis of the surface. Furthermore, a separate dosing system and an organic evaporator are connected to the UHV machine. The machine houses a laboratory XPS setup, which consists of an X-ray source (Al Kα) and an electron energy analyzer (CLAM 100 VG). The TPD spectra were measured using a quadrupole mass spectrometer (Pfeiffer Vacuum Prisma QMS 200) in combination with a Feulner cup. The opening of the Feulner cup matches to the size of the crystal, which ensures that only the desorption of the front side of the crystal is recorded. In addition to that, the partial pressure of the desorbing molecules is higher inside the Feulner cup, as its volume is significantly smaller than that

of the UHV chamber, which further improves the quality of the TPD spectra. The UHV apparatus is equipped with LEED optics and a sputter gun. Cooling of the sample to temperatures down to 90 K is achieved with a liquid nitrogen reservoir on top of the UHV machine. Figure 12 shows the inside of the UHV machine and its main components.

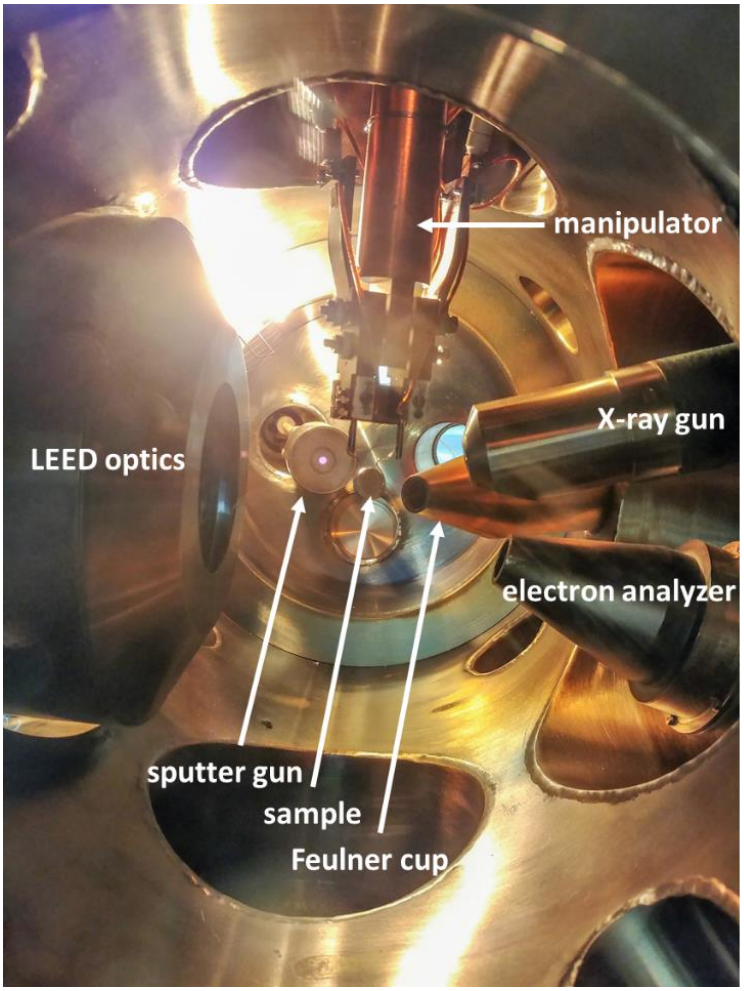

Figure 12: Inside of the TPD apparatus with view on main components.

3.4. Quantification of XPS experiments

In this chapter, the quantification of the surface coverages of carbon, nitrogen, and oxygen on Ni(111) and Pt(111) is described.

On Ni(111), the carbon coverage (1 carbon monolayer = 1 carbon atom/nickel surface atom) was calibrated by comparison with a graphene layer (2 carbon atoms/nickel atom).[135] The XP spectrum of graphene on Ni(111) in the C 1s region is presented in Figure 13. The signals in the C 1s region show the coexistence of two different adsorption geometries of graphene on Ni(111): The green signal at 284.9 eV is assigned to a bridge-

top structure, while the blue signals at 284.5 and 285.1 eV are assigned to a top-fcc structure.

The graphene layer was obtained by dosing ethylene at 900 K until full saturation, while monitoring the growth process by XPS. In a saturated and fully closed graphene layer, the XPS signal area corresponds to 2 ML of carbon, that is, two carbon atoms per nickel atom.

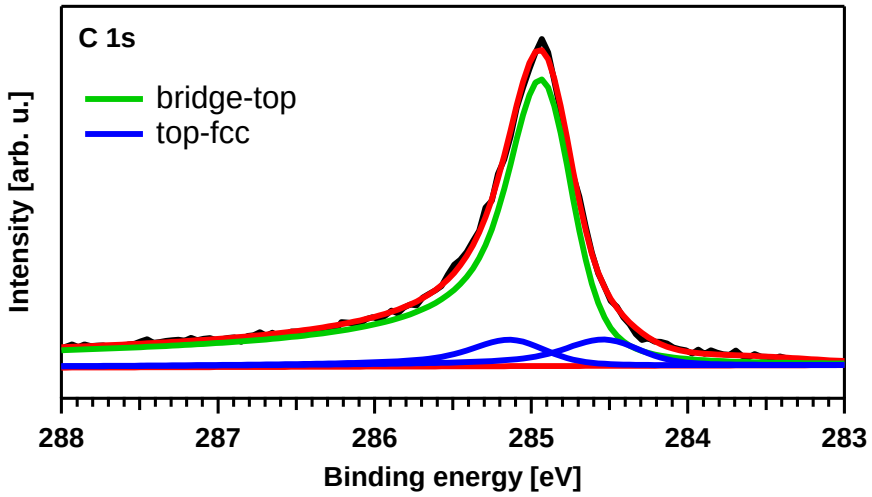

Figure 13: Ni(111) surface in the C 1s region with a closed layer of graphene for the calibration of the nitrogen coverage.

On Ni(111), the nitrogen coverage (1 nitrogen monolayer = 1 nitrogen atom/nickel surface atom) was calibrated by comparison to a saturated hexagonal boron nitride (*h*-BN) layer (1 nitrogen monolayer = 1 nitrogen atom/nickel atom). The XP spectrum of *h*-BN on Ni(111) in the N 1s region is shown in Figure 14. Hexagonal boron nitride is a structural analogue to graphene with alternating nitrogen and boron atoms and shows a signal at 398.2 eV in the nitrogen region. In a saturated and fully closed h-BN layer, the XPS signal area corresponds to 1 ML of nitrogen, that is, one nitrogen atom per nickel atom. The *h*-BN layer was obtained by dosing the precursor borazine at a substrate temperature of 1050 K.[136-137]

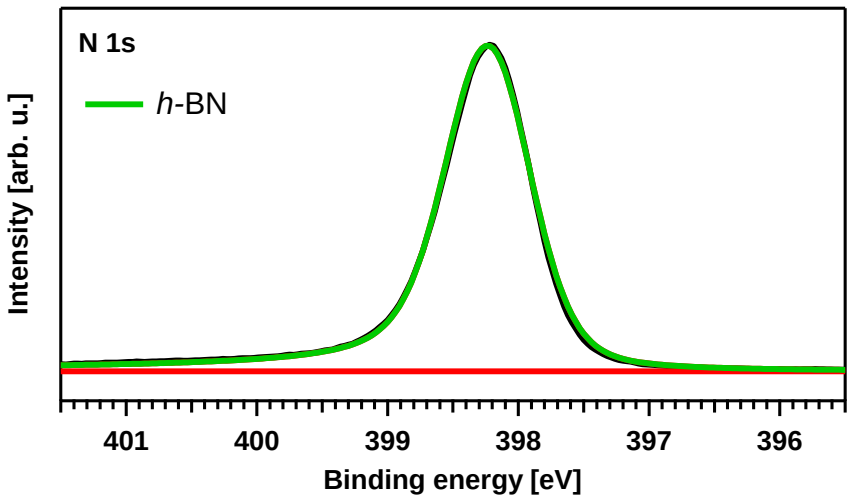

Figure 14: Ni(111) surface in the N 1s region with a closed layer of hexagonal boron nitride (h-BN) for the calibration of the nitrogen coverage.

The carbon coverage on Pt(111) was calibrated by comparison with adsorption spectra of CO showing the c(4 x 2) super structure. A spectrum of CO on Pt(111) in the C 1s region is shown in Figure 15. The signal at 286.8 eV (blue) is assigned to the on-top CO species. The on-top species is witnessed upon CO adsorption at low coverages. With an increasing coverage, the growth of a signal at 286.1 eV (green) is also seen, which is assigned to a bridge CO species. A c(4 x 2) structure in LEED is formed that has a coverage of 0.5 ML of CO. CO was dosed at 200 K.

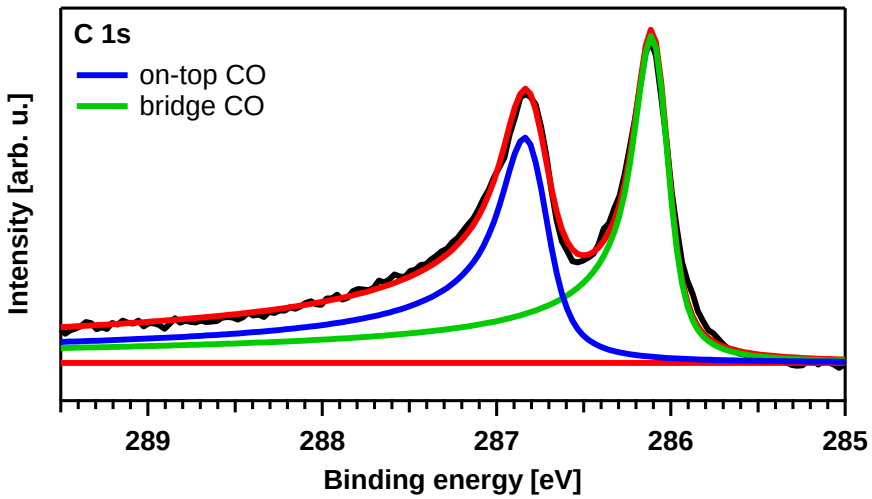

Figure 15: XP spectrum of a Pt(111) surface in the C 1s region fully saturated with CO for the calibration of the carbon coverage.

The oxygen coverage on Pt(111) was also calibrated by comparison with adsorption spectra of CO. In Figure 16, the XP spectrum of CO on Pt(111) in the O 1s region is shown.

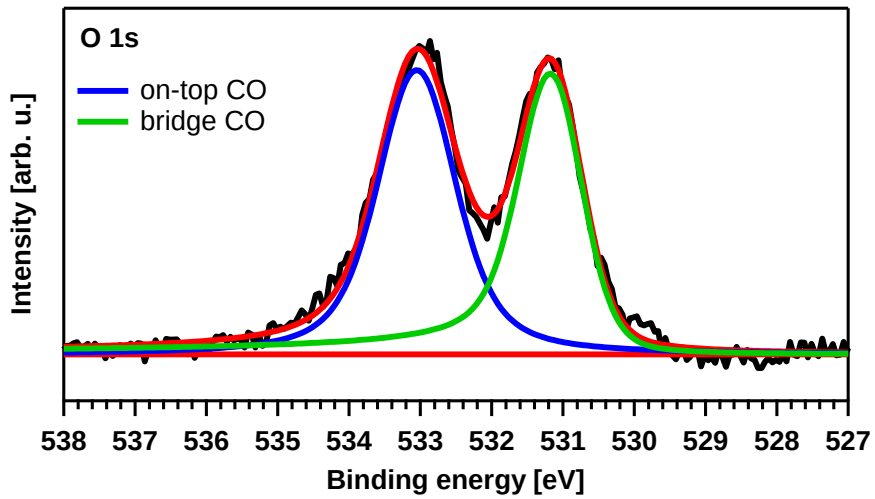

Figure 16: XP spectrum of a Pt(111) surface in the O 1s region fully saturated with CO for the calibration of the oxygen coverage.

The signal at 533.1 eV (blue) is assigned to the on-top CO species. The on-top species is witnessed upon CO adsorption at low coverages.[138] With an increasing coverage, the growth of the signal at 531.1 eV (green) is also witnessed, which is assigned to a bridge CO species.[138] CO was adsorbed on Pt(111) at 200 K.[139] The growth of both signals stops at full saturation (0.5 ML oxygen).

3.5. Single crystal preparation

The cleaning procedure of the Ni(111) single crystal (MaTecK GmbH) included Ar^+ sputtering (1 kV, $5x10^{-6}$ mbar, 30 min, 130 K) and subsequent annealing to 1200 K (1 min). XPS was used to check for impurities on the surface. Remaining carbon contaminations were removed by O_2 exposure at 800 K, followed by annealing to 1150 K to desorb oxygen residues.

The Pt(111) single crystal (MaTecK GmbH) was cleaned by Ar^+ sputtering (1.5 keV, 8×10^{-5} mbar, 20 min, 300 K) and subsequent annealing to 1200 K (3 min). Afterwards, carbon residues were removed by O_2 exposure at 900 K. Subsequently, annealing to 1200 K ensured the desorption of all oxygen residues. XPS and low energy electron diffraction (LEED) were used to control the Pt(111) single crystal.

4. Indole, Indoline, OHI on Ni(111)

The results in this chapter have been published. The content of this chapter is adapted from the publication:

Model Catalytic Studies of Liquid Organic Hydrogen Carriers: Indole/Indoline/Octahydroindole on Ni(111)

J. Steinhauer, P. Bachmann, M. Freiberger, U. Bauer, H.-P. Steinrück, C. Papp*

The Journal of Physical Chemistry C **2020**, 124, 41, 22559–22567.

Abstract: N-heterocycles belong to the class of so-called liquid organic hydrogen carriers (LOHCs), which have been identified as suitable materials for chemical hydrogen storage, due to a favorable hydrogen storage capacity and reaction kinetics. In this contribution, we focus on the dehydrogenation reaction of the hydrogen-rich octahydroindole, its dehydrogenation intermediate indoline and the hydrogen-lean indole. Octahydroindole has a hydrogen storage capacity of 6.4 wt% and indoline 1.7 wt%. We investigated the mechanism of the temperature-induced dehydrogenation of the three compounds after adsorption on Ni(111) at low temperatures. Nickel is attractive as effective and low-priced dehydrogenation catalyst, which potentially could replace the more expensive Pt and Pd in industrial applications. We compare the obtained results with our previous work on Pt(111) for the same LOHC system and for N-ethylcarbazole/ H_{12}-N-ethylcarbazole. A comprehensive understanding of the reaction mechanism was obtained by combining high-resolution XPS with TPD lab experiments. For all three compounds we find dehydrogenation at the nitrogen atom above 270 K (indole ≥130 K, indoline >180 K, octahydroindole >230 K). For indoline and octahydroindole, we observe simultaneous dehydrogenation at the carbon atoms, resulting in an indolide surface species. For octahydroindole, small amounts of side products and decomposition products are observed throughout the reaction pathway. Above 380 K, the indolide species decomposes into fragments for all three compounds.

4.1. Introduction

As described in Chapter 1, renewable energy sources, such as wind and solar energy, more and more replace fossil fuels to master the negative effects of air pollution[140], high levels of greenhouse gases[141] and shrinking resources[142]. On the other hand, these energy sources are unsteady due to environmental influences, seasonal fluctuations and day and night cycles. Consequently, energy demand and production are correlated in time [143]. Therefore, efficient and safe techniques for energy storage are required, which can be applied in large scale[143].

Elemental hydrogen is a promising energy storage material, with a high gravimetric storage density of 33 kWh per kg H_2[144]. However, hydrogen has a low volumetric storage density and for applications storage under high pressures (700 bar) or liquefaction at low temperatures (-253 °C) is necessary. As an alternative to physical hydrogen storage, chemical hydrogen storage in liquid organic hydrogen carriers (LOHCs), where hydrogen is bound to organic molecules, has been proposed[50, 145-146]. The hydrogen- and energy-lean LOHC substance is catalytically hydrogenated in large scale and can be transported and stored under ambient conditions using already existing infrastructure[147]. When energy is needed, the hydrogen- and energy-rich LOHC substance is dehydrogenated catalytically. In a functioning LOHC cycle, the organic framework of the storage molecules stays intact[23]. Recent studies revealed that N-heterocycles are good candidates for LOHC systems, as they exhibit comparably low dehydrogenation temperatures[71, 148-149]. One promising and well understood LOHC pair is N-ethylcarbazole/dodecahydro-N-ethylcarbazole (NEC, H_{12}-NEC)[70-71, 150] with a hydrogen storage capacity of 5.8 wt%. Building on that system, indole and its hydrogen-rich counterparts indoline and octahydroindole gained interest, as a higher hydrogen storage capacity can be achieved (1.7 and 6.4 wt%).[151-152] Moreover, these substances show lower dehydrogenation temperatures and are easily available. The LOHC systems indole/indoline/octahydro-indole and NEC/H_{12}-NEC were extensively studied on Pt(111) as model catalyst surface [151]. Since the performance of a LOHC system is highly dependent on the used catalyst, a comparison of different catalyst materials is of particular interest. Nickel represents a promising candidate, as it is widely used as catalyst in dehydrogenation catalysis,[153-154] and is fairly cheap in comparison with platinum. Furthermore, numerous model catalytic

studies on the reaction of cyclic hydrocarbons and heterocycles on nickel were published, which facilitates the assignment of reaction products[70, 155-157].

Herein, the results of model-catalytic surface science studies of the LOHC system indole/indoline/octahydroindole on Ni(111) are presented. We used high-resolution XPS (HRXPS) and temperature programmed desorption (TPD) to gain detailed insights into the reaction products and intermediates, and the overall reaction pathways. The investigations focus on the catalytic dehydrogenation mechanism and hydrogen release in the LOHC cycle. A simplified reaction scheme is presented in Figure 17. The dehydrogenation of the hydrogen-rich octahydroindole to indole yields eight hydrogen atoms. The partially hydrogenated LOHC compound indoline dehydrogenates under the release of two hydrogen atoms. The reactions of the energy- and hydrogen-rich compounds indoline and octahydroindole are investigated along with the reaction of the energy-lean indole. The latter provides insight into the overall thermal stability of the LOHC system, and serves as a fingerprint for the desired product.

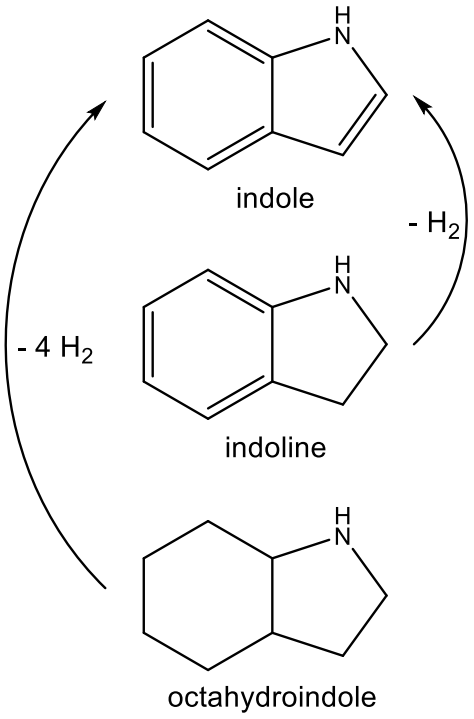

Figure 17: Dehydrogenation of octahydroindole and indoline to indole.

Under real catalytic conditions, a polycrystalline nickel catalyst would be used in the dehydrogenation of the LOHC compounds. This would include facet sites like Ni(110) and Ni(100), which may have an impact on the reaction behavior. It was shown, that different surface sites may have an impact on the adsorption energy of adsorbates and their dissociation rate. As the hydrogen adsorption energy is highly dependent on the surface sites (decrease in the order Ni(100)>Ni(111)>Ni(110)), the size and shape of the used catalytic material should impact the dehydrogenation reaction of LOHCs.[158-159]

4.2. Results and discussion

The adsorption and reaction of indole, indoline and octahydroindole was investigated with *in situ* high-resolution XPS and TPXPS in the C 1s and N 1s regions. Moreover, TPD experiments provided additional insights into the desorption of hydrogen. In the following, we concentrate on submonolayer coverages of the LOHC compounds, since no surface reaction was found in the multilayers. After desorption of the multilayers, the remaining monolayers showed the same reaction behavior as monolayers prepared by adsorbing the appropriate amounts.

4.2.1. Indole

Indole is the hydrogen- and energy-lean compound in the LOHC system indole/indoline and indole/octahydroindole. As indole is the desired reaction product in the dehydrogenation of indoline and octahydroindole, an understanding of its thermal stability limits and the related reaction mechanism of its decomposition is necessary. Furthermore, the corresponding experiments provide fingerprint spectra allowing for an easy identification of species in the following investigations of the hydrogen-rich compounds.

Figure 18 shows the C 1s and N 1s XP spectra measured during indole exposure at ~130 K (0.85 L and 0.99 L, respectively) and subsequent heating to 600 K. Figure 18a, 18b, 18h and 18g display the complete experiment in a color-coded plot, and Figure 18c-18f and 18i-18l selected spectra along with the corresponding fits. In Figure 19, the XP spectra of both regions are analyzed quantitatively. Carbon and nitrogen coverage are plotted

against the temperature and similar colors as in the XP spectra are used to illustrate the evolution of the different chemical species.

Upon exposure to indole, one observes four overlapping signals in the C 1s region, at 284.36, 284.46, 285.04 and 285.55 eV that grow with constant relative intensities.

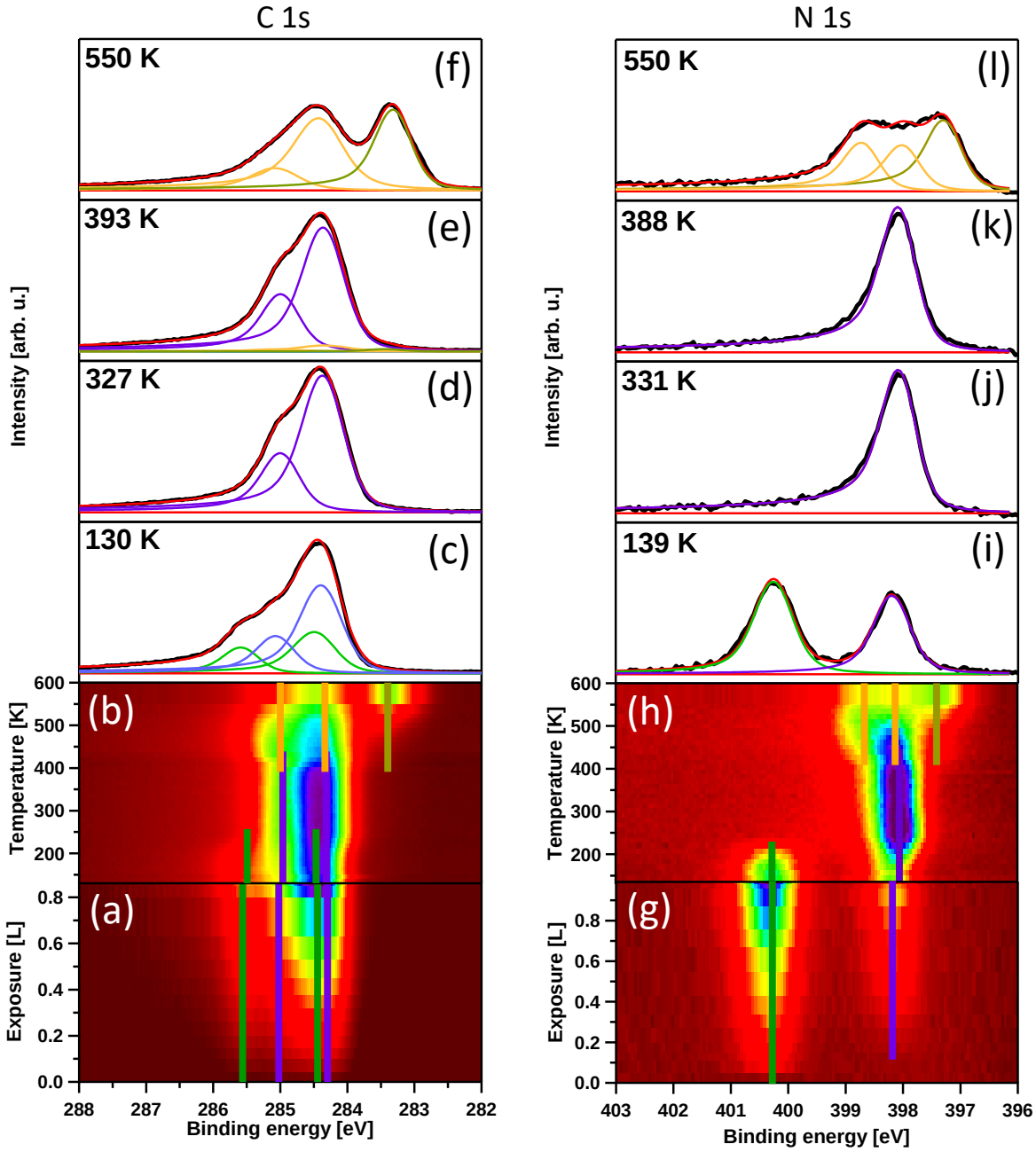

Figure 18: C 1s (left) and N 1s (right) XP spectra measured during adsorption of indole on Ni(111) at 130 K (0.85 L and 0.99 L, respectively) and during subsequent heating to 600 K. (a), (b), (g) and (h) display color-coded density plots, and (c-f) and (i-l) selected spectra along with the fits (green: indole; purple: indolide).

The signals at 284.36 and 285.04 eV are assigned to indole, and the signals at 284.46 and 285.55 eV are assigned to the first reaction product indolide (see Figure 21 for structure). This assignment in the C 1s region was only possible after evaluation of the heating experiment, and the N 1s spectra, where a clear distinction between indole and indolide is possible (see below). A detailed assignment of the C 1s signals to specific indole and indolide carbon atoms is difficult due to the complexity of the molecule. However, high binding energies suggest the vicinity to electronegative, i.e. electron withdrawing neighbours, such as the heteroatom nitrogen.

In the N 1s region, the adsorption of indole leads to a signal at 400.25 eV, which is assigned to an aminic nitrogen atom[160]. The additional signal at 398.18 eV is attributed to the mentioned dehydrogenation of indole to an indolide surface species. This assignment is based on the change in binding energy that is also observed in similar reactions and compounds, which involve hydrogenated and dehydrogenated nitrogen atoms[150-151, 161]. The partial dehydrogenation of indole on Ni(111) during adsorption at 130 K already is in contrast to studies on a platinum surface[151], where the dehydrogenation at the nitrogen atom only starts at temperatures above 340 K.

Subsequently, a heating experiment (TPXPS) was performed from 130 to 600 K with a heating ramp of 0.5 K/s, while simultaneously recording XP spectra. In the C 1s region, the signals at 284.46 and 285.55 eV vanish at temperatures above 230 K, while the signals at 284.36 and 285.04 eV grow by the same amount. The total carbon coverage on the surface does not change during this reaction, which indicates the complete conversion of all indole molecules into indolide. This interpretation confirms the assignment of the species present during the adsorption experiment, and is confirmed by the TPD data.

The TPD spectrum in Figure 20, measured after indole adsorption shows a weak hydrogen desorption signal (m/z=2) at around 350 K, which is assigned to the formation of indolide, i.e. the dehydrogenation at the nitrogen atom. As hydrogen desorption from Ni(111) does not occur below 300 K[162], this desorption maximum in the hydrogen TPD is associated to the dehydrogenation at the nitrogen atom witnessed in the XP spectra already at lower temperatures.

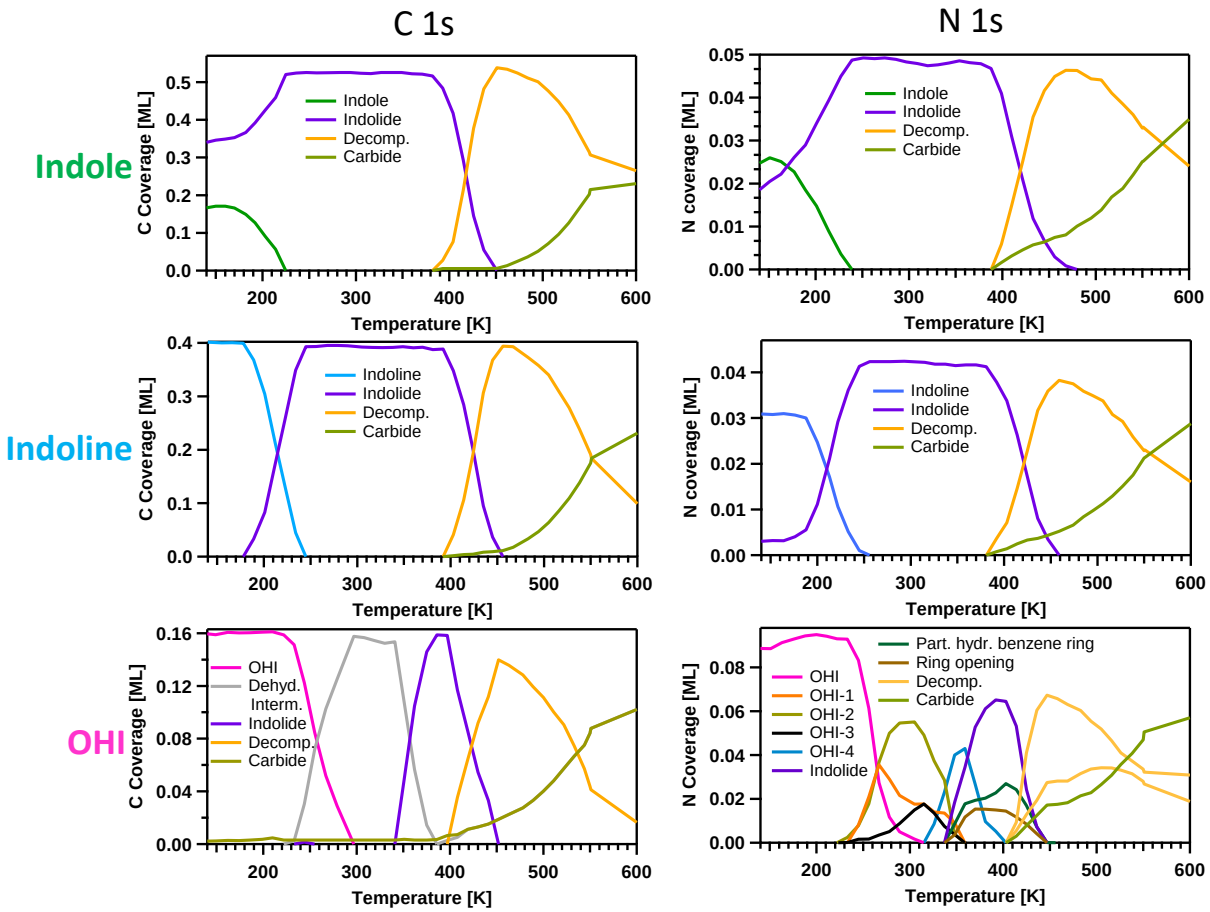

Figure 19: Quantitative analysis of the heating experiments of indole (top), indoline (center) and octahydroindole (bottom) on Ni(111) in the C 1s (left) and N 1s (right) regions.

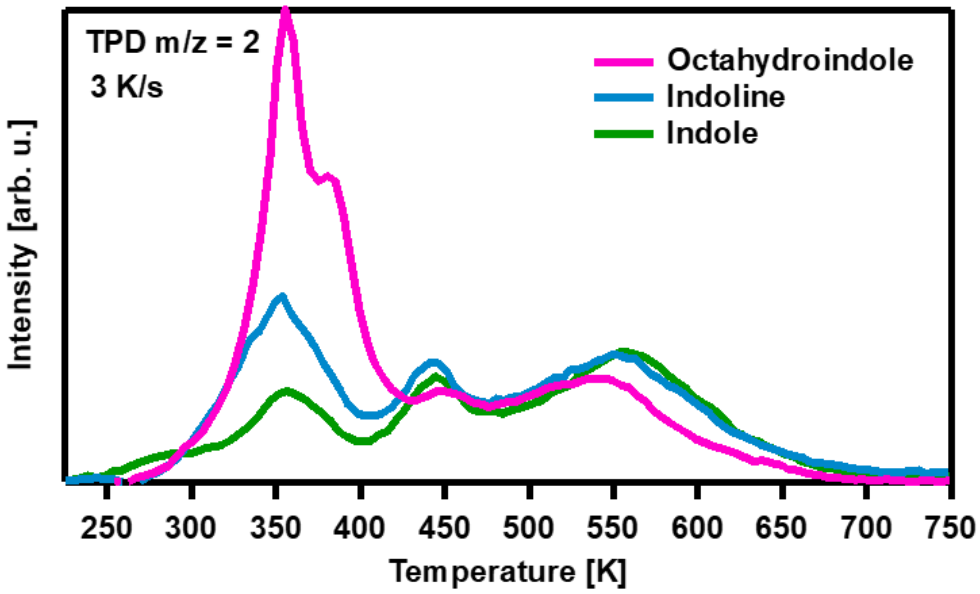

Figure 20: H_2 (m/z =2) TPD experiments of indole (27.3 L), indoline (3.0 L) and octahydroindole (0.6 L), recorded with a heating ramp of 3 K/s. T_{ads} = 110 K.

In the N 1s region, the dominant peak at 400.25 eV decreases upon heating and disappears at 240 K, while the indolide signal at 398.18 eV shifts to a slightly lower binding energy of 398.00 eV and gains intensity. At the same time, the nitrogen signal intensity in the quantitative analysis increases from 0.043 to 0.049 ML (see Figure 19). As no further nitrogen-containing molecules are supplied, this increase in intensity is assigned to photoelectron diffraction effects due changes in the adsorption geometry of the compound. Studies on a Pt(111) surface revealed that indole is lying flat on the surface.[151] A shift to an upright standing adsorption geometry for indolide is conceivable upon dehydrogenation at the nitrogen. This indicates a shift from a π-bonded to a σ-bonded configuration. Such a behavior was observed e.g. for pyridine on Ni(111).[163] At temperatures between 250 and 380 K only indolide is found on the surface, as concluded from in the C 1s and N 1s spectra.

Above 390 K, the decomposition of indolide into fragments starts, which is indicated by the rise of new signals in the XP spectra in both regions. In the C 1s region, the most notable change is the rise of the signal at 283.42 eV. In the N 1s region, a broadening of the signal is observed, with two shoulders growing at 398.66 and 397.29 eV.

The decomposition into fragments is also indicated by two hydrogen desorption signals at 440 and 550 K in the corresponding TPD experiment. Thus, both TPXPS and TPD reveal that all indolide is further dehydrogenated at temperatures above 460 K. This further dehydrogenation and decomposition of the hydrogen-lean LOHC is an undesired process in a LOHC storage system and has to be avoided. No further investigation of the decomposition fragments was conducted.

In Figure 21, the reaction pathway of indole (green) is summarized. Indole already reacts to indolide during adsorption at 130 K. Above 380 K indolide decomposes.

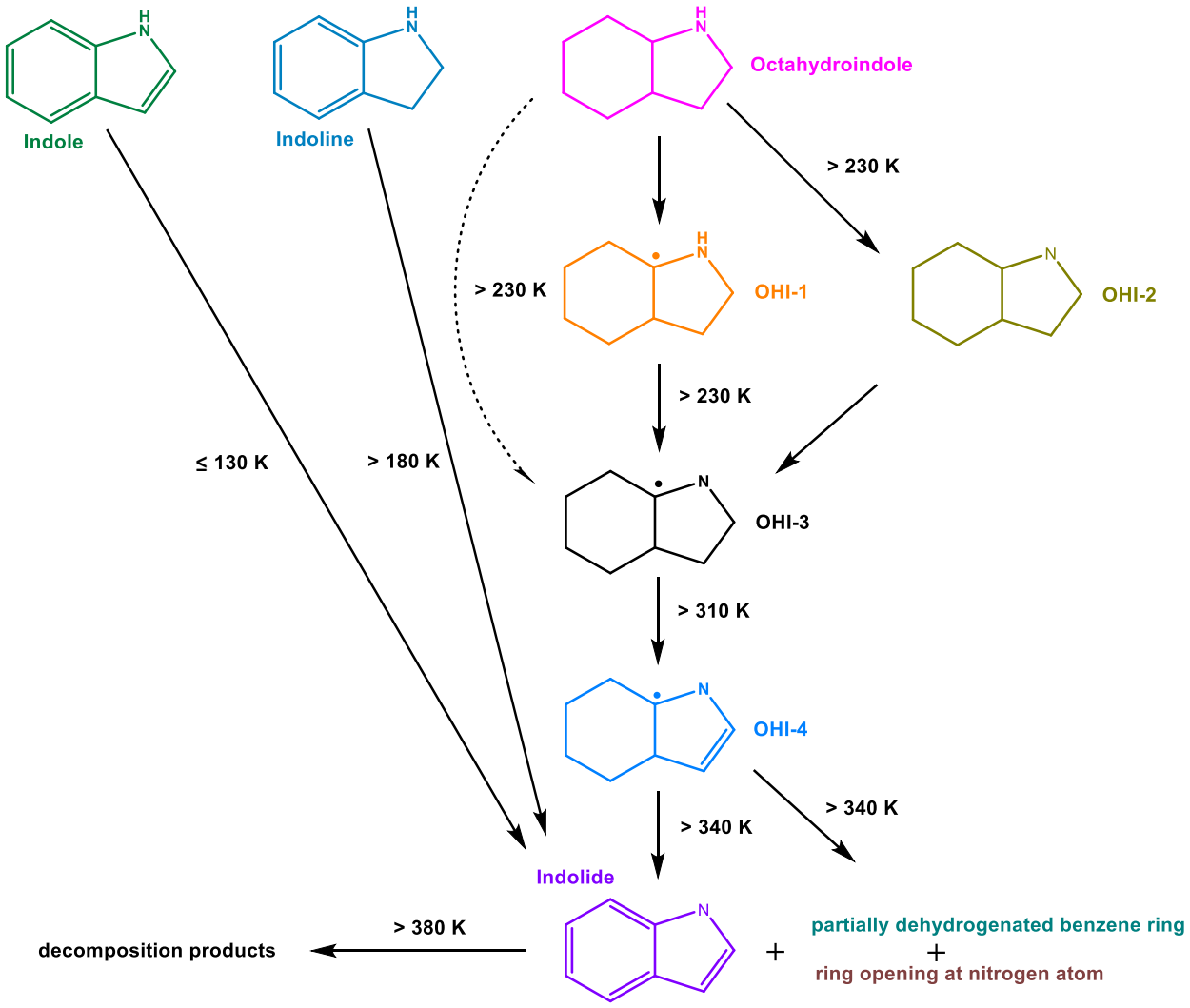

Figure 21: Reaction pathway of indole (green), indoline (blue) and octahydroindole (pink) on Ni(111).

4.2.2. Indoline

Similar to the studies of indole, the adsorption and reaction behavior of indoline was investigated. In contrast to the hydrogen-lean compound indole, indoline is hydrogenated at the five-membered ring. Thus indoline[151, 164-165] is a LOHC itself with a hydrogen storage capacity of 1.7 wt%. Moreover, it is also a possible reaction intermediate in the dehydrogenation of octahydroindole. We therefore also carried out studies on its reaction on the Ni(111) surface. The C 1s and N 1s spectra continuously collected during exposure of Ni(111) to indoline at 130 K (0.54 L and 0.64 L, respectively) and subsequent heating to

600 K are displayed in Figure 22. The corresponding quantitative analysis of both the C 1s and the N 1s regions are presented in Figure 19.

During the adsorption of indoline, the growth of four signals is observed in the C 1s region. Two dominating signals are found at binding energies of 284.17 and 284.63 eV and two smaller signals at 285.36 and 285.81 eV. The relative signal intensities stay constant throughout the exposure to indoline. As for the indole C 1s spectra region, the assignment of signals to indoline carbon atoms is difficult. As described above, higher binding energies in XPS indicate carbon atoms in closer proximity to the nitrogen atom. In the N 1s region, one signal grows at 400.09 eV during adsorption. At the highest exposures, an additional very weak signal can be observed at 398.14 eV. This binding energy was also found for the indolide surface species during the heating experiment of indole. We assign the corresponding species to very small amounts of indoline molecules that are dehydrogenated at the nitrogen atom and dehydrogenated at the pyrrole ring at 130 K. Due to the complexity of the signal pattern in the C 1s region, such a behavior can only be resolved in the nitrogen region.

Upon heating with a heating ramp of 0.5 K/s, the four signals in the C 1s region start to decrease at 180 K and two new signals grow at 284.33 and 284.96 eV. As these peaks match the binding energy and intensity ratio found for indolide during heating of indole, this first reaction product is assigned to indolide. The cleavage of three hydrogen atoms per indoline molecule is also witnessed in the TPD data in Figure 20. The first hydrogen desorption signal of indoline is approximately three times larger than the hydrogen desorption signal of indole at the same temperature. This threefold increase can be explained by the cleavage of three hydrogen atoms. Two hydrogen atoms are dehydrogenated from the carbon atoms in the five-membered ring and one hydrogen atom from the nitrogen atom. Above 180 K, we also observe a decrease in the indoline signal in the N 1s region; see also Figure 19. Simultaneously, the indolide signal at 398.14 eV starts to grow. Between 250 to 380 K, indolide is the only reaction product present on the Ni(111) surface. Interestingly, no indole is found as dehydrogenation intermediate. This observation contrasts the situation on Pt(111), where indole is observed as intermediate and where the formation of indolide occurs at ~100 K higher temperatures[151]. This indicates a higher reactivity of indoline on Ni(111).

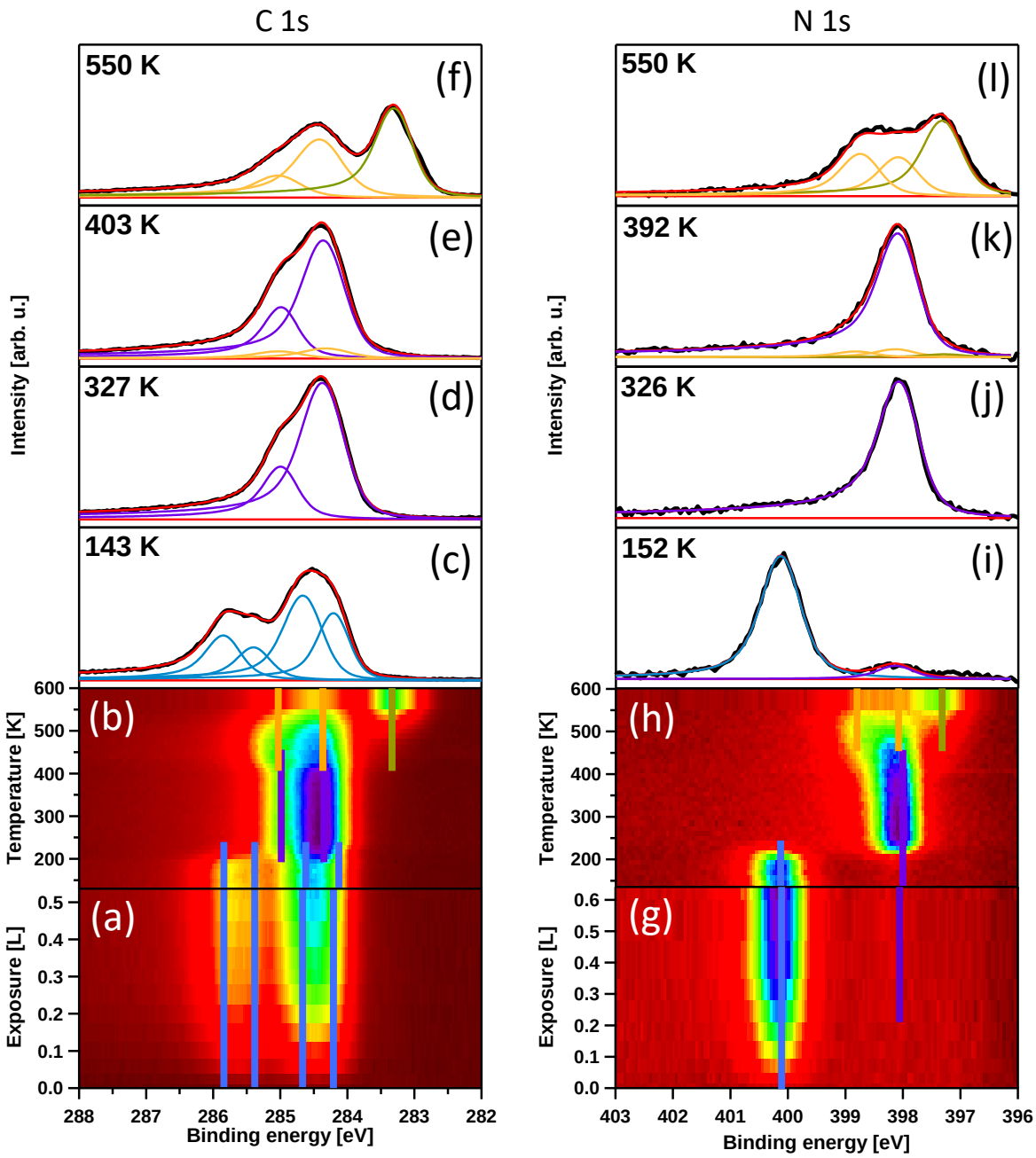

Figure 22: C 1s (left) and N 1s (right) XP spectra measured during adsorption of indoline on Ni(111) at 130 K (0.54 L and 0.64 L, respectively) and during subsequent heating to 600 K. (a), (b), (g) and (h) display color-coded density plots, and (c-f) and (i-l) selected spectra along with the fits (blue: indoline; purple: indolide).

Similar to the previous experiments with indole, indolide starts to decompose into fragments at temperatures above 380 K; see Figures 22 and 19. The decomposition is observed in both the C 1s and N 1s regions.

In the C 1s region, the growth of the distinct peak at 283.35 eV is a good indicator for the decomposition process, and in the N 1s region, two shoulders at 398.79 and 397.25 eV

start to grow around the dominant signal at 398.14 eV. The decomposition is also monitored with TPD. In Figure 20, a hydrogen desorption signal starts to grow at around 400 K and reaches its maximum at 450 K. A small shift in the temperature scale, compared to the XP spectra, is assigned to the different heating ramps (0.5 K/s in XPS, 3 K/s in TPD). At higher temperatures, a large hydrogen desorption signal is observed, which reaches its maximum at 560 K. The decomposition of the molecular framework is unwanted in the LOHC cycle. Due to the broad peak shapes in the XP spectra at higher temperatures, an assignment of the signals to specific decomposition products is difficult.

In concluding our consideration on indoline, two aspects have to be pointed out: Compared to the reaction on Pt(111)[151], indole was not observed as dehydrogenation intermediate. Moreover, the formation of indolide is shifted to lower temperatures by 100 K, and the decomposition into fragments is shifted to lower temperatures by 80 K (380 K vs. 460 K on Pt(111)[151]). Thus, a lower activation energy is needed for the dehydrogenation of indoline on Ni(111).

The reaction pathway of indoline (blue) is illustrated in Figure 21. Above 180 K indoline reacts to indolide, which decomposes into fragments above 380 K.

4.2.3. Octahydroindole

In the following, the adsorption behavior of the fully hydrogenated LOHC compound octahydroindole with a hydrogen storage capacity of 6.4 wt% is presented. The C 1s and N 1s spectra continuously collected during exposure of Ni(111) to octahydroindole at 130 K (0.075 and 0.080 L, respectively) and subsequent heating to 600 K are displayed in Figure 23.

The quantitative analysis of the heating experiment is presented in Figure 19 for both regions. Please note, that the surface coverage in the C 1s experiment is significantly smaller compared to the experiment in the N 1s region due to two separately conducted adsorption experiments.

During the adsorption of octahydroindole at 130 K, the growth of two signals at 284.80 and 285.24 eV is observed in the C 1s region. The relative intensities stay constant throughout the exposure to octahydroindole. In addition, a very small peak is found at

283.43 eV, which is assigned to nickel carbides. In the N 1s region, one signal is growing at 399.71 eV. During heating, no changes are observed until 230 K in both regions. Above 230 K, in the C 1s region, two dominating signals grow at 284.36 and 285.04 eV and two smaller signals at 283.10 and 283.60 eV.

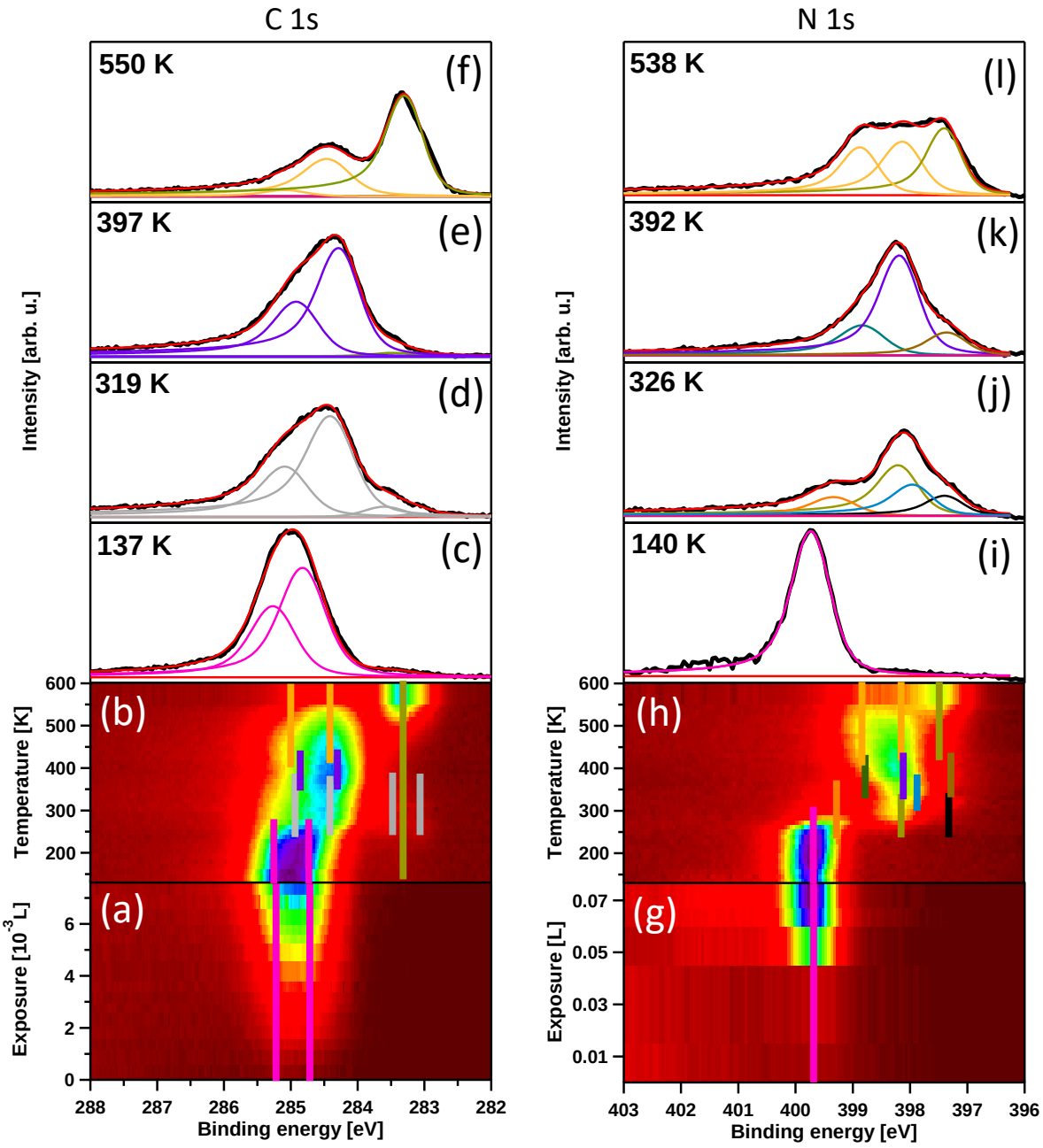

Figure 23: C 1s (left) and N 1s (right) XP spectra measured during adsorption of octahydroindole on Ni(111) at 130 K (0.075 and 0.080 L, respectively) and during subsequent heating to 600 K. (a), (b), (g) and (h) display color-coded density plots, and (c-f) and (i-l) selected spectra along with the fits (pink: octahydroindole; purple: indolide).

This pattern is present up to 380 K and is assigned to dehydrogenation of various intermediates of octahydroindole. The assignment is, however, difficult, since the spectra do not show significant changes, indicating that the reaction seems to produce several different intermediates that occur in the same temperature range. A similar situation has been observed e.g. for H_{12}-NEC[71] and indole[151-152] on Pt(111).

In the N 1s region, more insights into the dehydrogenation mechanism are possible. Above 230 K, three peaks evolve at 397.35, 398.15 and 399.28 eV. The assignment of these signals to plausible dehydrogenation products is based on their relative position to each other. The signal at 399.28 eV has the smallest shift from the pristine octahydroindole peak at 399.71 eV. Accordingly, no dehydrogenation at the nitrogen atom is assumed, but a dehydrogenation in the vicinity of the N atom. Therefore, this peak is assigned to an octahydroindole molecule dehydrogenated in alpha position to the nitrogen atom at the tertiary carbon atom (see Figure 21, "OHI-1"). A dehydrogenation at this tertiary carbon atom is expected to be more favorable than a dehydrogenation at a secondary carbon atom, due to a better stabilization of the remaining fragment. The signal at 398.15 eV is assigned to an intermediate, which is dehydrogenated at the nitrogen atom ("OHI-2"), as its binding energy matches the binding energy of indolide at 398.14 eV. The third signal at 397.35 eV is assigned to a dehydrogenation intermediate ("OHI-3"), which is dehydrogenated at the tertiary carbon atom next to nitrogen and dehydrogenated at the nitrogen atom. According to the quantitative analysis in Figure 19, the formation of this compound may be possible via OHI-1, OHI-2 or pristine octahydroindole. The compounds OHI-1, OHI-2 and OHI-3 are present up to 350 K. Between 315 and 380 K, one further signal develops in the N 1s region. We assigned this signal to a dehydrogenation intermediate ("OHI-4"), which is dehydrogenated at the tertiary carbon atom next to nitrogen, dehydrogenated at the nitrogen atom and additionally dehydrogenated at the pyrrole ring. During the formation of OHI-4, the highest hydrogen desorption rate is observed in the TPD experiment at around 350 K (see Figure 20).

Coming back to the carbon region, two new signals start to grow at temperatures above 340 K at 284.28 and 284.93 eV, which reach their maximum intensity at ~390 K. These peaks fit to the signals of indolide found in the previous experiments. At the same temperature, a dominant peak at 398.14 eV is found in the N 1s region, which is assigned to indolide. Moreover, two shoulders are observed at 397.32 and 398.78 eV. These signals

are tentatively assigned to the formation of indolide with a partially hydrogenated benzene ring and a product, which is formed by ring opening of the pyrrole ring at the nitrogen atom. In both regions, the indolide species is found up to 450 K. However, a decomposition into unspecified fragments sets in at around 400 K.

The reaction pathway of octahydroindole (pink) is much more complex than for indole and indoline, and is summarized in Figure 21. Octahydroindole reacts to indolide via the dehydrogenation intermediates OHI-1, OHI-2, OHI-3 and OH-4, which can only be resolved in the N 1s region. However, also other byproducts are observed in the same temperature range as the fully dehydrogenated indolide surface species. The formation of nickel carbides have to be considered in a technical application, as the enrichment of carbides over multiple dehydrogenation cycles may have an impact on the LOHC surface reaction. Our experiments show, that it is possible to partially dehydrogenate OHI before decomposition. The integration of the TPD spectrum of OHI up to the decomposition temperature (380 K) derived from the XP spectra, shows the desorption of ~7 hydrogen atoms. In contrast to our UHV experiments, a desorption of (partially) dehydrogenated species is highly likely under real catalytic conditions. This would lead to vacant surface sites for further dehydrogenation of hydrogen-rich molecules.

4.2.4. Ni(111) vs. Pt(111)

Indole shows the same reaction pathway on both catalysts, but with different reaction temperatures. On the Ni(111) surface, indolide is partly formed already upon adsorption at 130 K, while on Pt(111) heating to 280 K is required[151-152]. Moreover, the decomposition temperature of indolide is also shifted to lower temperatures on the Ni(111) surface (380 vs. 450 K[151]).

For indoline, we found different reaction mechanisms on the two model catalyst surfaces. On Ni(111), indolide is formed above 180 K directly without a stable intermediate, and on Pt(111) the required temperature is 280 K[151-152]. On Pt(111), however, a stable reaction intermediate indole is formed, which is completely transformed into indolide at 400 K. On Ni(111), indole was not found as an intermediate. Due to a lower dehydrogenation temperature, nickel thus might be more favorable as catalyst for the dehydrogenation of indoline.

Octahydroindole exhibits complex reaction pathways on both catalysts. However, some main aspects can be pointed out. Octahydroindole reacts on Ni(111) via several dehydrogenation intermediates to indolide at 340 K. At this temperature, indolide formation is accompanied by partially dehydrogenated compounds and ring opening products, which is undesirable for a LOHC system. On Pt(111), indolide is formed already at around 280 K together with indole,[151-152] and at 450 K, almost exclusively indolide is present. Due to the absence of byproducts and the lower dehydrogenation temperature, platinum should be a better catalyst for the dehydrogenation of octahydroindole.

A clear explanation for the partly higher reactivity of nickel in comparison to platinum cannot be given, as it can be influenced by different factors. The activation energy for the dehydrogenation can be dependent on different work functions of the two metals, their d-character, lattice spacing, bond lengths and strength between adsorbates and metals.[166]

The reaction temperatures of indole, indoline and octahydroindole are compared graphically for Ni(111) and Pt(111) surfaces in Figures A 1-3.

4.3. Conclusions

The surface reaction of the LOHC system indole/indoline/octahydroindole on Ni(111) was investigated using high-resolution TPXPS and TPD. At 130 K, indole is dehydrogenated at the nitrogen atom, forming an indolide surface species. Indoline is dehydrogenated at 180 K at the pyrrole ring and is dehydrogenated simultaneously at the nitrogen atom, leading to indolide. The indolide species formed from indole or indoline is stable up to ~380 K. Octahydroindole starts to react at 230 K, forming several dehydrogenation intermediates. Above 340 K, an indolide species is identified , which is accompanied by a ring-opening product at the nitrogen atom and a partial dehydrogenated octhahydroindol. The decomposition of indolide into fragements is observed above 400 K. The highest H_2 desorption rate was determined at around 350 K for all three compounds. A side reaction like ring-opening, as we observed for octahydroindole, has to be avoided under real catalytic conditions to prevent the loss of a reusable LOHC compound.

5. 2,2’-Bipyridine, 2,2’-Bipiperidine on Ni(111)

The results in this chapter have been published. The content of this chapter is adapted from the publication:

Model Catalytic Studies of the LOHC System 2,2′-Bipiperidine/2,2′-Bipyridine on Ni(111)

J. Steinhauer, P. Bachmann, U. Bauer, F. Düll, H.-P. Steinrück, C. Papp*

The Journal of Physical Chemistry C **2021**, 125, 15, 8216–8223.

Abstract: N-heterocyclic compounds as octahydroindole[151-152, 164] and dodecahydro-N-ethylcarbazole[70-71] have been proposed as suitable liquid organic hydrogen carriers (LOHCs) for chemical hydrogen storage. In this chapter, we focused on hydrogen-rich 2,2’-bipiperidine and hydrogen-lean 2,2’-bipyridine. Both compounds were adsorbed on Ni(111) and the temperature-induced reaction mechanism and decomposition was studied. The reaction mechanisms were investigated using synchrotron-based high-resolution XPS, NEXAFS and TPD experiments. Upon adsorption, the formation of a flat-lying chemisorbed layer is observed. Above 370 K, 2,2’-bipyridine is dehydrogenated in α-position to the nitrogen atoms to form an α-2,2’-bipyridyl species, which shows a tilted adsorption geometry. The hydrogen-rich 2,2’-bipiperidine is partially dehydrogenated above 180 K and deprotonated at the nitrogen atoms above 250 K. Temperatures above 320 K induce the formation of the α-2,2’-bipyridyl species, which is accompanied by a byproduct that is partially dehydrogenated at the carbon atoms. Above 400 K, we observe a decomposition of the α-2,2’-bipyridyl species.

5.1. Introduction

Promising candidates for LOHC systems are hydrogenated N-heterocyclic compounds, due to their favorable kinetic and thermodynamic properties.[23, 49, 148, 151, 167] For example, the LOHC pair N-ethylcarbazole/dodecahydro-N-ethylcarbazole (NEC, H_{12}-NEC) with hydrogen storage capacity of 5.8 wt% was extensively studied and showed promising results.[70-71] Another promising LOHC pair is octahydroindole/indole with a slightly higher hydrogen storage capacity of 6.4 wt%, which was discussed in the previous chapter.

In this work, we present comprehensive results of model-catalytic studies of the LOHC pair 2,2'-bipiperidine/2,2'-bipyridine on Ni(111) as dehydrogenation catalyst. In contrast to our previous LOHC studies with precious metal catalysts such as platinum or palladium, we herein focus on nickel as catalyst, which is comparably cheap and is used in large scale applications as dehydrogenation catalyst. In the course of our studies, we applied synchrotron-based high-resolution XPS (HR-XPS), near-edge X-ray absorption fine structure (NEXAFS) and temperature programmed desorption (TPD) measurements to obtain insights in the reaction pathway and to identify occurring intermediates.

A simplified dehydrogenation scheme of 2,2'-bipiperidine to 2,2'-bipyridine is presented in Figure 24. Upon complete dehydrogenation of 2,2'-bipiperidine, 12 hydrogen atoms are released, which results in a hydrogen storage capacity of 7.1 wt%.

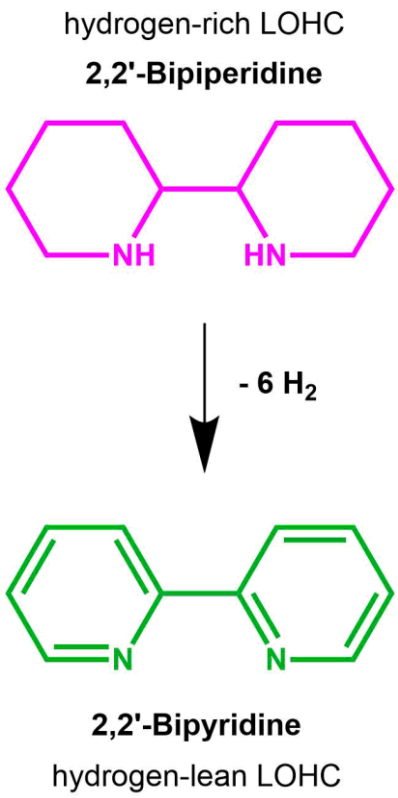

Figure 24: Dehydrogenation of 2,2’-bipiperidine to 2,2’-bipyridine.

5.2. Results and discussion

5.2.1. 2,2’-Bipyridine

The hydrogen-lean compound in the proposed LOHC system is 2,2’-bipyridine (BiPy) with the molecular formula $C_{10}H_8N_2$. In this section, we address the thermal stability limits of BiPy, as BiPy is the desired product in the dehydrogenation of the hydrogen-rich 2,2’-bipiperidine (bipip) and an intact molecular framework is crucial for a functioning LOHC cycle. Furthermore, fingerprint spectra of BiPy and its decomposition products facilitate the evaluation of XP spectra of the hydrogen-rich bipip. The spectra of the C 1s and N 1s regions were taken in independent separate experiments; therefore, they differ in surface coverage.

Figure 25 shows XP spectra of BiPy in the C 1s (left, 0.14 L, 0.69 ML carbon) and N 1s (right, 0.08 L, 0.08 ML nitrogen) regions.

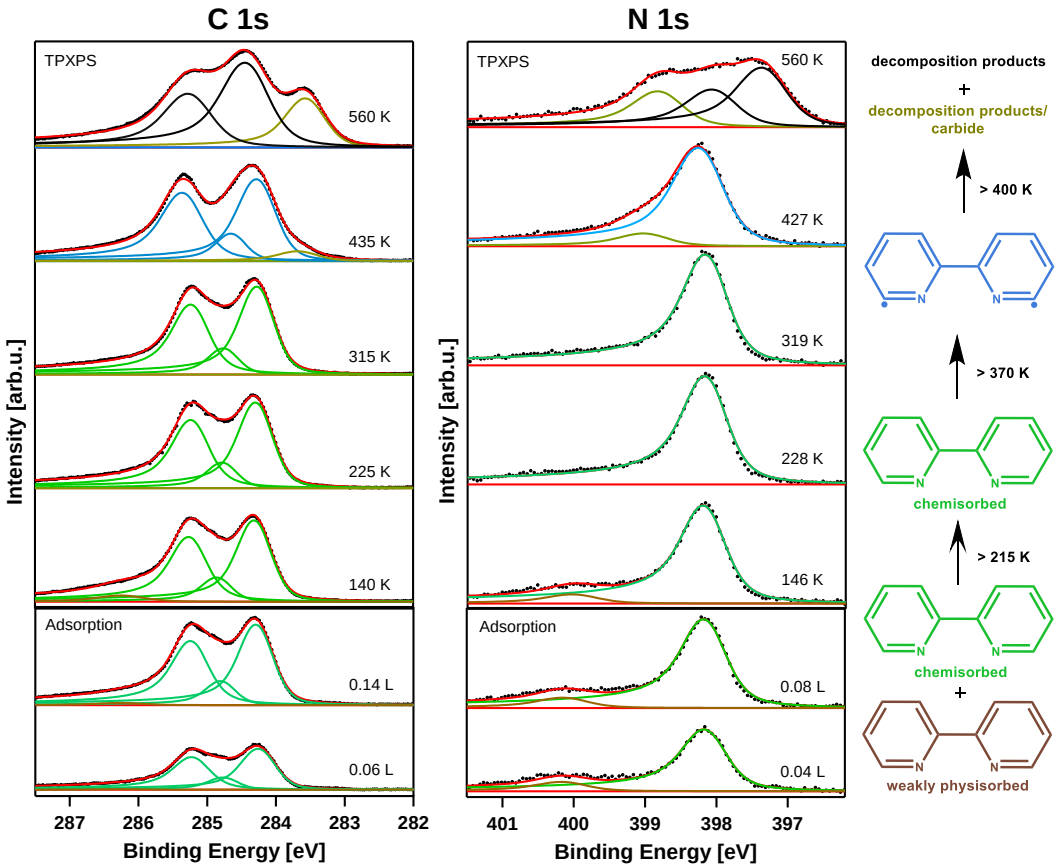

Figure 25: Selected C 1s (hν = 380 eV, left) and N 1s (hν = 500 eV right) XP spectra for 2,2'-bipyridine on Ni(111). T_{ads}: 130 K; heating rate: 0.5 K/s.

Representative spectra collected during adsorption are presented at the bottom and spectra of the subsequent heating experiments (TPXPS) at the top.

Adsorption of BiPy on Ni(111) at 130 K leads to three signals in the C 1s region at 284.30, 284.84 and 285.24 eV, which grow linearly with increasing exposure. The three signals are fitted with a constant intensity ratio of 1 : 0.3 : 0.9 throughout the adsorption experiment. A clear assignment of the signals to specific carbon atoms in the molecule is difficult due to the complexity of the molecule and possibly non-uniform adsorption sites.[108] However, high binding energies typically indicate the proximity to an electron withdrawing heteroatom such as nitrogen.[168] Moreover, a very weak signal is found at 286.22 eV, which is tentatively assigned to a physisorbed species on top of the first chemisorbed layer. The growth of weakly adsorbed multilayers is very typical for molecular adsorbates, e.g., it has also been reported for the adsorption of pyridine on Pt(111).[169] In the N 1s region, the adsorption of BiPy at 130 K yields a signal at 398.12 eV, which is assigned to the two chemically equivalent nitrogen atoms. The small peak at

400.10 eV is tentatively again assigned to physisorption of 2,2'-bipyridine, in analogy to the C 1s region. This assignment is further supported by the similar binding energy of 400.30 eV observed for physisorbed pyridine on Pt(111).[169]

Subsequently, we performed TPXPS in both regions, that is, we heated the sample from 130 to 600 K with linear heating rates of 0.5 K/s while continuously recording XP spectra. The corresponding quantitative analysis is presented in Figure 26. Upon heating, the small peak at 286.22 eV in the C 1s region with a carbon coverage of 0.035 ML decreases and vanishes at 190 K, which confirms our assignment as weakly bound physisorbed species. At the same time, the coverage corresponding to the three other BiPy signals increases by the same amount, that is, from 0.63 to 0.66 ML. A similar behavior is seen in the N 1s region, where the small peak at 400.10 eV with a nitrogen coverage of 0.06 ML decreases and vanishes at 215 K, while the main N 1s signal is growing from 0.070 to 0.076 ML.

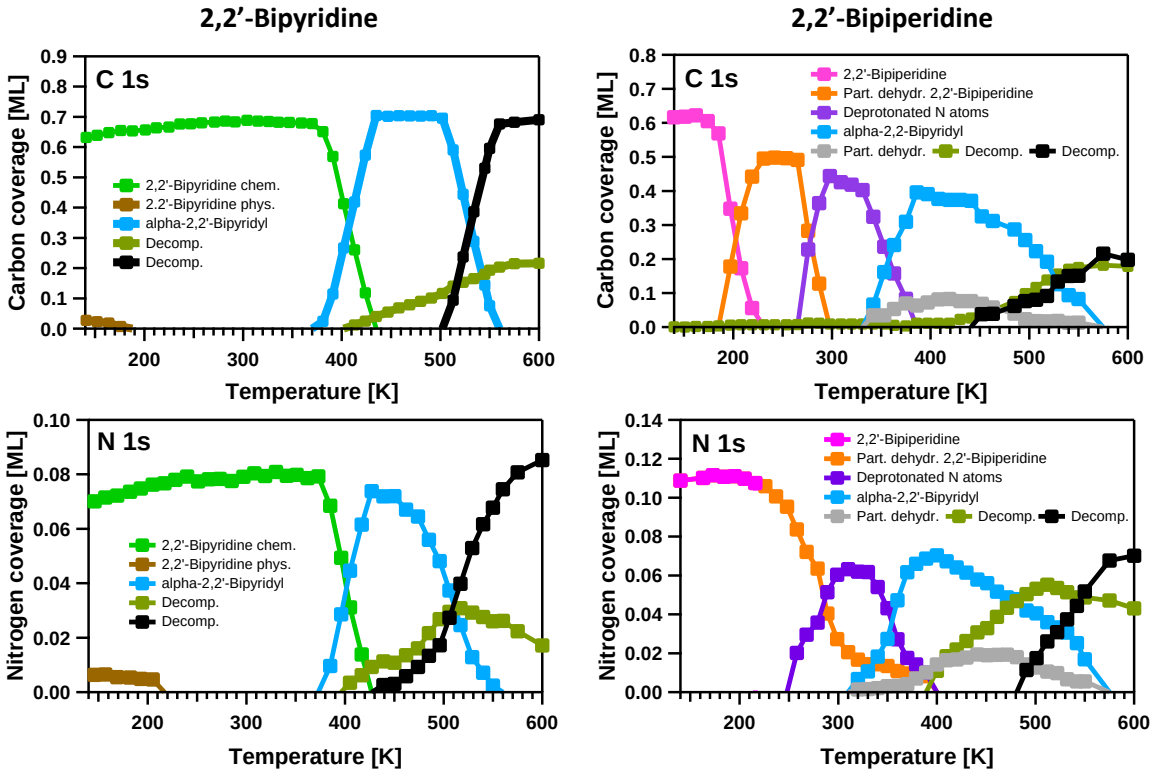

Figure 26: Quantitative analysis of the C 1s (top) and N 1s (bottom) experiments for 2,2'-bipyridine (left, data from Figure 25) and 2,2'-bipiperidine (right, data from Figure 29) on Ni(111).

We propose that physisorbed molecules are immobile at low temperature and upon heating do not desorb but rather move to vacant surface sites of the not completely filled

chemisorbed layer. Notably, we can rule out that the increasing signal intensities for the chemisorbed species are caused by desorption of the physisorbed layer and reduced damping, since e.g. in the C 1s region 0.035 ML physisorbed 2,2'-bipyridine are estimated to cause only less than 0.01 ML attenuation.

To obtain information on the adsorption geometry of BiPy, we performed NEXAFS measurements at the carbon K-edge. The corresponding spectra at normal (NI, 0°; red) and gracing incidence (GI, 70°; black) are shown in Figure 27a. They were recorded in separate experiments after the adsorption of a submonolayer coverage (0.45 ML) of 2,2'-bipyridine at 130 K, and subsequent heating to 300 K to avoid the presence of physisorbed species. The π* resonances at 283.8 and 284.5 eV display weak intensity at NI, but are significantly more intense at GI.

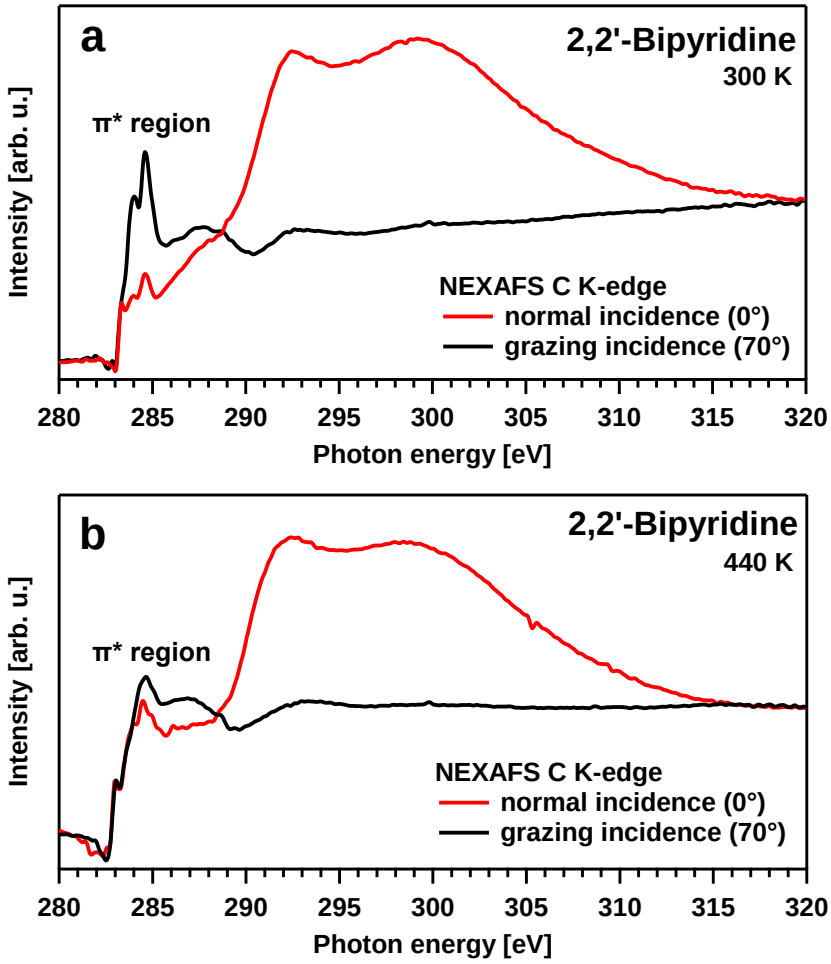

Figure 27: Normal (0°) and grazing (70°) incidence NEXAFS spectra at the C K-edge at 300 K (a) and 440 K (b) of 2,2'-bipyridine. The spectra are recorded in partial electron yield (PEY) mode.

This characteristic behavior indicates, that the π-system of BiPy is oriented close to parallel to the surface plane, resulting in a nearly flat-lying or slightly tilted compound. The small intensity minimum at 282.5 eV in the NEXAFS spectra might be caused by carbon impurities on the monochromator of the beamline.

Further heating to 370 K leaves the C 1s and N 1s XP data in Figure 25 unchanged. Above 370 K, we observe pronounced changes for both regions, indicating the formation of a new species through a chemical reaction. In the C 1s region, we observe new signals at 284.24, 284.61 and 285.32 eV, which results in a slightly broader overall width of the spectra. In the N 1s region, the signal shifts only by +0.07 eV to 398.19 eV. The new species reaches its highest surface coverage in both regions at around 420 K; see Figure 26.

Additional insight in this first reaction step is provided by the hydrogen TPD spectrum (m/z = 2) in Figure 28a. The first peak of the spectrum at 340 K (indicated by a dashed green line) is an artefact, due to adsorption of hydrogen from the background.

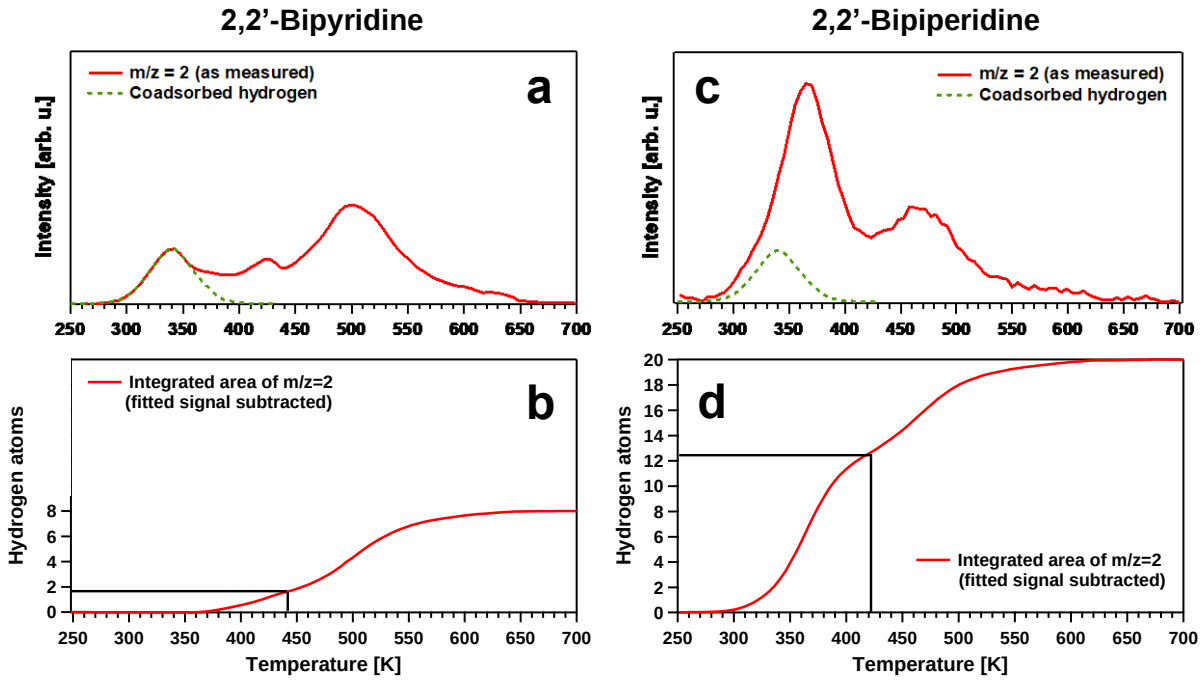

Figure 28: TPD experiments (m/z = 2) of 2,2'-bipyridine (a, b) and 2,2'-bipiperidine (c,d) on Ni(111) with a heating rate of 3 K/s (top). The peaks at 340 K (dashed green line) is due to background adsorption of H_2 from the background pressure. This peak is subtracted from the TPD spectra (in a and c) for the evaluation of the integrated m/z = 2 signals (b and d), which are normalized to the total number of hydrogen atoms (8 in b and 20 in d).

The first BiPy-related desorption peak is found at 425 K. The integrated intensity of this desorption signal up to 440 K (Figure 28b) corresponds to the desorption of approximately two hydrogen atoms (that is, one hydrogen molecule).

From the combined XPS and TPD data, we thus assign the new species formed by abstraction (and desorption) of two hydrogen atoms to a α-BiPy species, which is dehydrogenated in both rings at the secondary carbon atoms in α-position to the nitrogen atoms. This type of dehydrogenation was also proposed for pyridine in previous studies for platinum and nickel surfaces.[169-172] Indeed, in a separate heating experiment of pyridine on Ni(111), which is shown in Figure 29, we find a binding energy of 398.13 eV at ~420 K, which we assign to an α,α-pyridyl species. This species is dehydrogenated at both carbon atoms in α-position to the nitrogen atom and is structurally similar to α-pyridyl, which was suggested in different surface studies.[170, 172] Thus, the binding energies of the proposed α-BiPy (398.19 eV) and α,α-pyridyl (398.13 eV) species on Ni(111) are very similar. It is noteworthy to mention that 2,2'-bipyridine can be synthesized from pyridine in presence of a *Raney nickel* catalyst.[173] In this reaction, pyridine is dehydrogenated in α-position, before a new C-C bond between the two six-membered rings is formed. This may indicate a strong acidity of this particular C-H bond.

The α-BiPy species is found to be stable up to around 450 K, as concluded from both core level spectra; see Figure 25. We assume that the C-C bond between the two six-membered rings is still intact at this temperature and no α,α-pyridyl is formed. This assumption is based on Figure 29, which shows a comparison between N 1s spectra of 2,2'-bipyridine, 2,2'-bipiperidine and pyridine on Ni(111) at ~420 K. For pyridine, at this temperature, the formed α,α-pyridyl species shows a narrower peak shape than the proposed α-BiPy signal, which we attribute to the smaller size of α,α-pyridyl and the resulting more homogeneous local chemical environment. In order to obtain information on the adsorption geometry of α-BiPy, we performed NEXAFS experiments in NI and GI at 440 K; see Figure 27b. The NI experiment at 440 K shows slightly larger signals in the π* region compared to the spectra at 300 K. At GI, the situation is reversed, that is, slightly lower π* signals are found at 440 K, compared to 300 K. This behavior indicates that α-BiPy is tilted, likely with the nitrogen atoms pointing to the surface. We assume, that the tilting of the compound is more favorable, after the hydrogen atoms in α-position to the nitrogen atoms are dehydrogenated.

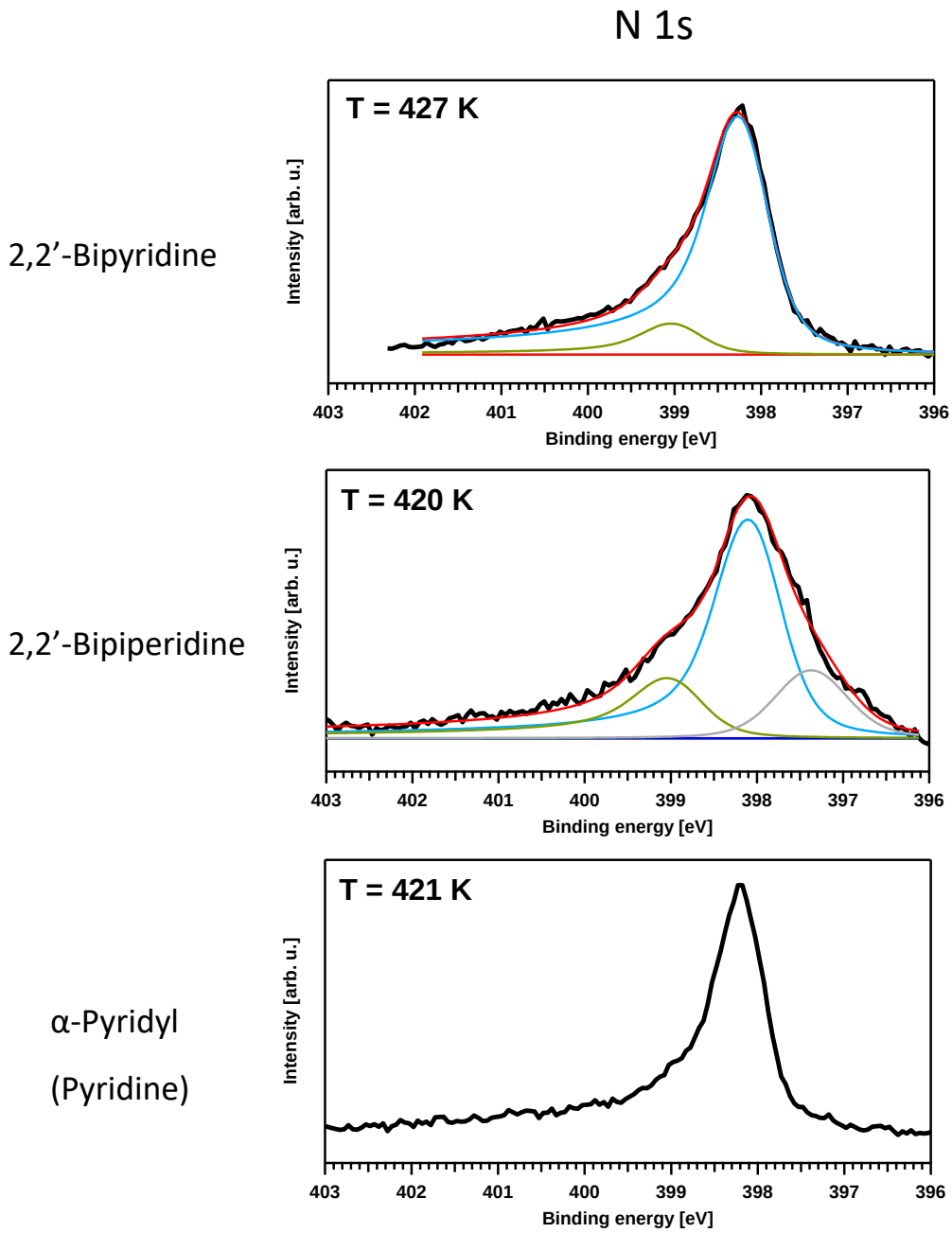

Figure 29: Comparison of XP spectra in the N 1s region of 2,2’-bipyridine, 2,2’-bipiperidine and pyridine at ~420 K on Ni(111). At this temperature, pyridine has reacted to an α,α-pyridyl species. The α-2,2’-bipyridyl species (blue) in the reactions of 2,2’-bipyridine and 2,2’-bipiperidine features a significantly broader peak shape. Therefore, a scission of the C-C bond between two six-membered rings in the reactions of 2,2’-bipyridine and 2,2’-bipiperidine is unlikely.

The XP spectra of both regions in Figure 25 show the onset of decomposition of α-BiPy already at 405 K. This decomposition process is revealed by the growth of a shoulder in the C 1s region at 283.64 eV. With increasing temperature, this peak shifts to lower

binding energies and reaches 283.48 eV at 600 K; it is assigned to the formation of nickel carbide. The decomposition is also evidenced in the nitrogen spectra with a new rising signal at 398.98 eV. This signal shifts to lower binding energies with increasing temperature and reaches 398.71 eV at 600 K. A clear assignment of the signal in the N 1s region to a specific decomposition compound is difficult. However, a ring opening reaction at the nitrogen atom (C-N bond cleavage) at this temperature is likely. Starting at 440 K, an additional N 1s signal grows at 397.38 eV, indicating an additional decomposition product. Above 500 K, the decomposition into fragments is reflected by the rise of C 1s signals at 284.39 and 285.26 eV. The decomposition is also evident from a large hydrogen desorption signal in the TPD spectrum at 500 K. Such a decomposition of the hydrogen-lean LOHC molecule is undesired and has to be avoided. Therefore, a further analysis of the decomposition products at higher temperatures was not performed.

To sum up this chapter, at low temperatures we observe physisorption on top of the first layer during the adsorption of 2,2’-bipyridine. These weakly adsorbed layers move to vacant surface sites at 215 K. The flat lying 2,2’-bipyridine is dehydrogenated in α-position to the nitrogen atoms above 370 K, resulting in a tilted adsorption geometry. Further heating above 400 K results in a decomposition of the compound.

5.2.2. 2,2’-Bipiperidine

In this section, we address the adsorption and reaction of the hydrogen-rich LOHC compound 2,2’-bipiperidine (BiPip) with the molecular formula $C_{10}H_{20}N_2$. For the analysis of the dehydrogenation mechanism, we will use the fingerprint spectra gained for 2,2’-bipyridine by TPXPS in the last chapter.

Figure 30 shows representative C 1s spectra (left, 0.64 L, 0.62 ML carbon) and N 1s spectra (right, 0.78 L, 0.11 ML nitrogen) of BiPip during adsorption (bottom) and subsequent heating (top).

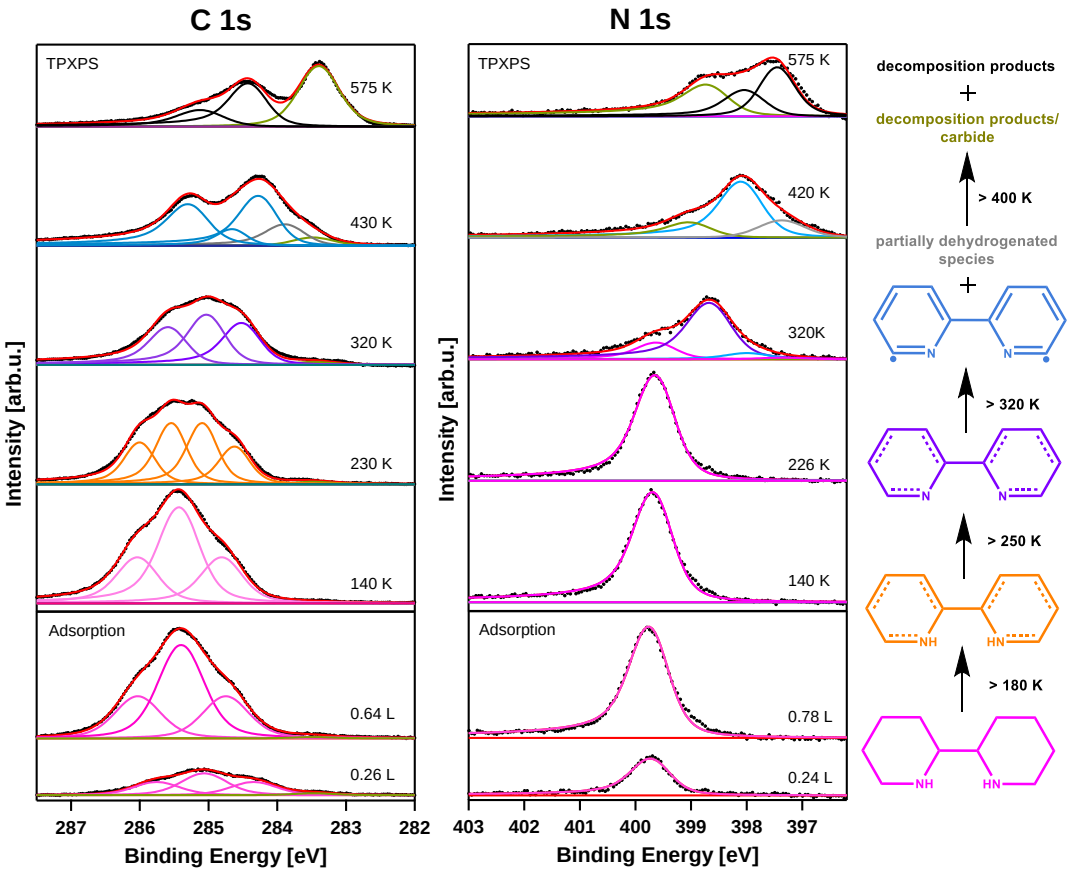

Figure 30: Selected C 1s (hν = 380 eV, left) and N 1s (hν = 500 eV, right) XP spectra for 2,2'-bipiperidine on Ni(111). T_{ads}: 130 K; heating rate: 0.5 K/s.

Upon exposure to 2,2'-bipiperidine, three signals grow in the C 1s region at 284.34, 285.06 and 285.75 eV with a constant intensity ratio of 1 : 2.2 : 1 to the final carbon coverage of 0.62 ML. With increasing coverage, the signals shift to higher binding energies and reach 284.75, 285.40 and 286.03 eV at a carbon coverage of 0.62 ML. Due to the complexity of the molecular structure, an assignment of the signals to specific carbon atoms is again difficult. Nevertheless, as mentioned in the previous section, high binding energies typically indicate the neighborhood to an electron withdrawing nitrogen atom. The very weak signal at 283.48 eV is assigned to small amounts of nickel carbide. In the N 1s region, we observe the growth of only one signal at 399.72 eV, which is assigned to the two equivalent aminic nitrogen atoms. The position of the signal remains unchanged up to a nitrogen coverage of 0.11 ML. For BiPip, we did not perform NEXAFS experiments, since the absence of π* resonances would make a clear interpretation difficult.

After the adsorption of BiPip, we applied a linear heating ramp and simultaneously recorded XP spectra. A quantitative analysis of the corresponding C 1s and N 1s spectra is

presented in Figure 26. In the C 1s spectra, we observe characteristic changes starting at 190 K, indicative of a first reaction step. Altogether four peaks at 284.61, 285.08, 285.53 and 285.99 eV with a signal height ratio of approximately 1 : 2 : 2 : 1 are necessary to fit the spectrum of the new species. The transformation to the new species is accompanied by a decrease in carbon coverage from initially 0.62 to 0.50 ML at 250 K, which is assigned to a partial molecular desorption of BiPip.

The nitrogen coverage shows a similar decrease, that is, from initially 0.11 to 0.085 ML at 250 K. In contrast to the C 1s region, the peak shape and peak position remain, however, unchanged. This finding suggests that while the first reaction step strongly affects the carbon atoms, it has no or only minor influences on the chemical state of the nitrogen atoms. We therefore assign this first reaction step to a partial dehydrogenation at the carbon atoms. Very likely, this dehydrogenation takes place at carbon atoms which are not in the direct vicinity of the nitrogen atom. Notably, we indicate the transition from the fully to the partially dehydrogenated 2,2'-bipiperidine species by a change in the color of the symbols (from pink to orange) in the quantitative analysis of the N 1s spectra in Figure 26. The TPD data shown in Figure 28 do not provide additional insights into the ongoing reactions, as this partial dehydrogenation occurs below the desorption temperature of hydrogen on Ni(111).[162, 174]

Further heating to above ~260 K leads to an again different signal pattern in the C 1s region, which can be described with three peaks at 284.49, 285.00 and 285.56 eV, indicating the formation of a new surface species. This reaction step is also reflected in the nitrogen spectra by a new signal at 398.63 eV. The shift of the main N 1s signal to lower binding energies by 1.09 eV indicates a significant change in the chemical environment of the nitrogen atoms, that is, a deprotonation at the nitrogen atoms. From our data, we are not able to distinguish, whether the nitrogen atoms are dehydrogenated simultaneously or consecutively. The new species reaches its highest surface coverage at around 310 K in both regions. From the fact that the XP spectra in both regions differ significantly from that of the 2,2'-bipyridine experiment, we exclude the formation of the hydrogen-lean LOHC compound at this temperature. Notably, a small nitrogen signal of pristine 2,2'-bipiperidine at 399.72 eV is observed up to 390 K, where it disappears together with the deprotonated species.

Above 320 K, a new N 1s signal starts to grow in Figure 30 at 398.15 eV, which matches the signal at 398.19 eV found in the 2,2'-bipyridine experiment at the same temperature. We thus assign this newly formed product to the same α-BiPy species proposed in the previous section. The small shoulder at 397.37 eV, which grows in parallel with the α-BiPy species, is assigned to a side product. In the C 1s region, the observed spectra appearance can also be fitted with exactly the same fitting parameters as for the α-BiPy species in the 2,2'-bipyridine experiment (Figure 25), that is, with three signals at 284.24, 284.61 and 285.32 eV. In addition, a small signal at 283.83 eV shows the presence of a side product as was already indicated in the N 1s region. This side product may be assigned to a compound that is partially dehydrogenated at the carbon atoms. One possibility is the formation of a π-allylic species. Such π-allyls have been identified as stable surface species during the dehydrogenation of other LOHC compounds.[151, 175-176] For the N-heterocyclic compound octahydroindole on Pt(111), signals attributed to such π-allyl signals were found at 283.9 eV.[151]

The TPD spectrum in Figure 28c provides additional insights in the dehydrogenation behavior. We observe a large hydrogen desorption signal at 360 K and a smaller signal at 460 K. At the desorption minimum between the two signals at 425 K, around 12 hydrogen atoms have desorbed from the surface (Figure 28d); this corresponds to the number of hydrogen atoms, which are released upon full dehydrogenation of all 2,2'-bipiperidine molecules to form the α-BiPy species.

Above 400 K, decomposition of the α-BiPy species sets in, as concluded from the growing carbide signal in the C 1s region at 283.48 eV, which shifts to slightly lower binding energies at higher temperatures; see Figure 30. This beginning decomposition is also observed in the N 1s region above 400 K with a growing signal at 399.05 eV, which shifts to 398.79 eV at around 470 K. Above 450 K, a further decomposition into fragments is monitored in the C 1s region with the growth of signals at 284.39 and 285.08 eV. This decomposition into fragments is in line with the second hydrogen desorption signal at 460 K.

To sum up this section, 2,2'-bipiperidine is partially dehydrogenated at the carbon atoms above 180 K. This process is only observed in the C 1s region. Above 250 K, the nitrogen atoms are deprotonated. Further heating to above 320 K leads to the formation of

α-2,2’-bipyridyl, which is accompanied by a species that is partially dehydrogenated at the carbon atoms. Above 400 K, the onset of decomposition is found.

5.3. Conclusions

We investigated the surface reaction of the LOHC system 2,2’-bipyridine/ 2,2’-bipiperidine on Ni(111) using synchrotron-based high-resolution TPXPS and NEXAFS along with TPD. The hydrogen-lean 2,2’-bipyridine forms weakly adsorbed multilayers on top of a first chemisorbed layer, which move to vacancies in this layer at ~215 K. Above 370 K, flat-lying 2,2’-bipyridine is dehydrogenated in α-position to both nitrogen atoms at the secondary carbon atoms, which leads to the formation of α-2,2’-bipyridyl and a slightly tilted adsorption geometry. Decomposition sets in at 400 K and is completed above 550 K. The hydrogen-rich 2,2’-bipiperidine is dehydrogenated partially above 180 K and deprotonated at the nitrogen atoms above 250 K. Starting at 320 K, an α-2,2’-bipyridyl species is observed, similar to the species found in the TPXPS of the hydrogen-lean LOHC compound. The desorption maximum of hydrogen was observed at 360 K. As a side product, we identified a species that is partially dehydrogenated at the carbon atoms. The decomposition sets in above 400 K and leads to a complete fragmentation above 550 K.

6. Pyridine, Piperidine, Pyrrole, Pyrrolidine on Ni(111)

Abstract: Liquid organic hydrogen carriers (LOHCs) enable chemical storage of hydrogen under ambient conditions. Recent studies proposed N-heterocyclic compounds such as dodecahydro-N-ethylcarbazole and octahydroindole as suitable LOHCs. In this chapter, we focused on the more simple N-heterocyclic LOHC pairs piperidine/pyridine and pyrrolidine/pyrrole, as these compounds are relatively cheap and are used in a wide range of industrial applications. Nickel is an earth abundant and cheap catalyst that is used in dehydrogenation reactions. Therefore, the two LOHC pairs were investigated on Ni(111) as a model catalyst and their temperature-induced dehydrogenation and reaction mechanisms were studied with synchrotron-based high-resolution XPS and TPD experiments. We found, that the dehydrogenation of both hydrogen-rich compounds occurs on Ni(111). In the piperidine (H_2 storage capacity: 7.0 wt%) experiments, the dehydrogenation product α-pyridyl is found besides the hydrogen-lean LOHC compound pyridine above 290 K. An undesired side reaction leads to minor amounts of a ring opening product. Pyrrolidine (H_2 storage capacity: 5.6 wt%) reacts to an α-pyrrolyl species above 270 K. Pyrrole molecules are not detected in the reaction of pyrrolidine, as a further dehydrogenation step to α-pyrrolyl happens at the same temperature.

6.1. Introduction

In this chapter, we focus on simpler LOHC compounds than in Chapter 4 and 5. They only consist of five- and six-membered rings, and contain only one nitrogen atom. Nickel was chosen as catalyst material, as it is used in large scale in dehydrogenation reactions and is relatively cheap, compared to platinum group metals.[153-154]

In the following, we present our results of the model catalytic studies of the LOHC pairs piperidine/pyridine and pyrrolidine/pyrrole on Ni(111). We used synchrotron-based high-resolution XPS (HR-XPS) and temperature programmed desorption (TPD) to study the reaction mechanism of all four compounds and to find intermediates and decomposition products. In comparison to previous studies on the two LOHC candidates, pyrrole and pyrrolidine, our experiments reveal more in-depth insights into the reaction steps at elevated temperatures (≤600 K).[163, 171-172] In our study, we also address the question, if five- or six-membered N-heterocyclic ring system are better suited as LOHC compounds. In Figure 31, the simplified reaction mechanisms of the LOHC pairs piperidine/pyridine and pyrrolidine/pyrrole are presented.

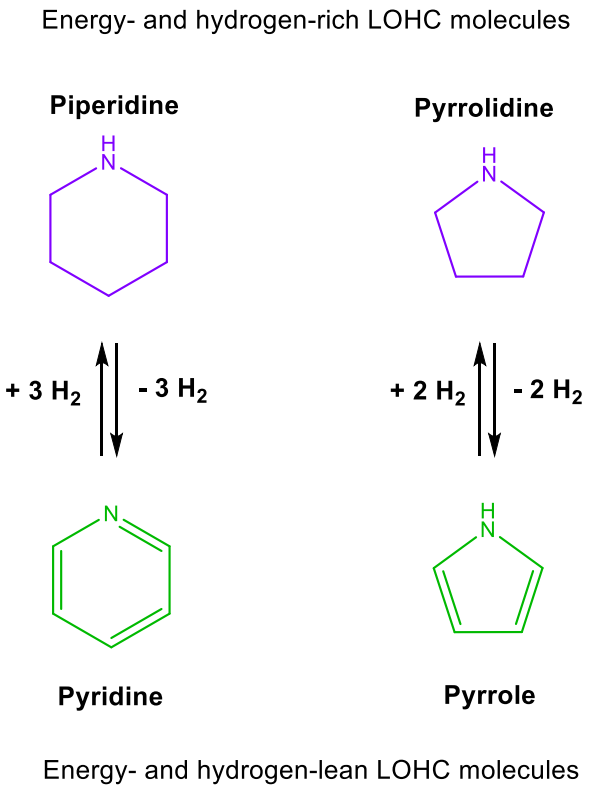

Figure 31: Simplified scheme of the dehydrogenation reaction of piperidine to pyridine and pyrrolidine to pyrrole.

The complete dehydrogenation of pyrrolidine to pyridine yields six hydrogen atoms. The dehydrogenation of pyrrolidine to pyrrole releases four hydrogen atoms.

6.2. Results and discussion

6.2.1. Pyridine

Pyridine is the hydrogen-lean molecule in the proposed LOHC cycle. The six-membered ring has the molecular formula C_5H_5N and a melting point of -42 °C. An intact molecular framework of the hydrogen-lean compound is necessary in a functioning LOHC cycle. Therefore, the thermal stability limits of pyridine are discussed in this section. Moreover, characteristic fingerprint spectra of pyridine and its reaction products help us to understand the reaction mechanism of the hydrogen-rich counterpart piperidine. Pyridine was adsorbed in two standalone experiments, which leads to slightly different surface coverages in the XPS experiments of the carbon and nitrogen region.

XP spectra of the heating experiments of pyridine in the C 1s (a, 0.65 ML carbon, 0.12 L) and N 1s (b, 0.078 ML nitrogen, 0.22 L) region are presented in Figure 32.

The adsorption of pyridine on Ni(111) at 130 K yields two signals at 284.25 and 284.89 eV (higher asymmetry) with a signal area ratio of around 2:3 (284.25 : 284.89 eV) in the carbon region. The signal at 284.89 eV is assigned to the two equivalent carbon atoms in neighborhood to the nitrogen atom, whereas the signal with a relatively high asymmetry at 284.25 eV is assigned to the remaining three carbon atoms in distance to the nitrogen atom. Conclusions on the adsorption geometry of pyridine are difficult to draw from the XP spectra, but from Raman experiments it is known, that pyridine chemisorbs in a flat-lying and π-bonded fashion on Ni(111) below room temperature.[172] In the nitrogen region, see Figure 32b, the growth of two signals at 398.12 and 400.18 eV is observed. The major signal at 398.12 eV is assigned to flat-lying pyridine. We propose that the minor signal at 400.18 eV is assigned to small amounts of differently adsorbed and upright standing pyridine molecules. The nitrogen atom could be sigma-bonded to the surface, leading to an upright standing adsorption geometry and a shift to higher binding energies. We exclude the presence of water on the surface, as discussed in the TPXPS below.

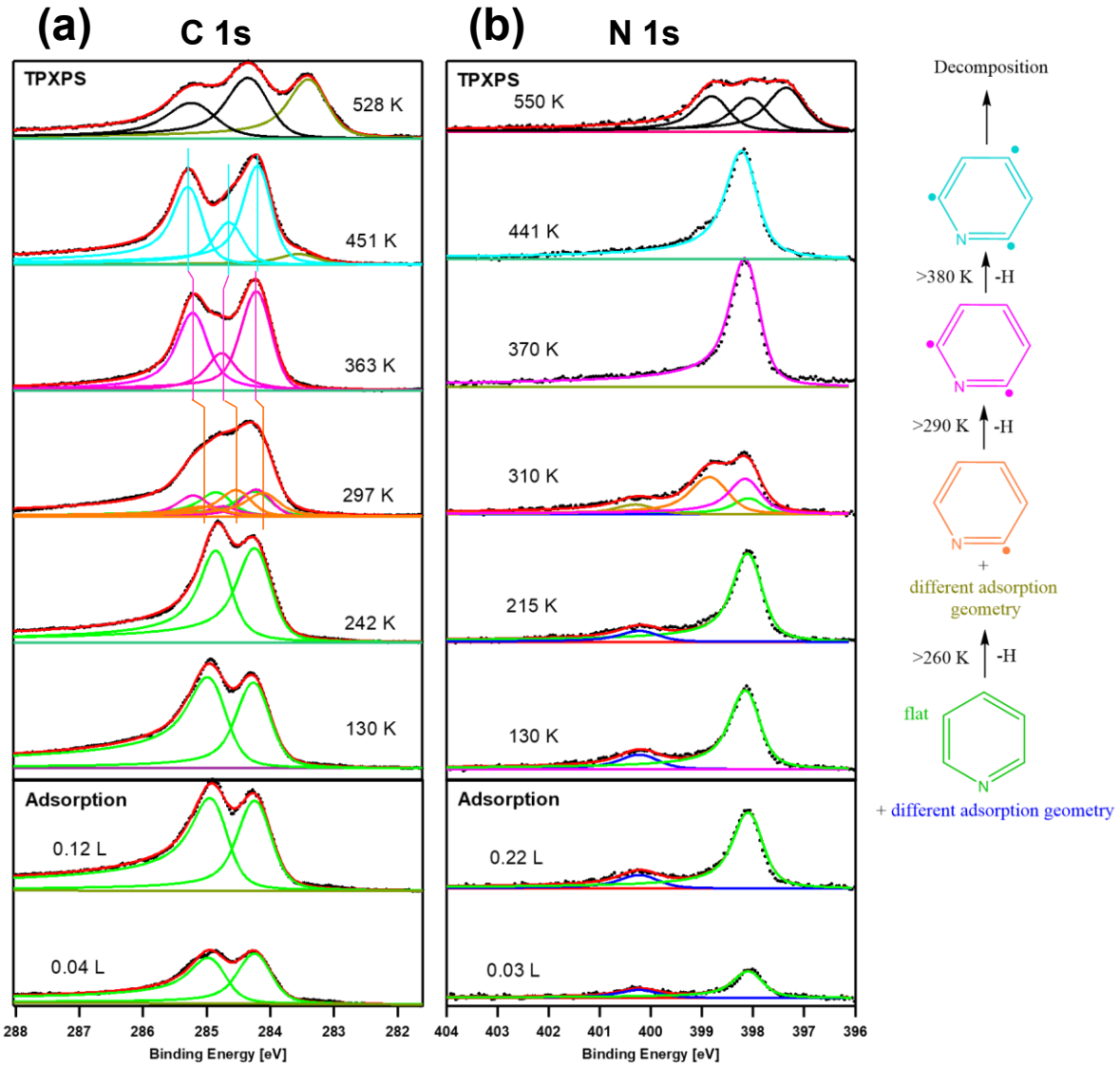

Figure 32: Selected C 1s (a) and N 1s (b) XP spectra for pyridine on Ni(111).

It is unlikely, that the small signal at 400.18 eV is caused by the growth of multilayer islands, as the signal is visible at already low coverages. For multilayer island growth to start, the surface has to be pre-covered with adsorbate molecules first. The small amounts of the proposed upright standing pyridine molecules cannot be clearly resolved in the carbon region.

Heating to above 260 K leads to a first reaction step that is visible in the XP spectra of both regions. A new signal at 398.81 eV is growing in the nitrogen region and gains its maximum intensity at around 310 K, which is shown in the quantitative analysis of the XP spectra in Figure 33b.

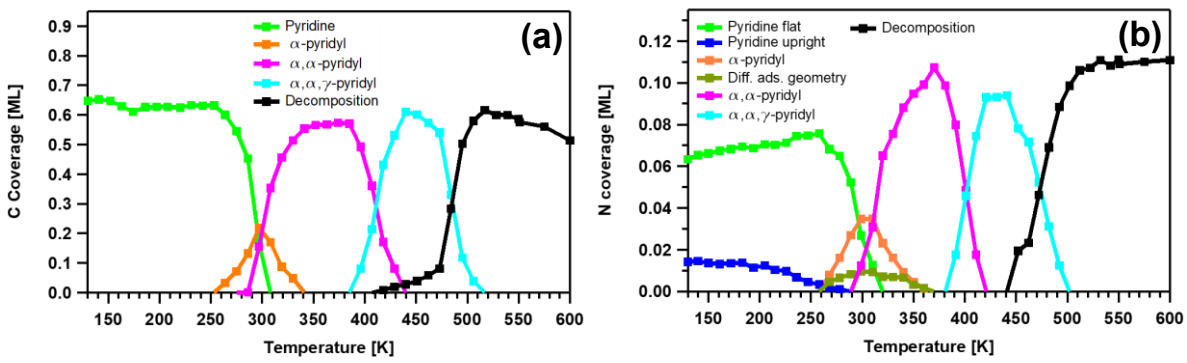

Figure 33: Quantitative analysis of the TPXPS experiments of pyridine on Ni(111) in the C 1s (a) and N 1s (b) regions shown in Figure 32.

This species is assigned to an α-pyridyl species, which is dehydrogenated in α-position to the nitrogen atom and is standing upright or tilted on the nickel surface.[172] Such an α-pyridyl product was detected by surface Raman spectroscopy at room temperature, in good agreement with our experiment.[172] The α-pyridyl species is bound to the nickel surface with its nitrogen atom and the dehydrogenated carbon atom in α-position. The dehydrogenation in α-position is also indicated by the left shoulder (~340 K) of the dehydrogenation signal at 380 K in the TPD (m/z = 2) spectrum in Figure 34. The start of the hydrogen desorption is shifted to higher temperatures compared to the XPS data, as hydrogen desorption from nickel only starts at around 300 K and also depends on the surface coverage of hydrogen.[174] The integrated area (normalized to the number of hydrogen atoms) of the TPD spectrum indicates that at 370 K one out of five hydrogen atoms has left the surface. This is in good agreement with the XPS data, as the α-pyridyl species is visible up to a temperature of 370 K. Also in the temperature region of the 1st reaction step, the small signal at 400.18 eV shifts to a slightly higher binding energy of 400.26 eV above 260 K. This new binding energy position is either assigned to an upright standing pyridine species, which is sigma-bonded with the nitrogen atom to the nickel surface or the minor shift to higher binding energies could be caused by the change of the co-adsorbed species (from flat-lying pyridine to upright standing α-pyridyl). In the carbon region, the α-pyridyl species is fitted with three signals at 284.08, 284.49 and 285.01 eV. Please note, that a reliable fitting of the signals in this temperature range is challenging, as the short-lived α-pyridyl species overlaps with the signals of pristine pyridine and the next evolving species (α,α-pyridyl).

A 2nd reaction step is observed above 280 K. In the nitrogen region one signal at 398.12 eV (the same binding energy as for flat-lying pyridine) evolves and in the carbon region three signals at 284.20, 284.75 and 285.20 eV with a signal height ratio of 2:1:2 are found. This species gains its highest intensity at around 370 K, which coincides with a peak in the TPD spectrum at the same temperature. This suggests a further dehydrogenation of the α-pyridyl species. The signal height ratio of 2:1:2 in the carbon region indicates that there are two sets of two chemically equivalent carbon atoms and a 3rd chemical environment for the one remaining carbon atom. A plausible conclusion is that the second carbon in α-position is also dehydrogenated to form an α,α-pyridyl species. The three signals in the carbon region correspond to two chemically equivalent α-carbon atoms (285.20 eV), two chemically equivalent carbon atoms in β-position (284.25 eV) and one carbon atom in γ-position to the nitrogen atom (284.75 eV) (see Figure 32a, C 1s). This dehydrogenation product has its maximum coverage at 410 K in the nitrogen region and at 430 K in the carbon region. This is in good agreement with the TPD experiment, where two hydrogen atoms have desorbed from the nickel surface at around 410 K.

The next reaction step starts at 380 K, as we see the development of a new signal pattern in the C 1s region with peaks at 284.18 (β-C), 284.62 (γ-C) and 285.25 eV (α-C). The most obvious change in comparison to the peak structure of the α,α-pyridyl species is the shift of the γ-carbon atoms signal to lower binding energies. As we also monitor a dehydrogenation peak at 420 K in the TPD spectrum, we propose a further dehydrogenation of the compound in γ-position to the nitrogen atom.

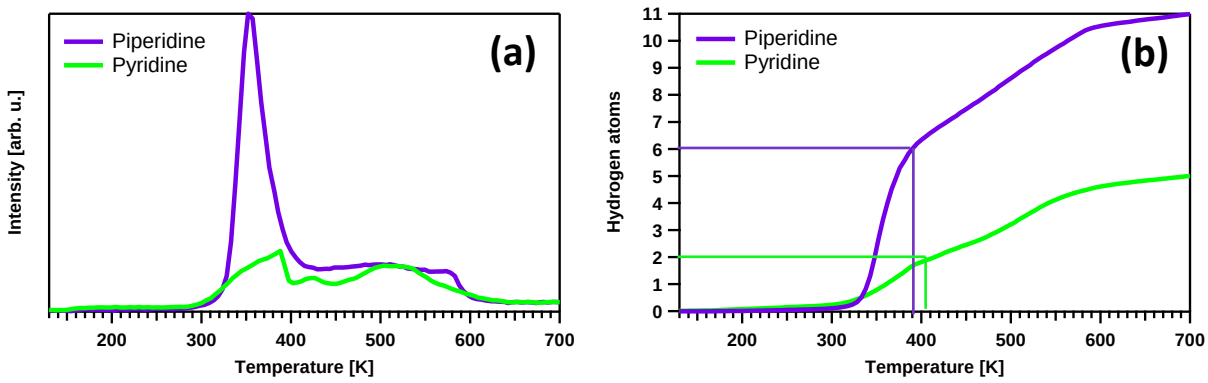

Figure 34: TPD experiments (m/z = 2) of pyridine and piperidine on Ni(111) with a heating rate of 3 K/s (a) and integrated area normalized to the total number of hydrogen atoms for pyridine and piperidine (b).

Above 410 K, a decomposition of the remaining carbon ring occurs as witnessed by a growing signal in the C 1s region at 283.49 eV. This signal shifts to 283.35 eV at around 550 K and is assigned to nickel carbide. Moreover, we observe a shift of the two main carbon signals at 285.18 and 284.25 eV. The signal at 285.18 eV shifts to 285.11 eV at 550 K and the signal at 284.25 eV to 284.36 eV. In the N 1s region, the decomposition is monitored above 450 K by the rise of signals at 397.45, 388.16 and 398.94 eV. The latter shifts by 0.2 eV to lower binding energies at around 550 K.

6.2.2. Piperidine

Piperidine is the hydrogen- and energy-rich compound in the proposed LOHC cycle. The molecule has the molecular formula $C_5H_{11}N$ and a melting point of -10 °C. A dehydrogenation of six hydrogen atoms from piperidine leads to the formation of the hydrogen- and energy-lean LOHC molecule pyridine. Like in the previous section, the compound was adsorbed in two separate experiments, leading to different surface coverages in the XPS experiments of the carbon and nitrogen region.

The XP spectra of the heating experiments of piperidine in the C 1s (a: 0.49 ML carbon, 0.22 L) and N 1s (b: 0.050 ML nitrogen, 0.3 L) region are shown in Figure 35.

During the adsorption of piperidine on Ni(111) at 130 K, the main signal is growing at 399.62 eV and a small signal at 401.65 eV in the N 1s region. The main signal at 399.62 eV is assigned to piperidine, whereas the signal at 401.65 eV is assigned to a water-induced feature, which is caused by co-adsorbed water. It forms hydrogen bonds with the hydrogen atom at the nitrogen and leads to this shift in binding energy. In the carbon region, we observe the growth of three signals at 284.89, 285.51 and 286.67 eV upon adsorption. The weak signal at 286.67 eV is assigned to the same water-induced feature that was witnessed in the nitrogen region. Both signals vanish at the desorption temperature of the co-adsorbed water (see TPXPS). The carbon peaks at 284.89 and 285.51 eV have a signal area ratio of close to 1:4. Typically, carbon signals appear at higher binding energies, when they are located in vicinity to electron-withdrawing heteroatoms like nitrogen. Additionally, a non-planar molecule like piperidine could possibly have a relatively weak / non-specific binding to the metal surface. This could

result in a weak screening of the core hole and a signal shift to higher binding energy. As a result, a clear assignment of the carbon signals to specific carbon atoms is not possible.

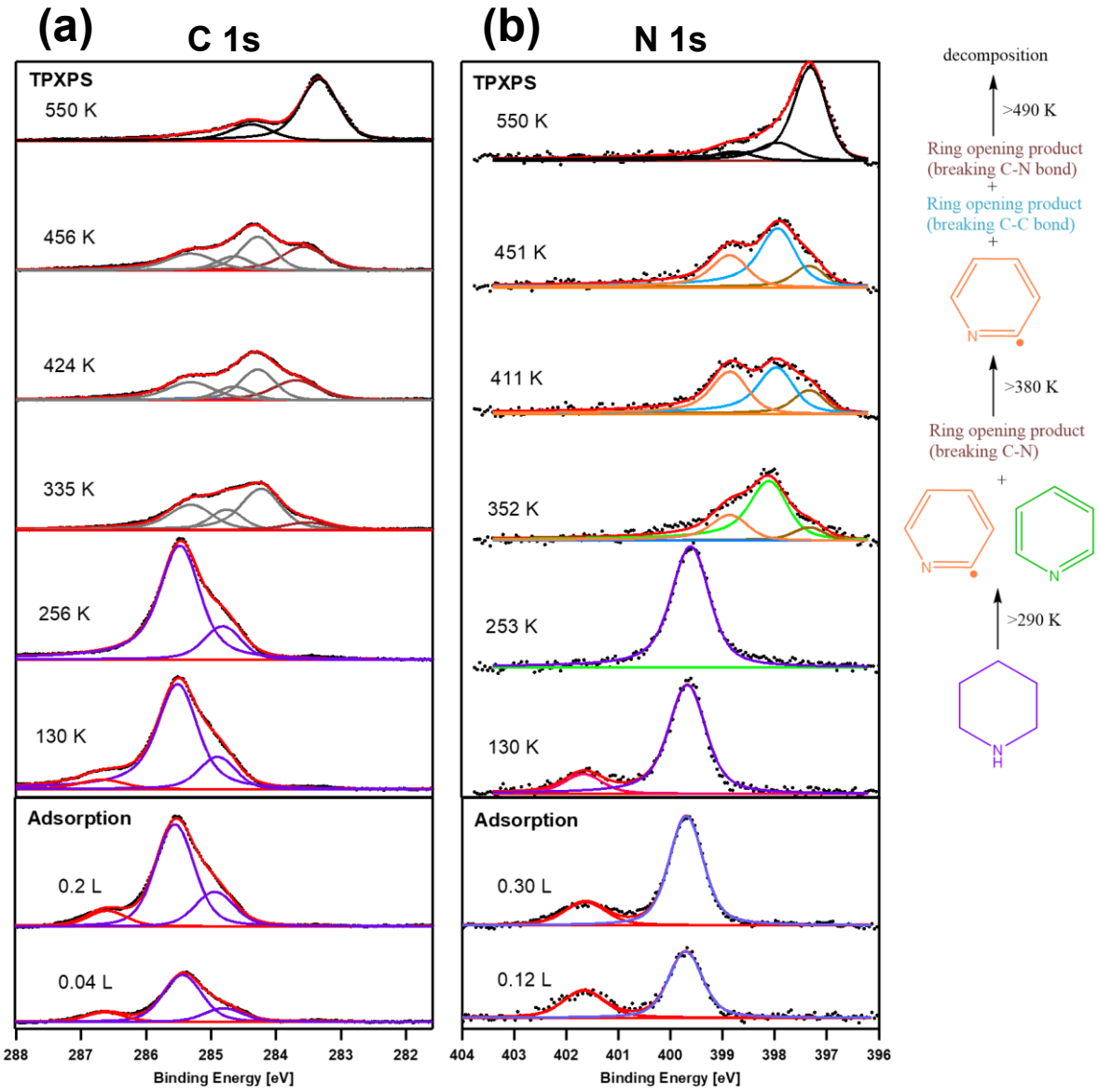

Figure 35: Selected C 1s (a) and N 1s (b) XP spectra for piperidine on Ni(111).

Overall, the peak shapes of piperidine in both regions differ significantly from those in the pyridine experiment, which enables a clear distinction of the hydrogen-rich and hydrogen-lean compounds. After the adsorption experiments, the heating experiments in both regions were recorded. The signals of the water-induced features created by water impurities in both regions (286.67 and 401.65 eV) vanish above 170 K, which is in line with the desorption temperature of water from a Ni(111) surface. At the same time, we see an increase in signal intensities of the remaining piperidine signals in both regions

(see quantitative analysis in Figure 36). Therefore, the total surface coverage of piperidine stays roughly constant.

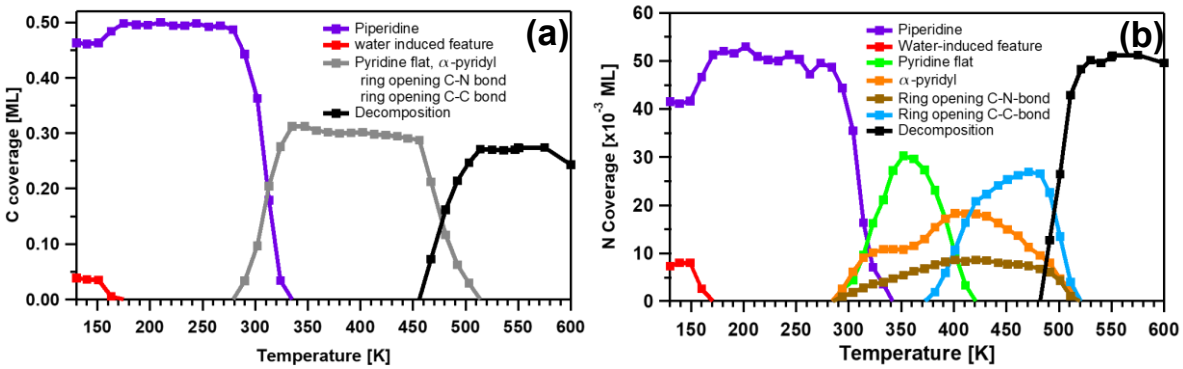

Figure 36: Quantitative analysis of the TPXPS experiments of piperidine on Ni(111) in the C 1s (a) and N 1s (b) regions shown in Figure 35.

The next change in the XP spectra and first reaction step is monitored at temperatures above 280 K in the carbon and the nitrogen region. In the nitrogen region, we see three new signals growing simultaneously at 397.30, 398.07 and 398.82 eV. The signal at 398.82 eV is assigned to an α-pyridyl species, as it matches the binding energy (398.81 eV) of this compound witnessed in the pyridine experiment in the previous section. Moreover, a flat-lying pyridine species is observed like in the previous pyridine experiment with the signal at 398.07 eV. This compound shows the highest surface coverage at around 350 K. The very small shift of 0.05 eV in binding energy between the two experiments is likely caused by the co-adsorption of different compounds in the piperidine experiment. The signal at 397.30 eV is assigned to a species, which is formed by a breaking C-N bond, as the rather large shift to lower binding energies indicates a change in the direct vicinity to the nitrogen atom. In the carbon region, the first reaction step above 280 K leads to a new peak shape in the XP spectra, which is fitted with four signals at 283.51, 284.22, 284.75 and 285.30 eV. Please note that an appropriate fit of the three individual and co-existent species is not possible in the C 1s region. Therefore, the C 1s spectra are colored in grey and are summed up in the quantitative analysis in Figure 36a. However, the existence of the signal at 283.51 eV indicates a beginning decomposition of small amounts of the LOHC compound (breaking of a C-N bond). A beginning decomposition of the molecular framework was observed at almost the same binding energy of 283.49 eV in the previous pyridine experiment above 380 K. During this reaction, we see a falling signal intensity in the quantitative analysis of the C 1s experiment, while the total coverage in the N 1s region stays relatively constant. This

phenomenon might be due to photoelectron diffraction, as the surface species change their adsorption geometry. The dehydrogenation above 280 K in the first reaction step is also monitored in the TPD spectrum (m/z = 2) in Figure 34, where a large dehydrogenation signal is found at around 350 K. At around 400 K, we see the dehydrogenation of around six hydrogen atoms. This is in relatively good agreement with the XP spectra, as we would expect to see a number slightly above six hydrogen atoms due to the formation of mainly pyridine (- 6 H) and smaller amounts of α-pyridyl (-7 H). Above 370 K, we see a decrease in pyridine coverage and the formation of a new reaction product in the N 1s region by a growing signal at 397.90 eV. This new species is likely assigned to a ring opening product formed by a breaking C-C bond in the pyridine molecule, as only a minor shift in binding energy is observed (0.17 eV), indicating a reaction not close to the nitrogen atom. During this reaction, the decomposition signal in the carbon region shifts from 283.51 to 283.66 eV and gains in intensity. Above 460 K, a total decomposition is observed in the nitrogen region through signals at 397.28, 397.90 and 398.75 eV. In the carbon region, this decomposition is monitored by signals at 283.32, 284.37 and 285.19 eV above 480 K.

The experiments showed that a dehydrogenation of piperidine to pyridine (-6H) and α-pyridyl (-7H) is possible on Ni(111) at around 350 K. However, both dehydrogenation products are accompanied by small amounts of a decomposition product, which amounts to around 12 % of the total surface coverage at 350 K and is likely formed by the cleavage of a C-N bond.

6.2.3. Pyrrole

Pyrrole has the chemical formula C_4H_5N, a melting point of -24 °C and is the desired hydrogen- and energy-lean compound in the LOHC system pyrrole/pyrrolidine. As shown in the previous sections, the XPS experiments of the hydrogen-lean molecule can provide useful fingerprint spectra of the reaction and decomposition products. This facilitates the evaluation of the reaction pathway of the hydrogen-rich LOHC molecule pyrrolidine. In Figure 37, selected C 1s (a: 0.35 ML carbon, 0.27 L) and N 1s (b: 0.15 ML nitrogen, 1.00 L) XP spectra of pyrrole are shown during the adsorption and the subsequent heating experiment. During the adsorption of pyrrole at 130 K on Ni(111), two signals are recorded at 284.40 and 285.12 eV in the carbon region and are assigned to the molecular

adsorption of pyrrole. The signal at 285.12 eV is assigned to α-carbon atoms in close vicinity to the nitrogen atom, whereas the signal at 284.40 eV is assigned to carbon atoms in β-position. We expect that the pyrrole molecule is lying flat on the surface in a π-bonded configuration at low temperatures, as was shown experimentally for pyridine.[172]

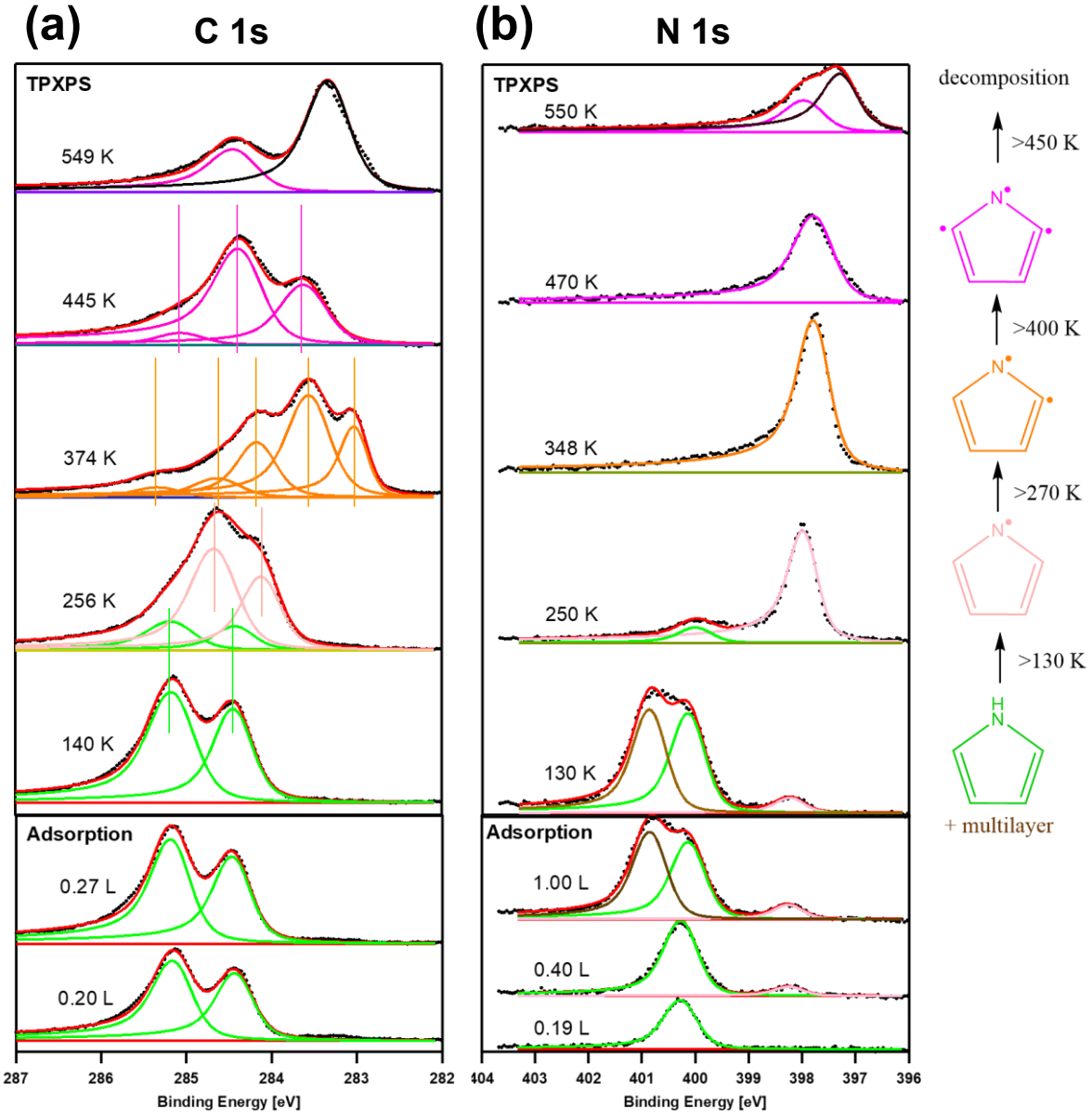

Figure 37: Selected C 1s (a) and N 1s (b) XP spectra for pyrrole on Ni(111).

In the nitrogen region, the main signal grows at 400.21 eV and is assigned to molecular pyrrole. Additionally, a minor signal at 398.09 eV occurs during the adsorption at exposures above 0.35 L. We assign this signal to a first reaction product (see TPXPS). It was shown in previous XPS studies on LOHC compounds that a dehydrogenation at the nitrogen atom can lead to a shift of almost 2 eV in the nitrogen region.[177] Consequently, this first reaction step at already 130 K is assigned to a dehydrogenation at the nitrogen

atom, forming a pyrrolide species. However, the formation of this minority species can not be resolved clearly in the carbon region. Furthermore, we observe the formation of a physisorbed multilayer in the nitrogen region at 400.83 eV above an exposure of 0.58 L. Subsequently, the heating experiment with a heating rate of 0.5 K/s was started and XP spectra were recorded. The desorption of the physisorbed multilayer in the nitrogen region occurs above 180 K. The first dehydrogenation reaction at the nitrogen atom (please note that this is the reaction product already observed during adsorption in the N 1s region) only becomes visible above 150 K in the carbon region with the growth of two new signals at 284.10 and 284.65 eV.

These two carbon peaks are assigned to the pyrrolide species. Pyrrolide gains its highest surface coverage at around 280 K in both regions (see quantitative analysis in Figure 38). The pyrrolide signal in the N 1s region shifts with increasing temperature from 398.09 to 397.79 eV.

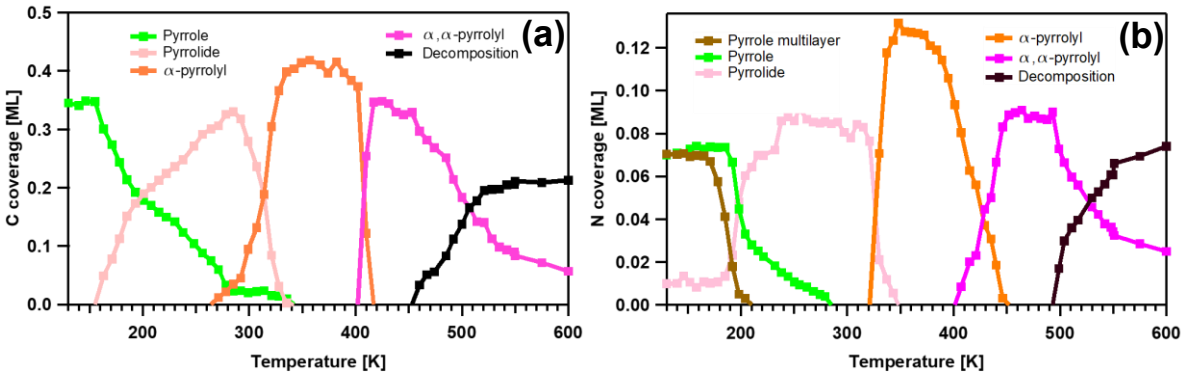

Figure 38: Quantitative analysis of the TPXPS experiments of pyrrole on Ni(111) in the C 1s (a) and N 1s (b) regions shown in Figure 37.

The dehydrogenation at the nitrogen is also witnessed in the TPD spectrum (m/z =2) in Figure 39a, where a hydrogen desorption signal is recorded at 320 K. The hydrogen desorption signal is shifted to higher temperatures in comparison with the onset of the dehydrogenation reaction in the XPS experiments, as hydrogen desorption from Ni(111) starts at ~300 K.[162] Moreover, the surface coverage of hydrogen has an impact on its desorption temperature from nickel surfaces.[162] The pyrrole signals vanish at ~300 K in the nitrogen region, while small amounts of the same species are observed up to 340 K in the carbon region. The formation of a new reaction product is witnessed above 260 K in the C 1s experiment with signals at 283.10, 283.49, 284.15, 284.60 and 285.35 eV.

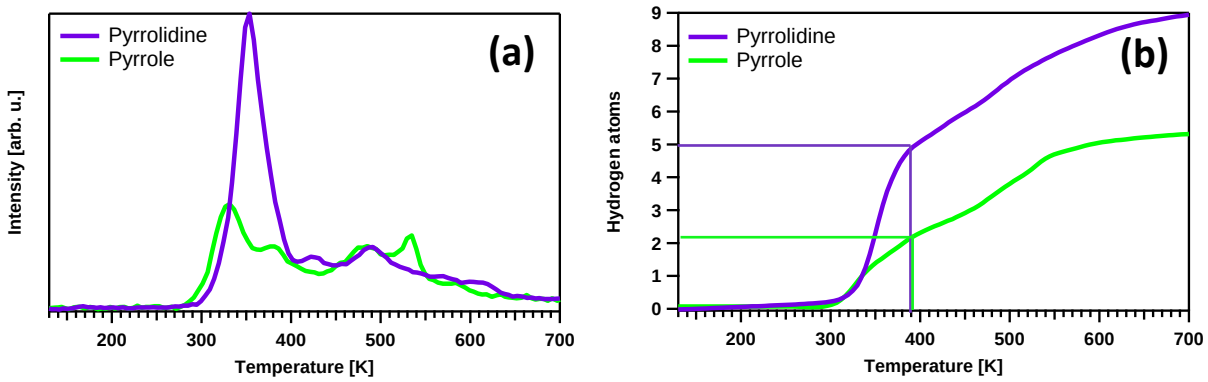

Figure 39: (a) TPD experiments (m/z = 2) of pyrrole and pyrrolidine on Ni(111) with a heating rate of 3 K/s and (b) integrated area normalized to the total number of hydrogen atoms for pyrrole and pyrrolidine.

The maximum surface coverage of this new species is reached at ~360 K. The TPD experiment suggests the cleavage of a second hydrogen atom in this temperature range, as a hydrogen desorption signal is seen at 370 K. We propose the dehydrogenation of a carbon atom in α-position to the nitrogen atom and the formation of an α-pyrrolyl compound, similar to the dehydrogenation of the α-carbon atom in the pyridine experiment. Above 320 K, one major signals at 397.76 eV is observed in the N 1s experiment and is also assigned to an α-pyrrolyl compound. This species has almost the same binding energy as the signal of the precursor pyrrolide (397.79 eV). Interestingly, a significant increase in the total surface coverage is seen in the nitrogen region during this dehydrogenation in α-position to the nitrogen atom. This finding is assigned to a different adsorption geometry and a strong photoelectron diffraction effect due to this change in adsorption geometry. One further reaction product is seen in the carbon region above 400 K by the growth of three new signals at 283.60, 284.33, 285.01 eV. At the same temperature, we also monitor the growth of a new signal in the N 1s experiment at 397.77 eV. In the TPD spectrum, we observe the growth of a hydrogen desorption signal above 430 K. This desorption signal gains its highest intensity at 480 K. Due to the presence of this third hydrogen desorption signal, we expect a further dehydrogenation of the α-pyrrolyl and the formation of an α,α-pyrrolyl species. This α,α-pyrrolyl compound is dehydrogenated at both carbon atoms in α-position to the nitrogen atom. A dehydrogenation of the second α-carbon atom seems favorable due to the electron withdrawing character of the nitrogen atom and the relatively high acidity of the hydrogen atom. The complex peak structure in the C 1s region is not possible to

understand. The fragmentation of the molecule is monitored above 460 K by a new carbon signal at 283.30 eV (carbide) and a signal at 397.25 eV in the nitrogen region. The decomposition is also observed through a hydrogen desorption signal in the TPD spectrum, which peaks at 530 K.

6.2.4. Pyrrolidine

Pyrrolidine represents the hydrogen and energy-rich compound in the LOHC system pyrrolidine/pyrrole. It has the chemical formula C_4H_9N and a melting point of -63 °C. The dehydrogenation of pyrrolidine to pyrrole yields four hydrogen atoms in an ideal LOHC cycle. As in the previous sections, we conducted standalone XPS experiments in the carbon and nitrogen region and recorded TPD data to monitor the dehydrogenation reaction.

In Figure 40, selected XP spectra of the C 1s (a, 0.67 ML carbon, 0.38 L) and N 1s (b, 0.08 ML nitrogen, 0.09 L) region during the adsorption of pyrrolidine and the subsequent heating experiments are presented. Upon adsorption of pyrrolidine at 130 K on Ni(111), only one signal grows in the nitrogen region at 399.69 eV, which shifts to a slightly higher binding energy of 399.85 eV with increasing coverage. This nitrogen signal is assigned to pristine pyrrolidine. In the carbon region, the growth of two signals at 285.02 and 285.60 eV with a signal area ratio of around 1:9 is witnessed during the adsorption. As in the piperidine experiment, the witnessed signal area ratio does not allow for a clear assignment of signals to specific carbon atoms. Like mentioned before, a weak interaction between the non-planar molecule and the metal substrate (electron donor) could result in a weak screening of core holes and a shift to higher binding energy. This could result in overlapping signals of α- and β-carbon atoms.

Subsequently, a heating experiment was started with a heating rate of 0.5 K/s and XP spectra in both regions were recorded. We observe no significant changes in the spectra of both regions below 275 K. Above 275 K, a reaction step is indicated by the growth of signals at 283.05, 283.52, 284.16 and 284.60 eV in the carbon region. A similar signal pattern was observed in the pyrrole experiment at the same temperature and was assigned to α-pyrrolyl.

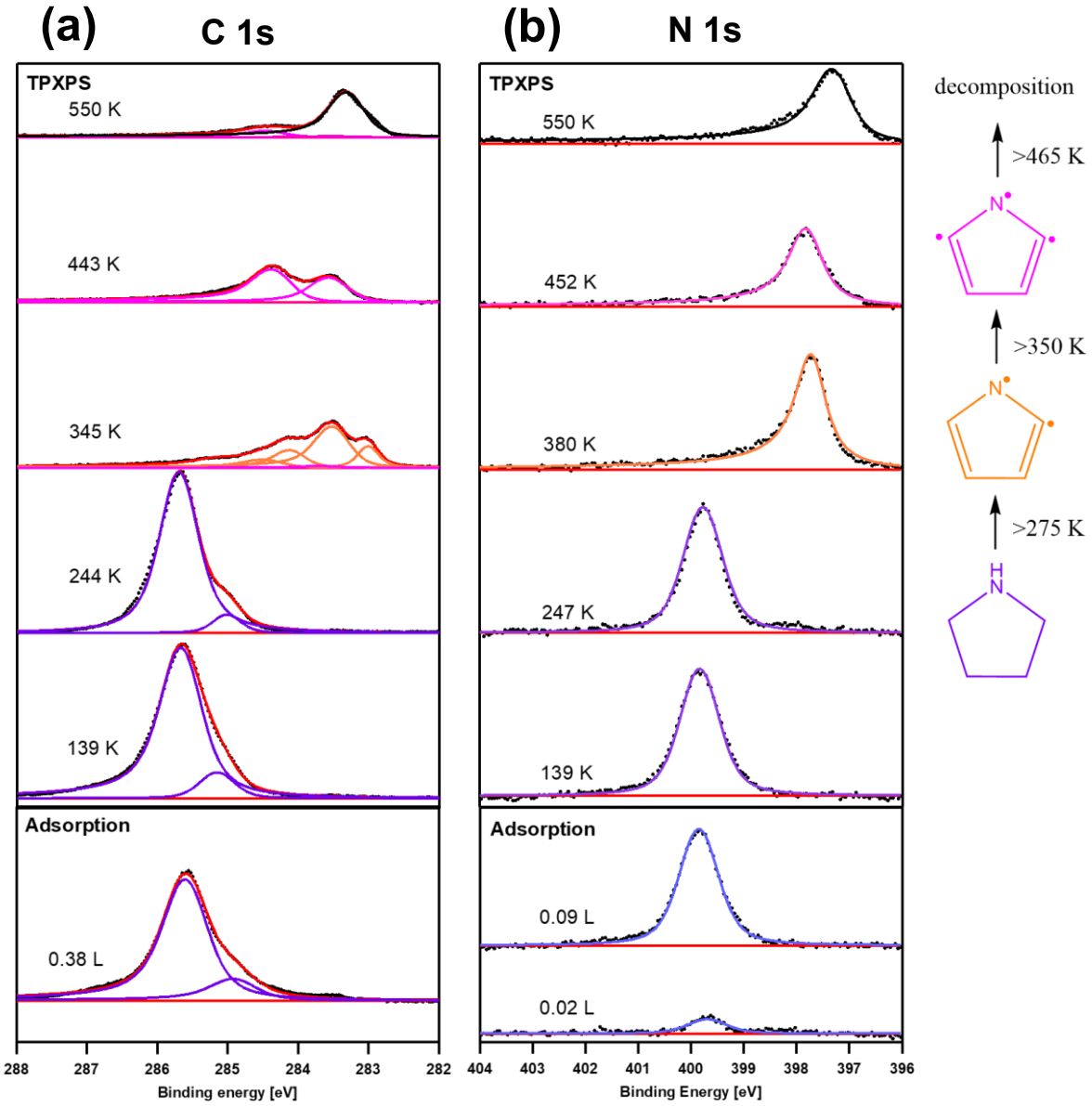

Figure 40: Selected C 1s (a) and N 1s (b) XP spectra for pyrrolidine on Ni(111).

The formation of an α-pyrrolyl species is also seen in the N 1s experiment, as a new signal grows at 397.70 eV. This signal corresponds to an α-pyrrolyl compound, which was found at 397.76 eV in the previous pyrrole experiment. During this first dehydrogenation reaction, the signal intensity in the carbon region decreases significantly from around 0.60 to 0.32 ML (see Figure 41a). In contrast to that, the signal intensities remain relatively constant in the N 1s experiment. Therefore, we exclude a desorption of molecules in this dehydrogenation reaction and assign this phenomenon to the shift in adsorption geometry and photoelectron diffraction. Such a decrease in signal intensities solely in the carbon region was also seen in the first dehydrogenation reaction of the hydrogen-rich piperidine.

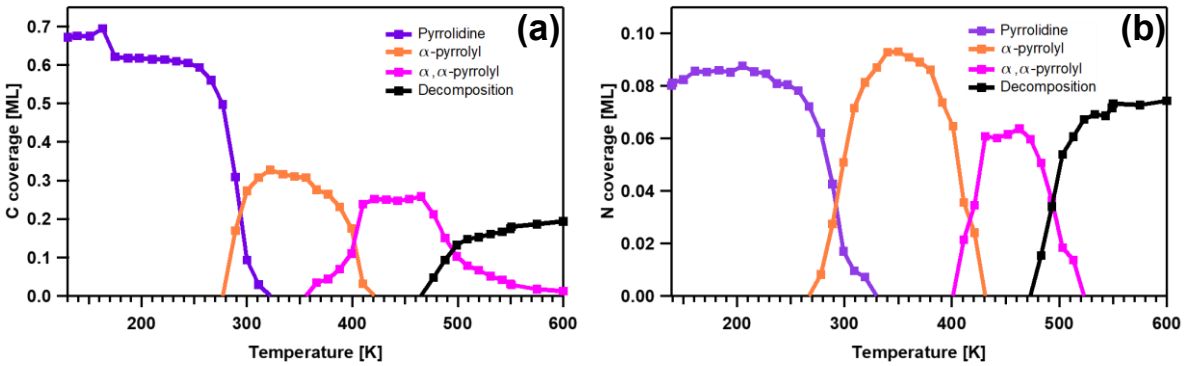

Figure 41: Quantitative analysis of the TPXPS experiments of pyrrolidine on Ni(111) in the C 1s (a) and N 1s (b) regions shown in Figure 40.

The dehydrogenation reaction of pyrrolidine to α-pyrrolyl is detected in the TPD experiment (m/z = 2) in Figure 39 through a large hydrogen desorption signal at 350 K. The onset of the hydrogen desorption signal is shifted by ~10 K in comparison to the first hydrogen desorption signal in the pyrrole experiment. Such a small difference in dehydrogenation temperatures for pyrrole (>270 K) and pyrrolidine (>275 K) is also witnessed in the XPS data. At 390 K, the TPD experiment shows the desorption of five hydrogen atoms. This in relatively good agreement to the six hydrogen atoms, which have to be cleaved from pyrrolidine to form an α-pyrrolyl species. Surprisingly, no formation of pyrrole (-4H) was detected as a precursor for α-pyrrolyl (-6H). Apparently, both dehydrogenation reactions take place simultaneously at the same temperature. Heating above 360 K, produces a new signal pattern in the carbon region with signals at 283.54, 284.33 and 285.00 eV, which resembles the spectra of the α,α-pyrrolyl species in the pyrrole experiment. Moreover, a new signal evolves in the nitrogen region at 397.78 eV and points to the formation of α,α-pyrrolyl. As a consequence, the cleavage of another hydrogen atom in α-position to the nitrogen atom is proposed. This dehydrogenation reaction is also confirmed by a small hydrogen desorption signal at ~420 K in the TPD experiment.

The fragmentation of the molecular framework is recorded in the carbon region with a rising signal at 283.28 eV and the formation of nickel carbide. In the nitrogen region, the decomposition is indicated by a new signal at 397.29 eV.

In Table 1 the binding energies in the carbon region of the presented LOHC molecules are compared. In addition to that, an overview over the reaction pathways of all presented LOHC compounds is shown in Figure 42.

	α-C-atom	β-C-atom	γ-C-atom	not assigned
Pyridine	284.89 eV	284.25 eV	284.25 eV	-
Piperidine	285.51 eV	285.51 eV	284.89 eV	-
Pyrrole	-	-	-	284.40 eV, 285.12 eV
Pyrrolidine	-	-	-	285.02 eV, 285.60 eV

Table 1: Binding energies in the C 1s region of pyridine, piperidine, pyrrole and pyrrolidine after adsorption.

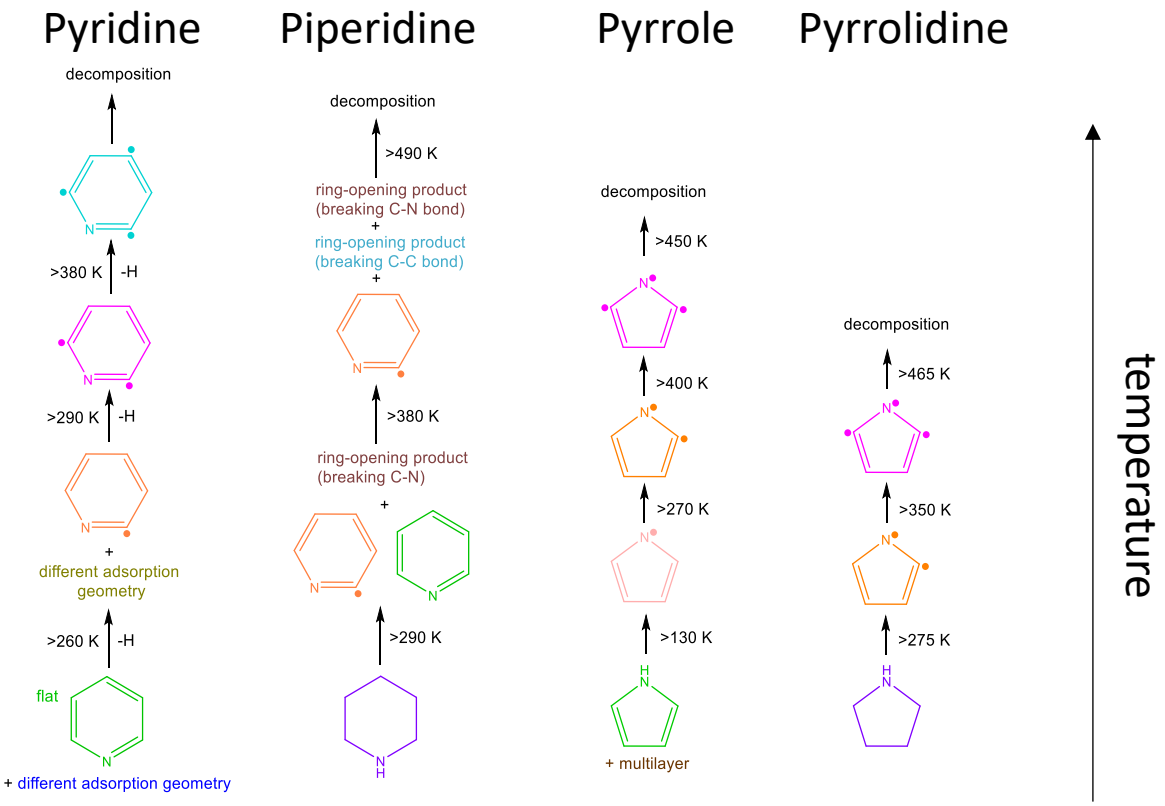

Figure 42: Overview over the reaction pathways of pyridine, piperidine, pyrrole and pyrrolidine on Ni(111).

6.3. Conclusions

We monitored the surface reaction of the LOHC pairs piperidine/pyridine and pyrrolidine/pyrrole using HR-XPS and TPD.

Pyridine is dehydrogenated to α-pyridyl above 260 K and undergoes a further dehydrogenation step above 290 K to form an α,α-pyridyl. This product is dehydrogenated at both carbon atoms in α-position to nitrogen. Further heating above 380 K induces the cleavage of a hydrogen atom in γ-position, before a decomposition into

fragments is seen above 410 K. The hydrogen-rich LOHC molecule piperidine is dehydrogenated to pyridine and an α-pyridyl species above 290 K. Furthermore, a ring opening product (breaking of the C-N bond) is found, which accompanies the α-pyridyl and amounts to 12% of the total surface coverage. Above 380 K, another ring-opening product is found, which is likely formed by the dissociation of a C-C bond. The fragmentation sets in above 490 K.

For both, pyrrolidine and pyrrole, common reaction products were found. The first dehydrogenation product α-pyrrolyl (-6H) is formed above 270 K. Apparently, the dehydrogenation of pyrrolidine to pyrrole (-4H) happens at almost the same temperature (~275 K) as a further dehydrogenation to α-pyrrolyl. Moreover, no side or decomposition products were found at this temperature. A further dehydrogenation at the second carbon atom in α-position to nitrogen atom takes place at ~400 K. The following decomposition into fragments occurs at ~470 K.

Our model catalytic experiments showed that the use of pyrrolidine could be more favorable in a LOHC system, when compared to piperidine, as no ring-opening products are witnessed during the dehydrogenation. This indicates that five-membered N-heterocyclic ring systems have a higher thermal stability than six-membered rings during the dehydrogenation on nickel. This advantage of five-membered ring system, however, comes with a lower hydrogen storage capacity.

In a functioning LOHC system, the hydrogen-lean compound needs to desorb from the surface, which is not the case under model catalytic UHV conditions due to a significant pressure gap. A desorption of dehydrogenated compounds under real catalytic conditions is highly likely, given higher pressures and the competition of molecules towards adsorption sites on the surface.

7. Furan, THF, Benzofuran, Dihydrobenzofuran on Pt(111)

Abstract: Liquid organic hydrogen carriers (LOHCs) enable chemical hydrogen storage in organic molecules under ambient conditions. In these systems, a hydrogen-lean compound is loaded with hydrogen under catalytic conditions to form a hydrogen- and energy-rich species. Upon energy demand, the hydrogen-rich compound is dehydrogenated catalytically. Recent studies identified N-heterocyclic molecules as suitable hydrogen storage materials. In particular, the systems octahydroindole/indole[151-152] and its derivatives H_{12}-N-ethylcarbazole/N-ethyl-carbazole[71] showed thermodynamically favorable properties on platinum catalysts. In order to study the feasibility of O-heterocyclic LOHC systems, this work focuses on the dehydrogenation mechanism of the proposed LOHC pairs tetrahydrofuran/furan and dihydrobenzofuran/benzofuran. High-resolution XPS and TPD lab experiments provided comprehensive insights in the reaction mechanisms on Pt(111) as model catalyst. Both hydrogen-rich compounds are partially dehydrogenated at low temperatures (tetrahydrofuran >140 K, dihydro-benzofuran >150 K). Above 210 K, we found ring-opening products through C-O bond scission for all four probing molecules and the dissociation of CO above 240 K. At higher temperatures, a decomposition of the molecular framework into fragments is observed.

7.1. Introduction

Fossil fuels are a primary energy source and responsible for the emission of greenhouse gases[140] and air pollution[141]. Their main advantages are high energy densities, availability at any given time and easy handling. Renewable energy sources like solar power or wind are expected to replace more and more fossil fuels in the future. However, their use as a primary energy source is still challenging, due to day and night cycles, changing environmental influences and seasonal changes. One further drawback is, that some renewables cannot be deployed profitably worldwide, as their efficiency is highly dependent on their location. For a broad adoption of renewable energy sources, an efficient way of distribution has to be achieved, which can be applied at large scale.

Hydrogen, produced by electrolysis, is one promising energy storage material with a high gravimetric storage density of 33 kWh/kg[178]. Its low volumetric storage density, however, makes a liquefaction at low temperatures (-253 °C) or storage under high pressures necessary. Handling hydrogen under such harsh conditions bears safety issues, like leakages and diffusion through metal walls. These disadvantages can be overcome, when hydrogen is stored chemically, e.g. in so-called liquid organic hydrogen carriers (LOHCs). LOHC systems consist of organic molecules in a hydrogen- and energy-lean and a hydrogen- and energy-rich form. Loading and unloading of the LOHC molecules with hydrogen takes place under catalytic conditions. In an application with a fuel cell or a combustion engine, only the necessary amount of hydrogen is catalytically produced in situ, which minimizes risks. The widely existent infrastructure for the transport and storage of organic substances is also convenient and reduces costs.

N-heterocyclic LOHC systems like H_{12}-N-ethylcarbazole/ N-ethylcarbazole[70-71] have been studied in detail and showed reversibility. Moreover, the reaction mechanisms of the N-heterocyclic LOHC systems octahydroindole/indoline/indole, 2,2'-bipiperidine/ 2,2'-bipyridine, piperidine/pyridine and pyrrolidine/pyrrole have been discussed in the previous chapters. The introduction of a heteroatom like nitrogen weakens neighboring C-H bonds and therefore lowers the dehydrogenation enthalpy[179]. However, some N-heterocyclic LOHC compounds are toxic and dangerous for the environment (indole) or not liquid at room temperature (indole, N-ethylcarbazole). One possible solution for this drawbacks is the replacement of the heteroatom nitrogen by oxygen. This chapter focuses on the feasibility of such O-heterocyclic LOHC systems. We investigated the reaction

mechanism of the dehydrogenation of the proposed LOHC pairs tetrahydrofuran(THF)/ furan and dihydrobenzofuran/benzofuran on Pt(111) under model catalytic UHV conditions. A combination of synchrotron-based high-resolution XPS and lab-based TPD experiments enabled a comprehensive understanding of the reaction pathway.

The proposed dehydrogenation of THF to furan and dihydrobenzofuran to benzofuran is presented in Figure 43. THF has a hydrogen storage capacity of four hydrogen atoms (5.6 wt%) and dihydrobenzofuran of two hydrogen atoms (1.7 wt%).

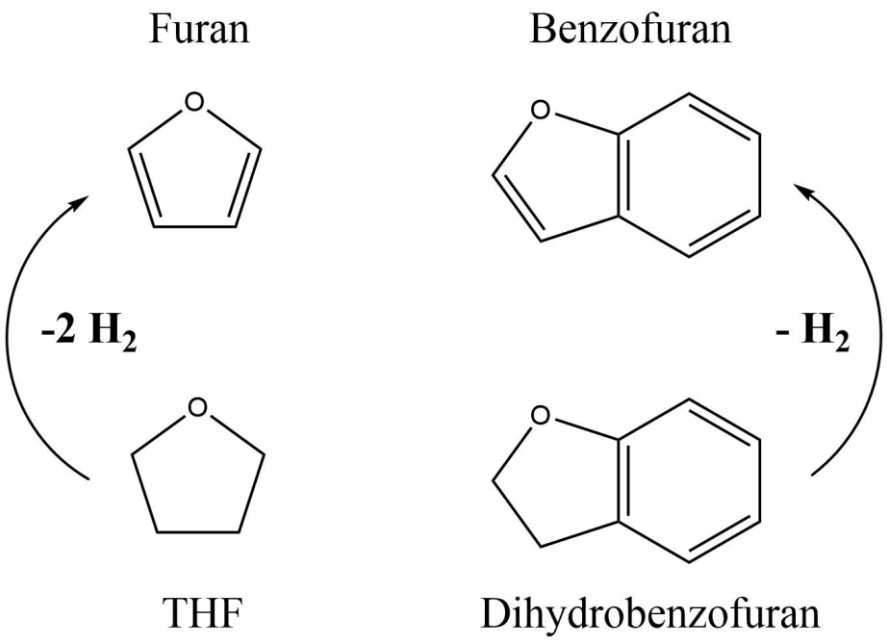

Figure 43: Dehydrogenation of THF to furan (left) and dihydrobenzofuran to benzofuran (right).

7.2. Results and discussion

In this section, the adsorption and reaction of the O-heterocyclic LOHC pairs THF/furan and benzofuran/dihydrobenzofuran is discussed in detail. Selected high-resolution XP spectra of the O 1s and C 1s regions are accompanied by a quantitative analysis and supported by TPD data for the hydrogen-rich compounds. Finally, an extensive reaction pathway for each molecule is proposed.

7.2.1. Furan

Furan represents the hydrogen-lean compound in the LOHC cycle furan/THF and is therefore the desired product in a dehydrogenation reaction of THF. The thermal stability limits of this energy-lean compound are discussed, as they are crucial for the application in a LOHC cycle. Moreover, the determined fingerprint spectra of furan are helpful for the assignment of species in the investigation of the hydrogen-rich THF. XP spectra in the O 1s and C 1s and were recorded in two separately performed experiments and slightly differ in surface coverage.

In Figure 44, representative spectra from the O 1s (a: 0.26 L, 0.19 ML C) and C 1s (b: 0.22 L, 0.17 ML C) region from the adsorption and heating experiment (TPXPS) are presented.

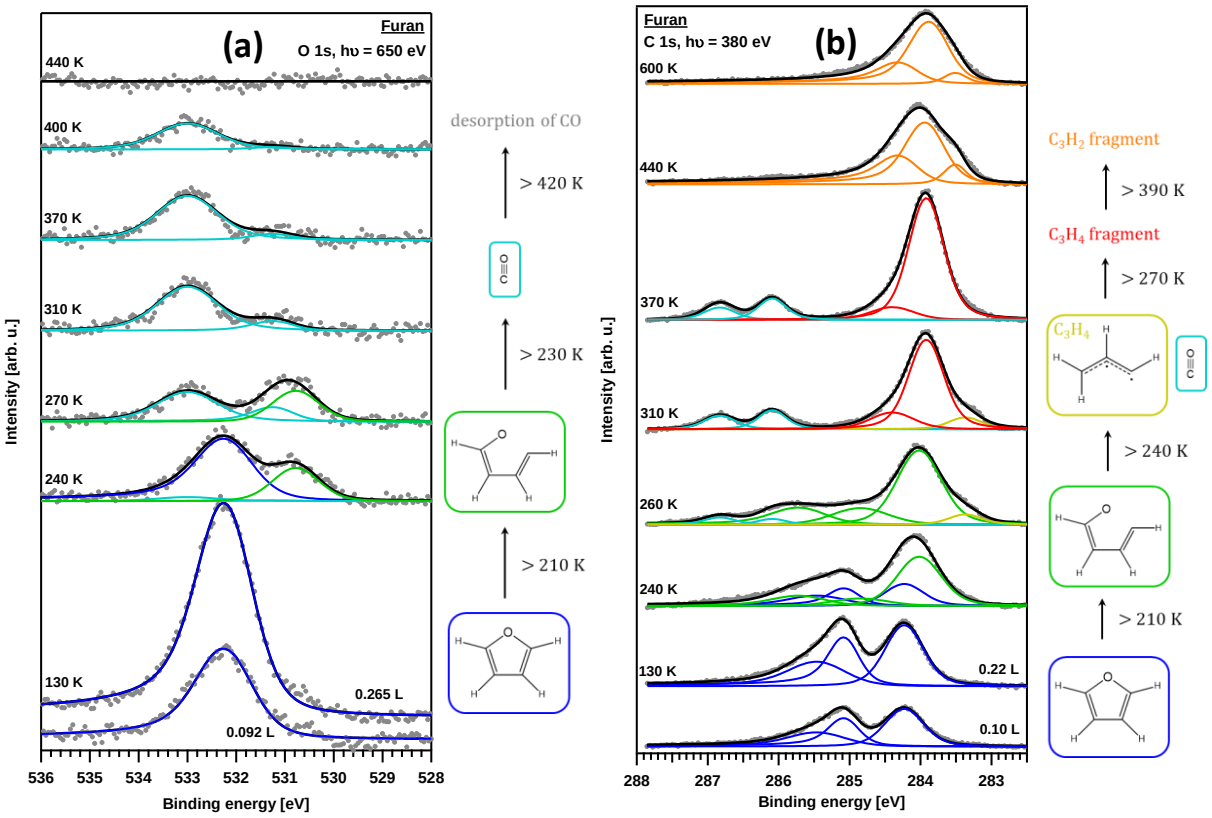

Figure 44: Selected O 1s (a) and C 1s (b) XP spectra for furan on Pt(111).

During the adsorption of furan at 130 K, one signal grows in the O 1s region at 532.2 eV, which is assigned to the single oxygen atom in the molecule. Due to a similar binding energy, we cannot rule out small contributions from water contamination to this signal.[180-181] In the C 1s region, the growth of two signals at 284.2 and 285.1 eV is

observed. The latter signal shows a broad shoulder at around 285.3 eV. The signal at 284.2 eV is assigned to the two carbon atoms, that are distant to the oxygen atom. The carbon atoms in direct neighborhood to the oxygen atom lead to the signals at high binding energy. Adsorption on different adsorption sites is presumably responsible for this splitting into two signals. Moreover, a contribution from satellites is possible, but cannot be clearly resolved. From SFG experiments it is known that furan is lying flat on a Pt(111) surface.[182] During the exposure to furan, the coverage in both regions grows, which can be seen in the quantitative analysis of the fitted signals in Figure 45.

Subsequently, a linear heating ramp was applied, and XP spectra were recorded simultaneously. Right away, the signal intensity in the O 1s region decreases by around 45% to 0.1 ML carbon coverage, which is presumably assigned to the desorption of the contaminant water that desorbs from a clean Pt(111) surface at around 180 K.[183] This behavior is also confirmed by the quantitative analysis in the C 1s region, where no decrease in surface coverage is found for temperatures below 200 K.

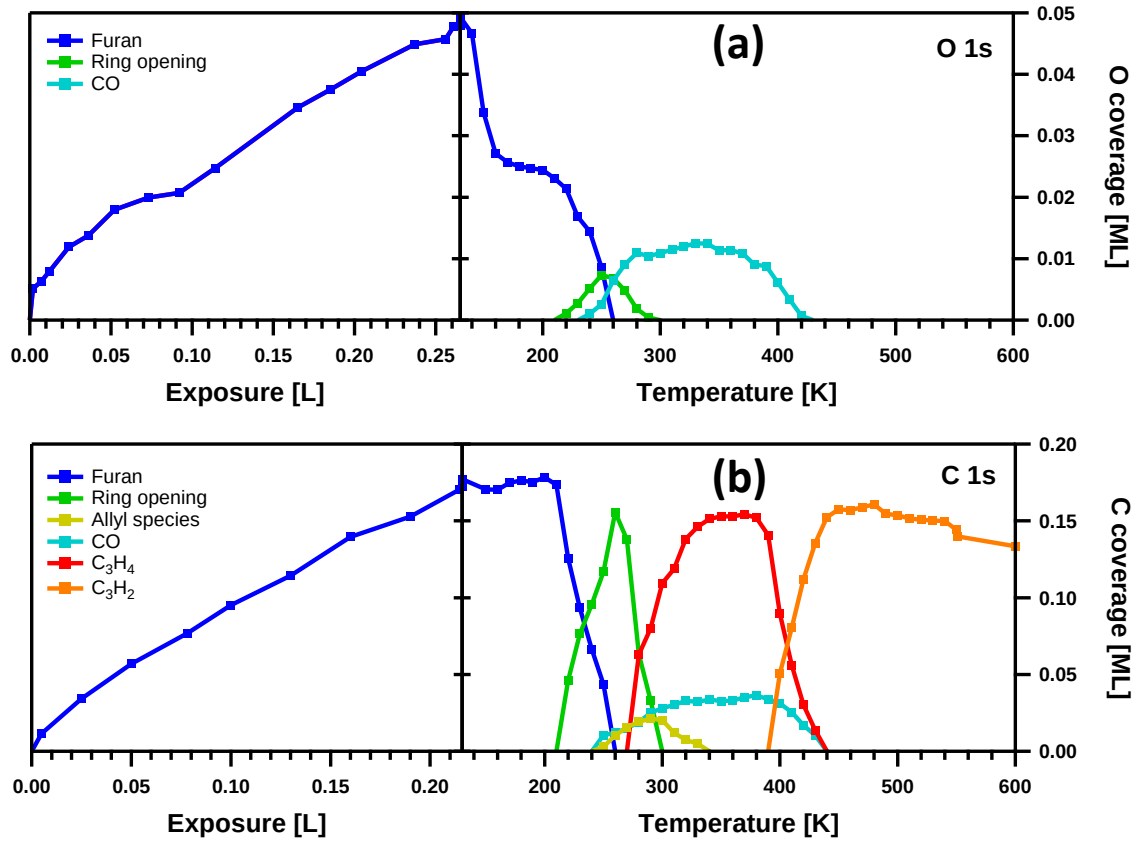

Figure 45: Quantitative analysis of the O 1s (a) and C 1s (b) experiments for furan on Pt(111).

At temperatures above 210 K, a new species is detected in the O 1s core level at 530.8 eV. It is assigned to a ring-opening product with a cleaved C-O bond. At the same temperature, three new signals start to evolve in the C 1s region at 284.0, 284,9 and 285.7 eV, which are also assigned to the newly formed ring-opening product. In both regions, this species gains its highest surface coverage at 250 K and vanishes at around 300 K. At 230 K, two signals start rising in the O 1s region at 531.2 and 533.0 eV. These signals correspond with the formation of CO coordinated at bridge (low binding energy) and on-top sites (high binding energy). The spectral fingerprint of CO on Pt(111) was already investigated and discussed in detail.[184] The formation of CO is also observed in the C 1s core level at 240 K, where two distinct and characteristic peaks grow at 286.1 and 286.8 eV. Please note, that the assignment to the ring-opening product is also partly based on the finding that the second reaction yields CO. At the same temperature, a shoulder at 283.4 eV is resolved in the C 1s region. As CO is split from the ring-opening compound, this newly formed species is assigned to an allyl species with the molecular formula C_3H_4. Studies on platinum catalysts revealed that such allylic species are stable intermediates in surface reactions.[151, 175-176, 185] Above 270 K, two signals at 283.9 and 284.4 eV are observed in the C 1s region. These new signals are assigned to a non-allylic C_3H_4 residue, which is likely formed by a rearrangement of the allylic C_3H_4 species and also a further decomposition of the ring-opening species. This conclusion is supported by a quantitatively progressing CO formation. Further evidence for this reaction is provided by gas phase studies, where propargyl radicals were found in the decomposition process of furan.[186] This species is present at temperatures up to around 440 K. Above this temperature, also no CO is found in both core level regions. Above 390 K, the spectra in the C 1s region are composed of three peaks at 283.5, 283.9 and 284.3 eV, which are the result of a further decomposition of the C_3H_4 species. Here, we propose the formation of a C_3H_2 compound, as the same C 1s signal pattern is found in the spectra of THF (see below in Chapter 7.2.2.) and since the corresponding TPD data (see Figure 48) indicates the loss of one further hydrogen atom.

In summary, furan is stable up to 210 K on platinum and above this temperature a ring-opening product is formed. Further heating leads to a decomposition of the ring-opening species into C_3H_4 under the formation of CO. At even higher temperatures, a dehydrogenation of C_3H_4 into C_3H_2 is observed.

7.2.2. Tetrahydrofuran

THF represents the hydrogen- and energy-rich species in the proposed LOHC cycle THF/furan. As for furan, individual high-resolution XPS experiments in the carbon and oxygen region have been performed for the adsorption and reaction. In addition to that, TPD data provides further insights in the dehydrogenation mechanism.

Representative spectra from the O 1s (0.21 L, 0.26 ML C) and C 1s (0.05 L, 0.16 ML C) region from the adsorption and heating experiment (TPXPS) are presented in Figure 46. During the adsorption of THF on clean Pt(111) at 130 K, one distinct peak at 532.3 eV grows almost linearly in the O 1s region. In comparison to the O 1s signal of furan, it is shifted by 0.1 eV to higher binding energy. In the C 1s region, the exposure to THF shows two signals at 284.2 and 285.5 eV. As in the furan experiment, the peak at low binding energy is assigned to the two carbon atoms distant to the oxygen atom, the signal at higher binding energy corresponds to the two carbon atoms in close vicinity to the oxygen atoms. At the beginning of the heating experiment, the O 1s signal intensity decreases by around 50% at 160 K, which is assigned to molecular desorption of THF. The same behavior is observed in the C 1s region, where approximately half of the signal intensity is lost. The introduction of three new signal at 284.2, 284.6 and 285.3 eV is necessary to fit the spectra in the carbon region. As the overall signal shape differs from that of the furan signals, a partial dehydrogenation to H_x-furan is proposed. Simultaneously, a small shift to 532.2 eV is seen in the oxygen region, which is attributed to a partial dehydrogenation of THF and the formation of a H_x-furan species. The TPD experiment shown in Figure 48 cannot provide insights in the degree of dehydrogenation, as hydrogen desorption from Pt(111) starts only at around 300 K. This partially dehydrogenated species can be found in both regions up to around 240 K. At 210 K, a new O 1s signal at 533.1 eV indicates a cleavage of a C-O bond and the formation of a partially dehydrogenated ring-opening product. Please note that this reaction takes place at the same temperature as in the furan experiment. However, the corresponding XPS signal for the ring-opening product in the THF experiment is found at a significantly higher binding energy (533.1 vs 530.8 eV). This behavior is possibly attributed to a different adsorption geometry. It is known that furan adsorbs flat on the surface, whereas an upright standing geometry is proposed for THF.[182] The decrease in O 1s signal intensity during the ring opening reaction might be attributed to a photoelectron diffraction effect.

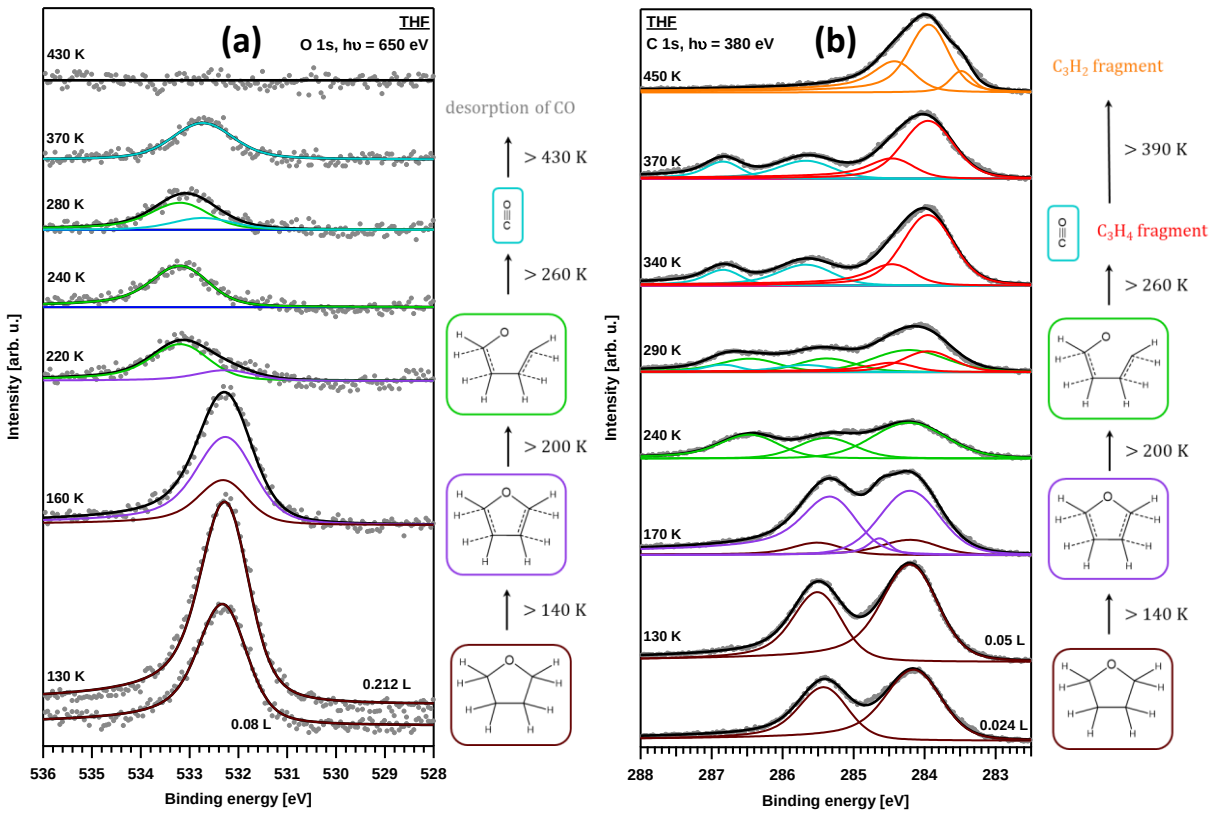

Figure 46: Selected O 1s (a) and C 1s (b) XP spectra for THF on Pt(111).

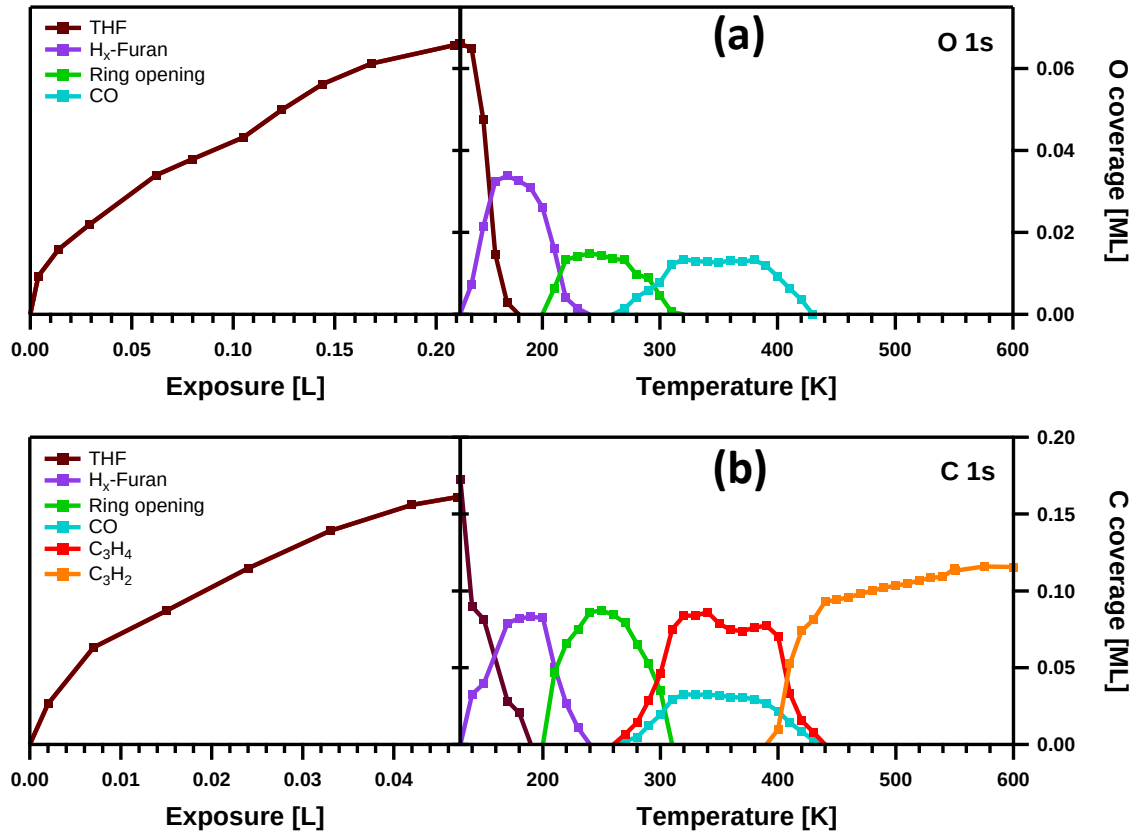

Figure 47: *Quantitative analysis of the O 1s (a) and C 1s (b) experiments for THF on Pt(111).*

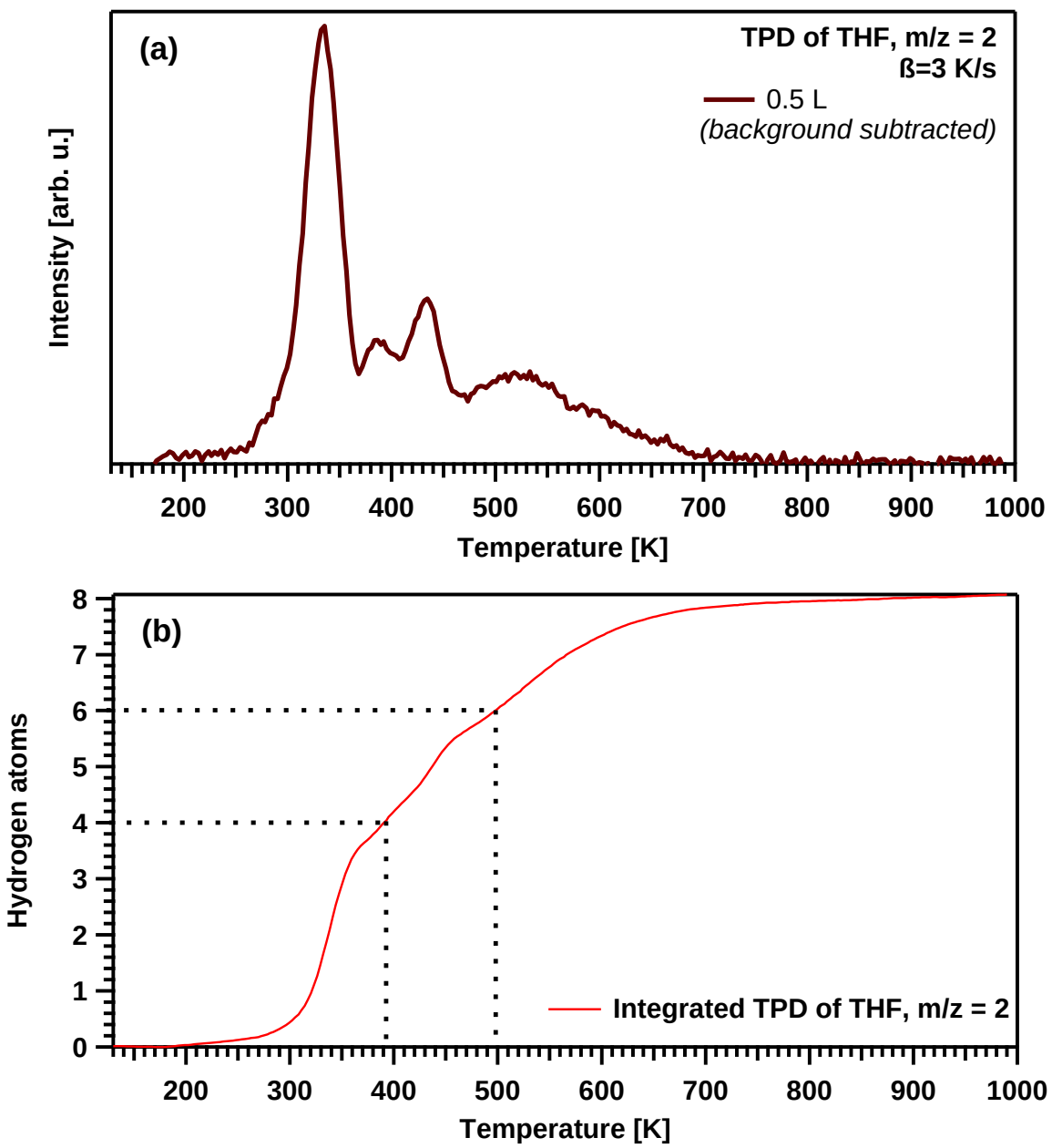

Figure 48: (a) TPD experiment (m/z = 2, H_2) of THF on Pt(111). (b) Integrated TPD of THF.

The partially dehydrogenated ring opening compound is described by three signals at 284.2, 285.4 and 286.4 eV in the carbon region. The signal pattern differs slightly from the ring-opening product in the furan experiment, which is attributed to additional hydrogen atoms and a different adsorption geometry. This ring-opening product vanishes at around 310 K in both core level regions. Above 260 K, the ring-opening species starts to react under the formation of CO. In the oxygen region, a signal at 532.7 eV grows and is assigned to a CO on-top species. CO is also found in the carbon region at 285.6 (bridge) and 286.8 eV (on-top). However, compared to the literature value, the signal for the bridge species is shifted by 0.5 eV to lower binding energy and has a broader shape.[184] This may be induced

by the coadsorption of the ring-opening product in bridge position. DFT calculations have shown that the dehydrogenation of propane to propylene takes place in a bridge position.[187] It is also known that n-butane, which has four carbon atoms like the ring-opening product, adsorbs with its center over bridge sites.[188] During the formation of CO, a C_3H_4 residue is described by signals at 283.9 and 284.4 eV in the carbon region. This is in line with the TPD experiment shown in Figure 48a. The integrated area of the m/z =2 spectrum (Figure 48b) shows that four of overall eight hydrogen atoms have desorbed from the surface at 390 K. This C_3H_4 compound is present on the surface up to 430 K in the carbon region. Also at 440 K, the CO signals vanish in the O 1s and the C 1s region due to desorption.

At temperatures above 390 K, the formation of a C_3H_2 fragment is proposed with signals at 283.5, 283.9 and 284.4 eV. The molecular formula of this reaction product is derived from the TPD experiment. The integrated area of the m/z = 2 spectrum shows, that six hydrogen atoms have desorbed at 500 K.

Summarizing, THF undergoes a partial dehydrogenation to a H_x-furan species. Subsequently, a ring opening product is formed like in the furan experiment and further heating leads to the formation of CO and the decomposition products C_3H_4 and C_3H_2. However, no allylic species is found in contrast to the furan experiment.

7.2.3. Benzofuran

Benzofuran is the energy- and hydrogen-lean species in the proposed LOHC cycle of dihydrobenzofuran/benzofuran. Like for the O-heterocycles with five-membered rings, an understanding of the thermal stability of the dehydrogenated species is crucial. Furthermore, fingerprint spectra of the hydrogen-lean compound facilitate the interpretation of spectra of the hydrogen-rich species.

In Figure 49, representative spectra from the O 1s (0.30 L, 0.32 ML C) and C 1s (0.31 L, 0.32 ML C) region from the adsorption and heating experiment (TPXPS) of benzofuran are shown.

The adsorption of benzofuran at 130 K on platinum shows a linear growth (see Figure 50) of one distinct signal in the O 1s region at 532.5 eV. Compared to the also hydrogen-lean

furan, the binding energy is shifted by 0.3 eV to higher binding energy. In the carbon region a linear rise of three signals at 284.2, 285.1 and 285.5 eV is observed. A clear assignment of these peaks to specific carbon atoms is difficult.

Right after the adsorption of benzofuran in each core level experiment, heating experiments were performed. In the oxygen region, we see a 20% decrease in peak intensity between 150 and 180 K, which is assigned to the desorption of the contaminant water, which contributed to the signal. This is in line with the spectra in the carbon region, where no decrease in carbon surface coverage is detected below 200 K. Therefore, a molecular desorption of benzofuran is excluded at this temperature. When the temperature is increased to 210 K, a new signal starts to rise at 530.8 eV in the oxygen core level. As this peak has the same binding energy as the ring-opening species in the furan experiment, we propose a cleavage of the C-O bond between the tertiary carbon atom and oxygen.

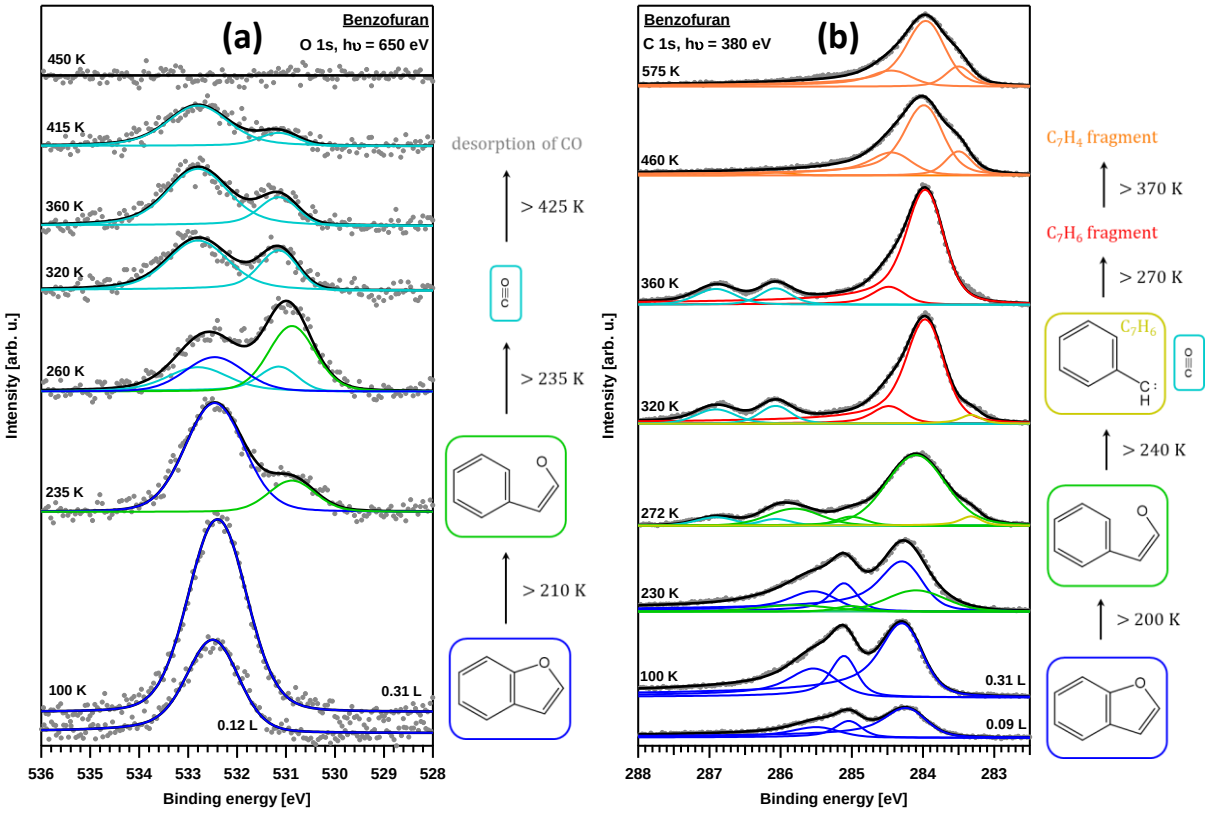

Figure 49: Selected O 1s (a) and C 1s (b) XP spectra for benzofuran on Pt(111).

A cleavage of the bond between the secondary carbon atom and oxygen is improbable, as CO is formed in the further reaction pathway (see Figure 49). As the phenyl ring is considered as relatively stable, its decomposition for the formation of CO is highly

unlikely. The surface coverage of the ring-opening product reaches its maximum at 275 K and vanishes at 305 K. Three signals in the C 1s region at 284.1, 285.0 and 285.8 eV are assigned to this ring-opening species. At 240 K, we monitored the rise of CO signals in the oxygen region at 531.1 (bridge) and 532.8 eV (on-top). The formation of CO is also visible in the carbon spectra, as two characteristic peaks grow at 286.1 (bridge) and 286.9 eV (on-top).

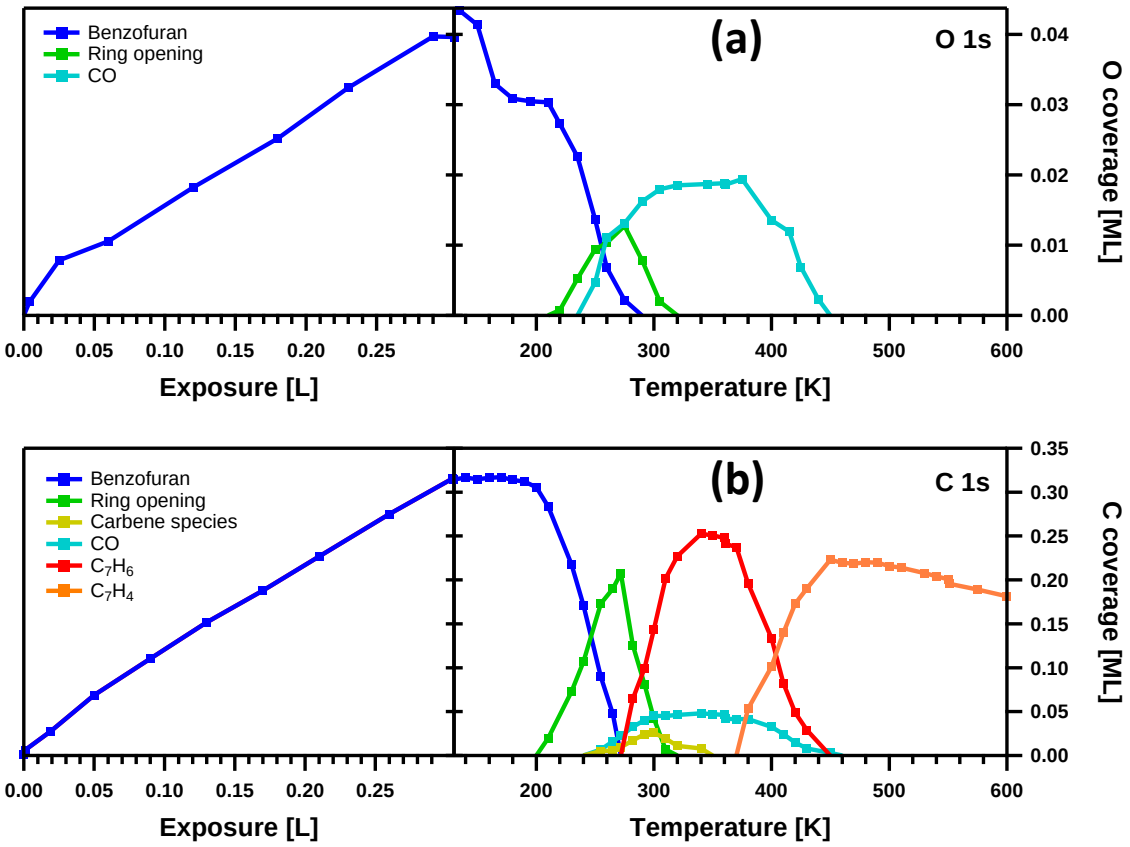

Figure 50: *Quantitative analysis of the O 1s (a) and C 1s (b) experiments for benzofuran on Pt(111).*

With the onset of CO formation, a small shoulder signal rises at 283.3 eV, which is present up to 340 K. We assign this to the formation of a carbene-like intermediate with an electron loan pair at the benzyl carbon or an allylic compound, as seen in the furan experiment. The formation of a benzyl species is also excluded, as its signal shape was determined in previous studies and does not match.[175] Moreover, a benzyl species would be stable up to 475 K on a platinum surface.[175] Heating above 270 K results in a more narrow signal shape in the carbon region with new peaks at 283.9 and 284.5 eV with a signal height ratio of 6:1. As CO is still produced at this temperature, we propose a remaining C_7H_6 fragment, which gains its highest surface coverage together with CO at

around 350 K. This C_7H_6 fragment has the same chemical formula as the carbene intermediate (electron loan pair at primary carbon atom), but is possibly bound with the primary carbon atom to the platinum surface. The spectral shape resembles that of toluene[175] and benzene[189]. Thus, an aromatic character of this fragment is likely. This compound, together with CO, vanishes at 450 K in the carbon region. The next reaction product in the carbon region is found above 370 K is a C_7H_4 fragment with signals at 283.5, 284.9 and 284.4 eV. Evidence for this species is provided in the next section. In the heating experiment of dihydrobenzofuran, similar signals are found and assigned with supporting TPD data (see Figure 53) to a C_7H_4 fragment. Above 450 K, only this compound is identified on the platinum surface.

In conclusion, the reaction mechanism of benzofuran resembles that of furan in some points. In a first reaction step, a ring-opening product is formed. At higher temperatures CO is cleaved from the ring-opening compound. In contrast to furan, a short-living carbene-like species is identified. This different reaction behavior is caused by the additional benzene ring in the benzofuran molecule. Further heating results in a C_7H_6 and a C_7H_4 decomposition product.

7.2.4. Dihydrobenzofuran

Dihydrobenzofuran is a hydrogen- and energy-rich species in the proposed LOHC cycle dihydrobenzofuran/benzofuran. However, this molecule is not fully hydrogenated and has an aromatic six-membered carbon ring. Similar to the previous experiments, XP spectra for the carbon and oxygen region are provided. Additional TPD data allows for a comprehensive analysis of the dehydrogenation pathway.

Selected XP spectra from the O 1s (0.35 L, 0.40 ML C) and C 1s (0.05 L, 0.21 ML C) region from the adsorption and heating experiment (TPXPS) are shown in Figure 51.

Please note that before the adsorption (O 1s: 105 K, C 1s: 100 K) of dihydrobenzofuran, an impurity causes a small signal in the O 1s region at 531.8 eV. In the fitting process of all shown spectra, the signal height was held constant. Exposure to dihydrobenzofuran leads to a growing signal at 532.4 eV in the oxygen region. Compared to the other hydrogen-rich compound THF, the signal is shifted by 0.2 eV to higher binding energies. An arrow in the quantitative analysis (see Figure 52) marks the time the dosing valve was

closed. However, a slow increase in surface coverage is still detected due to post adsorption, i.e., a low pumping speed of the adsorbate.

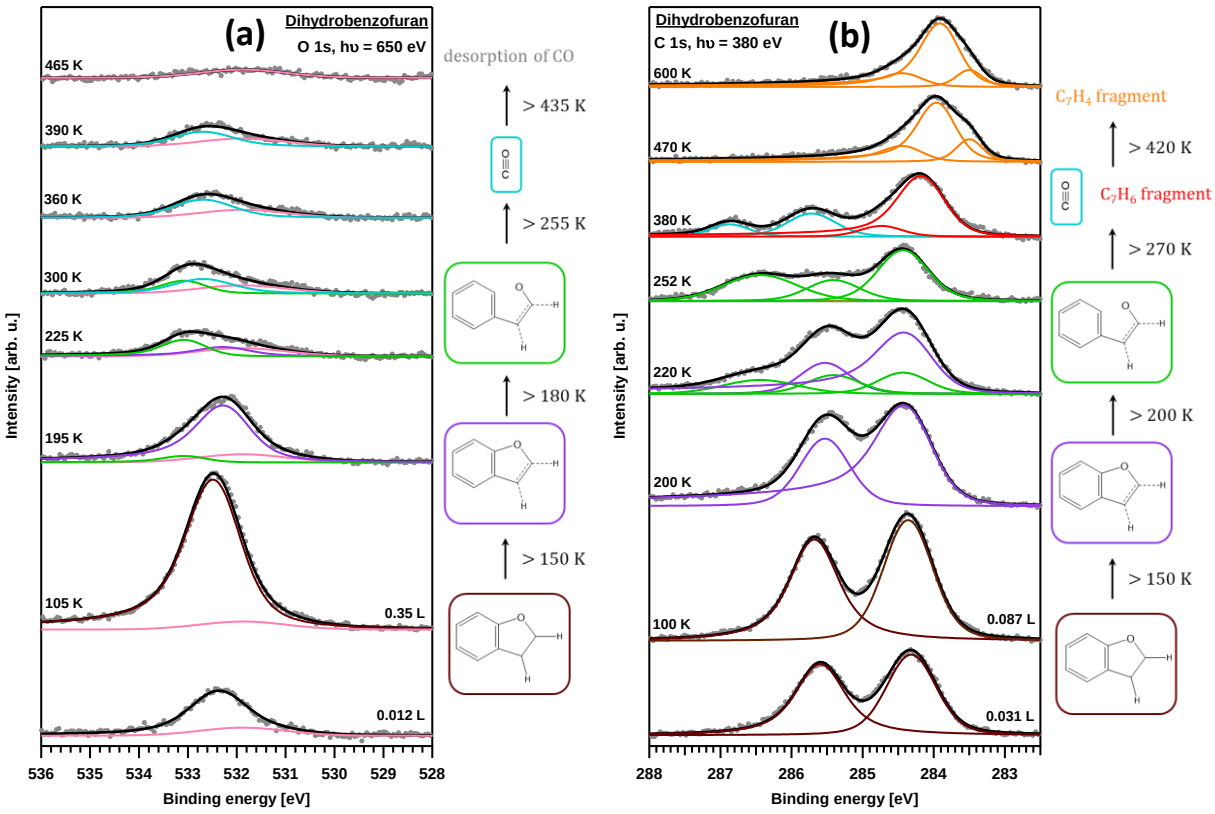

Figure 51: Selected O 1s (a) and C 1s (b) XP spectra for dihydrobenzofuran on Pt(111).

In the carbon region, two distinct signals at 284.4 and 285.7 eV are detected. As in the O 1s region, post adsorption of the substance is observed.

At the beginning of the heating experiment, we see a significant decrease in oxygen surface coverage at 150 K. This is caused by the desorption of water, which cannot be resolved spectroscopically due to an overlapping peak with the dihydrobenzofuran signal. As no decrease in carbon coverage is detected in the C 1s region at this temperature, molecular desorption is excluded. Moreover, a first reaction step occurs at 150 K, which is indicated by a shift of the oxygen signal by 0.2 eV to lower binding energy. At the same time, both signals in the carbon region shift to slightly lower binding energy. As a difference between the carbon spectra of this species and pristine benzofuran is observed, we expect a partial dehydrogenation of the five-membered ring at this temperature. This species, which is found between 150 and 250 K, is named H_1-benzofuran. However, it is not clear if the hydrogen atom is cleaved in alpha- or beta-position to the oxygen atom. Above 180 K, a new contribution in the O 1s region is monitored at 533.0 eV and assigned

to a ring-opening species. The binding energy is similar to the ring-opening compound in the THF experiment, but shifted by 2 eV to higher binding energy in relation to benzofuran. This 2 eV difference may be caused by a different degree of hydrogenation and different adsorption geometries on the surface. As in the benzofuran experiment, the ring-opening is expected to happen between the tertiary carbon atom and the oxygen atom due to the stability of the phenyl ring. The ring-opening compound vanishes at temperatures above 350 K in both regions.

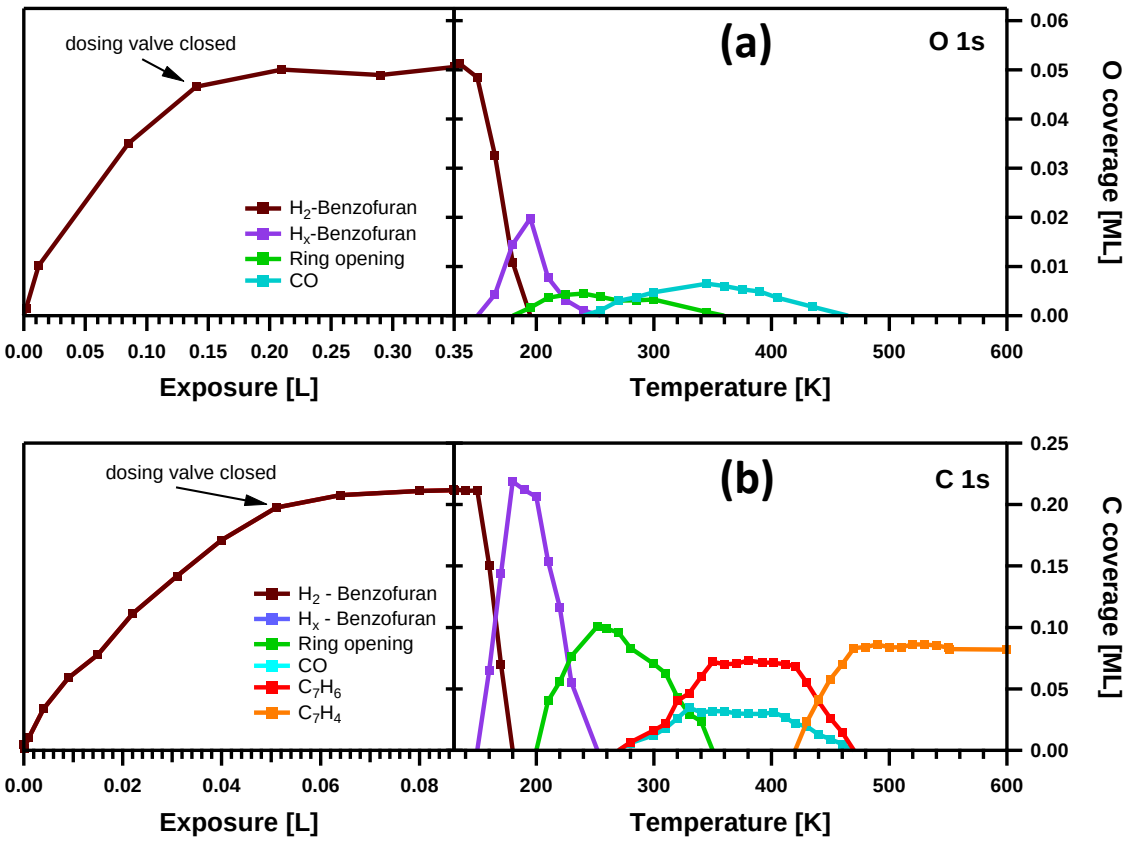

Figure 52: Quantitative analysis of the O 1s (a) and C 1s (b) experiments for dihydrobenzofuran on Pt(111).

Above 200 K, a decrease of more than 50% of the H_1-benzofuran coverage in both regions is observed and attributed to molecular desorption of H_1-benzofuran. Above 255 K, a signal at 532.7 eV emerges and represents the formation of an on-top CO species. As for the hydrogen-rich compound THF, no bridge species is detected in the oxygen region. In the carbon region, both, the bridge and on-top CO species are monitored with signals at 285.7 and 286.9 eV above 270 K. Similar to the THF experiment, the bridge species is shifted to lower binding energy and shows a higher width compared to the literature value.[184] This might be induced by coadsorption effects of CO with the dehydrogenated

species or hydrogen. With the onset of CO formation, a new reaction product in the carbon region is detected with peaks at 284.1 and 284.7 eV. As CO is cleaved from H_1-benzofuran at the same time, we expect the formation of a C_7H_x species. Integration of the first sharp signal in the TPD spectrum (see Figure 53) at around 375 K accounts to two hydrogen atoms. (Please note, that the small signal below 300 K in the TPD spectrum is assigned to a desorption from the sample holder.) With this information, we specify this compound to a C_7H_6 fragment. However, the XPS signals are shifted slightly to higher binding energies (+0.2 eV) compared to the C_7H_6 species in the benzofuran experiment. CO desorbs at 470 K and at the same temperature the C_7H_6 species vanishes due to a further reaction.

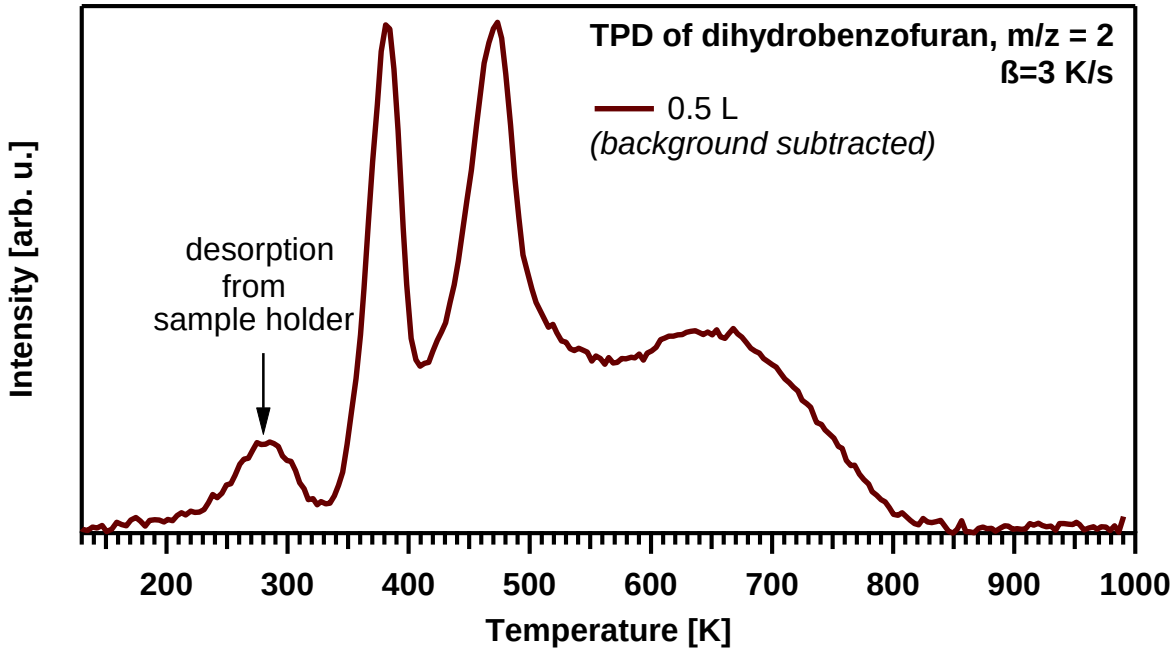

Figure 53: TPD experiment (m/z = 2, H_2) of dihydrobenzofuran on Pt(111).

Above 420 K, the same three signals as in the benzofuran experiment at 283.5, 283.9 and 284.4 eV are detected in the carbon region. Integration of the TPD spectrum to 500 K shows that in total four hydrogen atoms are cleaved from the pristine dihydrobenzofuran molecule. Therefore, the formation of a fragment with the molecular formula C_7H_4 is proposed.

In summary, dihydrobenzofuran is dehydrogenated partially to a H_1-benzofuran species. This compound shows partial molecular desorption and the residues undergo a ring-

opening reaction. Further heating leads to the cleavage of CO and the formation of a C_7H_6 species. At even higher temperatures, this fragment is dehydrogenated to a C_7H_4 species.

7.3. Conclusions

We investigated the surface reaction of the two LOHC pairs THF/Furan and dihydrobenzofuran/benzofuran on Pt(111) with high-resolution TPXPS and TPD. The hydrogen-lean furan shows a ring-opening reaction above 210 K. At around 240 K, CO is cleaved, and an allylic intermediate is formed. Above 270 K, a reorganization to a C_3H_4 fragment is found, which is dehydrogenated to C_3H_2 above 390 K. For the hydrogen-rich THF, we observed a partial dehydrogenation into H_x-Furan above 140 K. At higher temperatures, a similar reaction pathway as for furan, but with absence of the allylic species, was monitored. Benzofuran shows a ring-opening of the five-membered ring above 205 K and a dissociation of CO above 240 K. Instead of an allylic species, the formation of a carbene (C_7H_6) as intermediate is proposed, which reacts to a C_7H_6 compound with the same chemical formula but different adsorption geometry above 270 K. This fragment shows further dehydrogenation to a C_7H_4 species above 370 K. The hydrogen-rich dihydrobenzofuran is dehydrogenated to a H_1-benzofuran intermediate above 150 K. At higher temperatures, we monitored the same reaction pathway as for benzofuran. Summarizing, a complete dehydrogenation of the hydrogen-rich compounds into the hydrogen-lean compounds was not observed and the early onset of ring-opening reactions is a challenge for the use in a reversible LOHC systems. The splitting of the C-O bond has to be avoided under real catalytic conditions to retain reversibility in a LOHC application.

8. Conclusion and comparison of different LOHC systems

In this chapter, the investigated LOHC compounds are compared with each other. In particular, the influence of the structural differences in the LOHC molecules on their reaction behavior is discussed.

Influence of ring-size: Five-membered rings vs. six-membered rings

For a better understanding of how the ring size affects a LOHC system, studies of five-membered and six-membered N-heterocyclic ring systems were conducted. These LOHC compounds are compared in terms of their thermal stability. For a functioning LOHC cycle, it is essential that the LOHC molecules do not decompose and maintain an intact organic framework. In this regard, the hydrogen-lean LOHC molecule pyrrole shows a relatively high thermal stability on a nickel surface with a decomposition temperature slightly above 450 K (see Figure 54a), whereas a decomposition temperature of 380 K is seen for the six-membered ring pyridine. In addition, the decomposition temperatures of the hydrogen-rich LOHC molecules can also be compared. Please note that for the hydrogen-rich molecules the decomposition temperature was defined so that more than 10% of the molecules are decomposed (e.g., ring-opening), as the dehydrogenation would still be economical even if a very small fraction of the hydrogen-rich LOHC molecules decompose. The hydrogen-rich pyrrolidine decomposes at 410 K, whereas a decomposition of piperidine is witnessed at 350 K. Accordingly, five-membered ring systems appear to be thermally more stable than six-membered ones. This applies to both the hydrogen-lean and hydrogen-rich LOHC compounds.

LOHC compounds can also be compared by the temperature, at which the dehydrogenation starts. In Figure 54b, these temperatures for hydrogen-rich N-heterocyclic LOHC molecules on Ni(111) are shown. The highest dehydrogenation temperature was found for piperidine at 290 K, closely followed by pyrrolidine at 275 K. The six-membered ring piperidine is probably less suitable than the five-membered ring pyrrole for the use in a LOHC cycle, due to a higher dehydrogenation temperature and also a lower thermal stability of the hydrogen-lean species. In this regard, the LOHC system pyrrole/pyrrolidine should be favored over the system pyridine/piperidine.

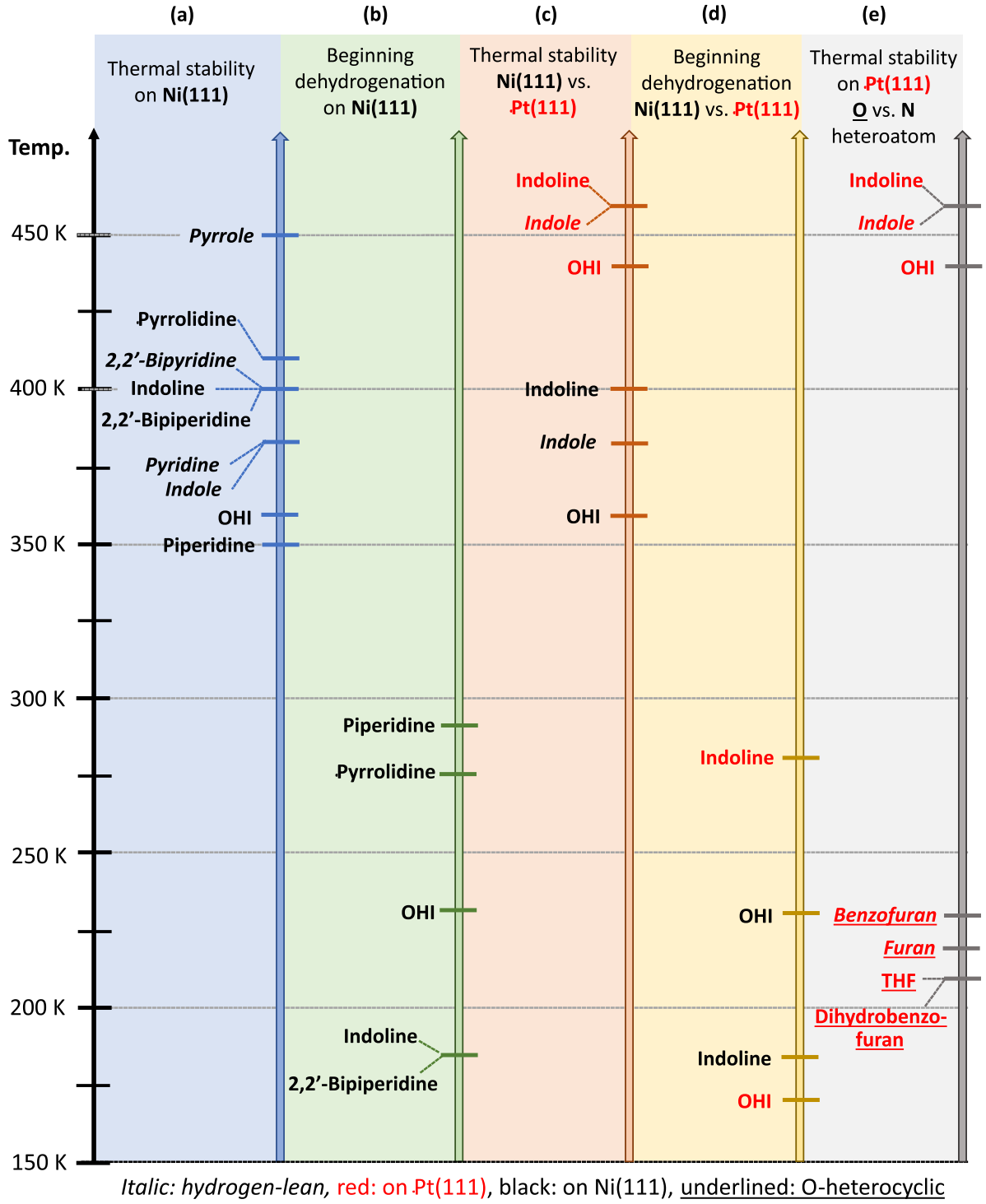

Figure 54: Comparison between investigated LOHC systems. (a) Thermal stability of N-heterocyclic LOHCs on Ni(111), (b) beginning dehydrogenation of hydrogen-rich N-heterocyclic LOHCs on Ni(111), (c) thermal stability of indole, indoline and octahydroindole on Ni(111) and Pt(111), (d) beginning dehydrogenation of octahydroindole and indoline on Ni(111) and Pt(111), (e) thermal stability of structurally very similar O- and N-heterocyclic compounds on Pt(111).

Influence of heteroatoms: Nitrogen vs. oxygen

The functionalization of LOHC molecules with different heteroatoms like nitrogen or oxygen has also an impact on their reaction behavior. In this respect, the O-heterocyclic LOHC system benzofuran/dihydrobenzofuran is compared with the N-heterocyclic LOHC system indole/indoline on Pt(111).[151] Both, indole and indoline have a high thermal stability on Pt(111) and decompose above 460 K, see Figure 54e. Benzofuran and dihydrobenzofuran on the other hand start to decompose at relatively low temperatures, as ring-opening reactions occur. The ring-opening was observed at 230 K for benzofuran and at 210 K for dihydrobenzofuran. Moreover, the cleavage of the catalyst poison CO in a subsequent reaction step is problematic for the use as LOHC compounds. A similar reaction behavior was also seen for the compounds furan and THF without a π-extension. None of the investigated O-heterocyclic and hydrogen-rich LOHC are completely dehydrogenated before the beginning ring-opening reaction. In contrast to that, a dehydrogenation of octahydroindole and indoline was possible on the same catalyst.

Influence of catalyst: Nickel vs. platinum

The influence of the catalyst material on the reaction behavior of LOHC systems was also examined, as the LOHC system indole/indoline/octahydroindole was investigated on Ni(111) in this thesis and on Pt(111) in recent studies.

In Figure 54c, the thermal stabilities of indole, indoline and octahydroindole on Ni(111) are compared to their thermal stabilities on Pt(111). Indole begins to decompose at 460 K on Pt(111) and at already 380 K on Ni(111). The same trend is witnessed for indoline and octahydroindole. Indoline decomposes at 460 K on Pt(111) and at 400 K on Ni(111), while octahydroindole starts to decompose at 440 K on Pt(111) and at already 360 K on Ni(111). As the decomposition temperatures for all three compounds are shifted to lower temperatures on a nickel surface, this may indicate a stronger activation of the C-N bond in comparison with a platinum-catalyzed reaction. This would also explain, why small amounts of ring-opening products through cleavage of the C-N bond were found during the dehydrogenation of the hydrogen-rich octahydroindole on Ni(111). In contrast to that, no ring-opening products have been found during the dehydrogenation of octahydroindole to indolide on Pt(111). This finding indicates, that ring-opening reactions at C-N bonds are more likely to take place on nickel catalysts than on platinum

catalysts. Such undesired ring-opening reactions could lead to poisoning of the catalyst with side products and inhibit further dehydrogenation reactions of LOHCs.

The temperatures of a beginning dehydrogenation of the hydrogen-rich octahydroindole and the dehydrogenation intermediate indoline are compared in Figure 54d for a nickel and a platinum surface. The dehydrogenation of indoline starts at 280 K on a Pt(111), while the onset of the dehydrogenation was found at 180 K on Ni(111). On both catalysts, the five-membered pyrrolidine ring of indoline is dehydrogenated in the first reaction step. This reaction is shifted to lower temperatures when nickel is used as a catalyst. However, the dehydrogenation temperatures of octahydroindole show a different trend. Here, a dehydrogenation of octahydroindole is witnessed at 230 K on Ni(111), while a dehydrogenation was observed at already 170 K on Pt(111). The use of a platinum catalyst is therefore more favorable for the dehydrogenation of the hydrogen-rich species octahydroindole, while the use of nickel is more favorable for the dehydrogenation of the dehydrogenation intermediate indoline. Accordingly, a platinum-nickel alloy could have a particularly beneficial effect on the dehydrogenation temperature, leading to a lower dehydrogenation temperature of the LOHC system octahydroindole/indoline/indole. This finding is of interest for future studies on N-heterocyclic LOHC systems under real-catalytic conditions. The reaction pathways of indole, indoline and octahydroindole with all reaction temperatures on Ni(111) and Pt(111) are also compared in Figures A 1-3 for a better overview.

Influence of π-extension

The investigated LOHC systems also allow one to determine the effect of a π-extension on the reaction behavior. The hydrogen-lean LOHC molecule pyrrole decomposes at 450 K on Ni(111) (see Figure 54a). At 380 K, we observed the beginning decomposition of indole, which consists of a pyrrole ring connected with a benzene ring over one C-C bond and one C-N bond. Interestingly, a significantly lower thermal stability was seen for indole in comparison with pyrrole. This finding suggests a lower thermal stability of hydrogen-lean LOHC compounds through π-extension by one C-C and one C-N bond. The hydrogen-rich pyrrolidine (410 K) also shows a higher thermal stability than the π-extended molecule indoline (400 K).

The π-extension, however, has a beneficial effect on the dehydrogenation temperature. Indoline shows a first dehydrogenation step at 180 K and is therefore more favorable than

pyrrolidine, which is dehydrogenated above 275 K (see Figure 54b). This finding suggests, that a π-extension of N-heterocyclic molecules has a lowering effect on the dehydrogenation temperature (indoline<pyrrolidine).

The π-extension of O-heterocyclic LOHC systems (THF vs. dihydrobenzofuran) did not show any significant impact on the reaction behavior. Both, molecules without π-extension and molecules with π-extension show a ring-opening reaction at relatively low temperatures before complete dehydrogenation. As a result, both types of molecules are rather unsuitable for the use in LOHC systems.

Linking heterocycles via a C-C bond

In this work, both pyridine and bipyridine were studied. This allows a statement about the influence of a linkage of heterocycles via a C-C bond in α-position. The LOHC compound 2,2'-bipyridine, which consists of two connected pyridine rings, decomposes at 400 K (see Figure 54a). 2,2'-Bipyridine shows a higher thermal stability than pyridine itself, which forms small amounts of decomposition products at already 380 K. For the hydrogen-rich compounds, the same trend was observed. While 2,2'-bipiperidine is stable to 400 K, piperidine decomposes at already 350 K.

Apparently, the fusion of two N-heterocyclic rings via one C-C bond in α-position to nitrogen improves their thermal stability.

Moreover, the dehydrogenation temperatures of 2,2'-bipiperidine and piperidine can be compared. At 180 K, the dehydrogenation of 2,2'-bipiperidine was monitored (see Figure 54b). Although the molecule is structurally very similar to piperidine, the dehydrogenation temperature of 2,2'-bipiperidine is shifted 110 K to lower temperatures. 2,2'-Bipiperidine seems to be more suitable as LOHC molecule than piperidine due to a significantly lower dehydrogenation temperature and also the fact, that its hydrogen-lean counterpart 2,2'-bipyridine has a slightly higher thermal stability than pyridine. For future research, the binding of two pyridine rings via a C-C bond in β- or γ-position to nitrogen and its influence on the thermal stability would also be of interest.

Further considerations

In a functioning LOHC system, the hydrogen-lean molecule has to desorb from the catalyst. The desorption of the hydrogen-lean compounds was not observed in the presented experiments due to the low pressures under UHV conditions and the lack of competition between molecules for adsorption sites. Therefore, the desorption behavior of the hydrogen-lean compounds has to be investigated separately under real catalytic conditions at higher pressures. The impact of the ring size, the catalyst, the heteroatoms, π-extension and connection of rings via a C-C bond also plays a significant role in the desorption behavior of LOHC compounds.

9. Summary

Liquid organic hydrogen carriers (LOHCs) are compounds, which are suitable for chemical hydrogen storage. This energy storage solution is particularly interesting in view of the expansion of green energy, as surplus energy from renewable energy sources can be used to produce “green” hydrogen. In a LOHC cycle, a hydrogen- and energy-lean LOHC molecule is catalytically hydrogenated, forming a hydrogen- and energy-rich LOHC species. When energy is needed, the stored hydrogen is catalytically released. In previous studies, N-heterocyclic compounds such as N-ethylcarbazole/H_{12}-N-ethylcarbazole have been identified as promising LOHC candidates. These studies are continued in this work with a focus on the influence of the catalyst material, the effect of a π-extension to the molecules, the incorporated heteroatom and the viability of five- and six-membered rings.

The dehydrogenation behavior of the liquid organic hydrogen carrier candidates was investigated under model catalytic conditions. After physical vapor deposition (PVD) of the LOHC compounds on the dehydrogenation catalysts Ni(111) and Pt(111), the reactions were monitored. In order to gain detailed insights into the reaction pathways of the presented LOHCs, the surface science techniques high-resolution X-ray photoelectron spectroscopy, temperature programmed desorption and near-edge X-ray absorption fine structure were used under ultra-high vacuum conditions. The in situ XPS experiments allowed for identifying reaction products and intermediates on the catalytic surfaces during the dehydrogenation. Temperature programmed desorption was used as a complementary method to monitor the desorption of hydrogen ($m/z = 2$) from the reaction.

In Chapter 4, the LOHC system indole/indoline/octahydroindole on Ni(111) is investigated. Indole represents the hydrogen-lean LOHC species, whereas octahydroindole is the fully hydrogenated counterpart. In addition, the partially hydrogenated compound indoline, which is hydrogenated at the five-membered ring, was also included in the investigations. During the heating experiment , the dehydrogenation of indole at the nitrogen atom and the formation of an indolide surface species was observed at 130 K. No further reaction steps were found for the indolide species before its decomposition at around 400 K. The partially hydrogenated LOHC molecule indoline shows a first reaction step at 180 K, when dehydrogenations at the carbon atoms of the pyrrole ring and at the nitrogen atom occur simultaneously, which leads to the formation

of indolide. The decomposition of indolide was witnessed at around 380 K. The more complex reaction pathway of octahydroindole starts with a reaction at 230 K, when several different dehydrogenation intermediates are formed. Further heating to above 340 K induces the reaction of the dehydrogenation intermediates into indolide, which was already found in the indole and indoline experiments. The indolide species is, however, accompanied by a ring-opening product at the nitrogen atom and a partially dehydrogenated octahydroindole. Under real catalytic conditions, the formation of ring-opening products has to be avoided, as this would lead to a loss of reusable LOHC molecules. Furthermore, fragments of LOHC molecules could poison the catalyst and hinder further dehydrogenation. The reaction pathways of indoline and octahydroindole on Ni(111) differ from those on Pt(111). The use of a nickel catalyst for the dehydrogenation of indoline seems more favorable than the use of platinum, as the dehydrogenation begins at lower temperatures (Ni(111): 180 K vs. Pt(111): 280 K). For the dehydrogenation of octahydroindole, a platinum catalyst should preferably be used, since on the noble metal the dehydrogenation takes place at lower temperatures (Pt(111): 280 K vs. Ni(111): 340 K) without the formation of ring-opening products.

The next investigated LOHC system, discussed in Chapter 5, is 2,2'-bipyridyl/2,2'-bipiperidine on Ni(111). For the hydrogen-lean LOHC species 2,2'-bipyridyl, weakly adsorbed multilayers on top of a first chemisorbed layer were found despite sub-monolayer coverage experiments. The weakly physisorbed molecules move to vacancies on the nickel surface at around 215 K. The flat-lying 2,2'-bipyridyl molecules are dehydrogenated in α-position above 370 K. In this reaction step, an α-2,2'-bipyridyl species with a slightly tilted adsorption geometry is produced. No further reaction steps of α-2,2'-bipyridyl were identified before decomposition at 400 K. The hydrogen-rich counterpart 2,2'-bipiperidine undergoes a partial dehydrogenation above 180 K. Subsequently, the deprotonation at both nitrogen atoms was observed at 250 K Above 320 K, a further reaction step leading to the formation of an α-2,2'-bipyridyl compound is found, which was already identified in the reaction pathway of the hydrogen-lean 2,2'-bipyridyl. The desorption maximum of hydrogen was found at around 360 K in TPD experiments. Besides the dehydrogenated species α-2,2'-bipyridyl, we also identified small amounts of a compound that is only partially dehydrogenated at the carbon atoms. The organic framework of the dehydrogenation products decomposed into fragments above 400 K.

Chapter 6 describes the dehydrogenation behavior of the six-membered ring systems pyridine/piperidine and the five-membered ring systems pyrrole/pyrrolidine. The hydrogen-lean compound pyridine shows a dehydrogenation and the formation of an α-pyridyl species above 260 K. This compound is further dehydrogenated above 290 K in the heating experiment to form an α,α-pyridyl. The cleavage of a hydrogen atom in γ-position to nitrogen was observed in a consecutive dehydrogenation step above 380 K, followed by a decomposition into fragments starting at 410 K. The hydrogen-rich LOHC counterpart piperidine shows a simultaneous dehydrogenation to pyridine and α-pyridyl above 290 K. However, also ring opening products were found above this temperature, which accompanied the desired reaction products and amounted to 12% of the total surface coverage. Heating to above 380 K induces the formation of a different ring-opening product, which is likely caused by a dissociation of a C-C bond. The complete fragmentation was witnessed above 490 K in TPXPS.

For pyrrole and pyrrolidine similar reaction products were found. Pyrrole is dehydrogenated at the nitrogen atom at relatively low temperatures. Small amounts of the reaction product were already observed upon adsorption at 130 K. In a following dehydrogenation step, which starts at 270 K, one carbon atom in α-position to the nitrogen atom is cleaved and an α-pyrrolyl compound is formed. In a following dehydrogenation step above 400 K, an α,α-pyrrolyl is formed, as another hydrogen atom is cleaved in α-position to the nitrogen atom. The fragmentation of the five-membered ring is seen above 450 K. The hydrogen-rich LOHC molecule pyrrolidine reacts directly to α-pyrrolyl above 270 K without further dehydrogenation intermediates, as the dehydrogenation at the nitrogen atom and the carbon atoms occurs at the same time. It is remarkable that the dehydrogenation of the hydrogen-rich compound takes place without the formation of ring-opening products, which were observed in the dehydrogenation of the six-membered ring piperidine. Above 350 K, the same α,α-pyrrolyl species is detected, which was already identified in the reaction pathway of pyrrole. No more reaction products were detected before the decomposition above 470 K. The comparison of the hydrogen-rich compounds piperidine and pyrrolidine shows that pyrrolidine is more favorable in LOHC systems on nickel catalysts.

The O-heterocyclic LOHC systems furan/THF and benzofuran/dihydrobenzofuran on Pt(111) have been discussed in Chapter 7. The hydrogen-lean molecule furan undergoes an undesired ring-opening at already 210 K. An allylic intermediate was observed upon

further heating above 240 K, as CO was cleaved from the ring-opening product. The allylic species rearranged on the surface to form C_3H_4 at around 270 K and was further dehydrogenated above 390 K to a C_3H_2 species. The hydrogen-rich LOHC counterpart THF showed a partial dehydrogenation and a formation of H_x-Furan, which started at around 140 K. The following reaction pathway of H_x-Furan includes similar reaction products as the reaction of furan, except the allylic species.

In the following section, the reactions of the LOHC compounds benzofuran and dihydrobenzofuran, which are structurally similar to indole and indoline and are the π-expanded version of furan, were discussed. The hydrogen-lean molecule benzofuran undergoes an undesired ring-opening reaction at the five-membered ring above 205 K on Pt(111). This reaction is followed by a dissociation of CO and the formation of a carbene intermediate above 240 K. The carbene-like / allylic species subsequently is dehydrogenated to C_7H_6 compound above 270 K. A further dehydrogenation of this compound was observed, which results in the formation of C_7H_4 at 370 K. Dihydrobenzofuran, which is hydrogenated at the five-membered ring, is dehydrogenated to a H_1-benzofuran intermediate above 150 K. Higher temperatures induce the same reaction pathway that was witnessed in the benzofuran experiments. After an undesired ring-opening reaction at 200 K and the cleavage CO at 270 K, the remaining C_7H_6 species was dehydrogenated to C_7H_4. As a result, the complete dehydrogenation of THF and dihydrobenzofuran to the hydrogen-lean LOHC species furan and benzofuran was not accomplished on Pt(111) due to an undesired ring-opening at relatively low temperatures. Therefore, these compounds are likely not suitable LOHC candidates on platinum surfaces.

A comparison of the structural features and functionalization of the LOHC, as well as the catalyst material are presented in Chapter 9.

10. Zusammenfassung

Flüssige organische Wasserstoffträger (LOHCs, von engl. liquid organic hydrogen carriers) sind Verbindungen, die sich für die chemische Wasserstoffspeicherung eignen. Diese Energiespeicherlösung ist insbesondere im Hinblick auf den fortschreitenden Ausbau von erneuerbaren Energiequellen interessant, da überschüssige Energie genutzt werden kann, um sogenannten grünen Wasserstoff zu produzieren. In einem LOHC-Zyklus wird ein wasserstoff- und energiearmes LOHC-Molekül katalytisch hydriert, wodurch eine wasserstoff- und energiereiche LOHC-Spezies entsteht. Wenn Energie benötigt wird, wird der gespeicherte Wasserstoff katalytisch freigesetzt. In bereits veröffentlichten Studien wurden N-heterozyklische Verbindungen wie N-Ethylcarbazol/H_{12}-N-Ethylcarbazol als vielversprechende LOHC-Kandidaten identifiziert. Diese Studien werden in dieser Arbeit fortgesetzt und konzentrieren sich auf die strukturell ähnlichen N-heterozyklischen LOHCs Indol/Indolin/Octahydroindol, 2,2'-Bipyridyl/2,2'-Bipiperidin, Pyridin/Piperidin und Pyrrol/Pyrrolidin. Darüber hinaus wurde das Reaktionsverhalten der LOHC-Verbindungen Furan/THF und Benzofuran/Dihydrobenzofuran auf Pt(111) untersucht.

In dieser Arbeit wurde das Dehydrierverhalten der genannten LOHC Moleküle unter modellkatalytischen Bedingungen untersucht. Nachdem die Wasserstoffträgermoleküle durch Gasphasenabscheidung auf die Modell-Katalysatoren Ni(111) und Pt(111) adsorbiert wurden, wurde das Dehydrierverhalten beobachtet. Um detaillierte Einblicke in die Reaktionswege der vorgestellten LOHCs zu erhalten, wurden verschiedene in der Oberflächenforschung gängige Methoden verwendet. Dazu zählen die synchrotron-basierte hochauflösende Röntgenphotoelektronenspektroskopie, temperaturprogrammierte Desorption und Röntgen-Nahkanten-Absorptions-Spektroskopie. Alle präsentierten Experimente fanden unter Ultrahochvakuumbedingungen statt. HR-XP-Spektren wurden mit Hilfe von Synchrotronstrahlung (BESSY II, Berlin) kontinuierlich gemessen, während die Temperatur der katalytischen Oberflächen linear erhöht wurde. Die in situ XPS-Experimente ermöglichten die Identifizierung von Reaktionsprodukten und Zwischenprodukten auf den katalytischen Oberflächen während der Dehydrierung. Die temperaturprogrammierte Desorption wurde als ergänzende Methode zur Erforschung der Wasserstoffdesorption (m/z = 2) eingesetzt.

Das erste in dieser Arbeit untersuchte LOHC-System ist Indol/Indolin/Octahydroindol auf Ni(111). Indol stellt die wasserstoffarme LOHC-Spezies dar, während Octahydroindol das vollständig hydrierte Gegenstück ist. Darüber hinaus wurde auch die teilweise hydrierte Verbindung Indolin, die am Fünfring hydriert ist, in die Untersuchungen einbezogen. Während des Heizexperiments (TPXPS) wurde die Dehydrierung von Indol am Stickstoffatom und die Bildung einer Indolid-Oberflächenspezies bei 130 K beobachtet. Für die Indolid-Spezies wurden keine weiteren Reaktionsschritte vor ihrer Zersetzung bei etwa 400 K festgestellt. Das teilhydrierte LOHC-Molekül Indolin zeigt einen ersten Reaktionsschritt bei 180 K, bei dem Dehydrierungen am Pyrrolring und am Stickstoffatom gleichzeitig stattfinden, was zur Bildung von Indolid führt. In diesem Experiment wurde die Zersetzung von Indolid bei etwa 380 K beobachtet. Der komplexere Reaktionspfad von Octahydroindol beginnt mit einer ersten Reaktion bei 230 K, bei der mehrere verschiedene Dehydrierungszwischenprodukte gebildet werden. Bei weiterem Erhitzen über 340 K reagieren die Dehydrierungszwischenprodukte zu Indolid, das bereits in den Indol- und Indolinversuchen identifiziert wurde. Die Indolid-Spezies wird jedoch von einem Ringöffnungsprodukt am Stickstoffatom und einem nur teilweise dehydrierten Octahydroindol begleitet. Unter realkatalytischen Bedingungen sollte die Bildung von Ringöffnungsprodukten vermieden werden, da dies zu einem Verlust von wiederverwendbaren LOHC-Molekülen führen würde. Darüber hinaus könnten Fragmente von LOHC-Molekülen den Katalysator vergiften und die weitere Dehydrierung von LOHC Molekülen beeinträchtigen. Die Reaktionswege von Indolin und Octahydroindol auf Ni(111) unterscheiden sich von denen auf Pt(111). Die Verwendung eines Nickelkatalysators für die Dehydrierung von Indolin scheint günstiger zu sein als die Verwendung von Platin, da die Dehydrierung bei niedrigeren Temperaturen beginnt (Ni(111): 180 K vs. Pt(111): 280 K). Für die Dehydrierung von Octahydroindol sollte vorzugsweise ein Platinkatalysator verwendet werden, da an dem Edelmetall die Dehydrierung bei niedrigeren Temperaturen (Pt(111): 280 K vs. Ni(111): 340 K) stattfindet und keine Bildung von unerwünschten Ringöffnungsprodukten erfolgt.

Im nächsten Abschnitt wurde das LOHC-System 2,2'-Bipyridyl/2,2'-Bipiperidin auf Ni(111) untersucht. Für die wasserstoffarme LOHC-Spezies 2,2'-Bipyridyl wurden trotz Submonolagen-Bedeckung schwach adsorbierte Multilagen auf einer ersten chemisorbierten Schicht gefunden. Die schwach physisorbierten Moleküle bewegen sich ab etwa 215 K zu vakanten Stellen auf der Nickeloberfläche. Die flach liegenden

2,2'-Bipyridylmoleküle werden in α-Position zu den beiden Stickstoffatomen an den sekundären Kohlenstoffatomen oberhalb von 370 K dehydriert. In diesem Reaktionsschritt entsteht eine α-2,2'-Bipyridyl-Spezies mit einer leicht gekippten Adsorptionsgeometrie. Vor der beginnenden Zersetzung bei 400 K wurden keine weiteren Reaktionsschritte von α-2,2'-Bipyridyl identifiziert. Das wasserstoffreiche Gegenstück 2,2'-Bipiperidin zeigt oberhalb von 180 K eine partielle Dehydrierung an den Kohlenstoffatomen. Anschließend wurde bei 250 K die Deprotonierung an den beiden Stickstoffatomen beobachtet. Eine weitere Temperaturerhöhung über 320 K induzierte einen weiteren Reaktionsschritt und die Bildung einer α-2,2'-Bipyridylverbindung, die bereits im Reaktionspfad des wasserstoffarmen 2,2'-Bipyridyls beobachtet wurde. Das Desorptionsmaximum von Wasserstoff wurde in TPD-Experimenten bei etwa 360 K gefunden. Neben der dehydrierten Spezies α-2,2'-Bipyridyl konnten wir auch geringe Mengen einer Verbindung identifizieren, die nur unvollständig an den Kohlenstoffatomen dehydriert ist. Das organische Molekülgerüst der Dehydrierungsprodukte zersetzte sich oberhalb von 400 K in Fragmente.

Im folgenden Kapitel wurde das Dehydrierverhalten der beiden strukturell ähnlichen LOHC-Systeme Pyridin/Piperidin und Pyrrol/Pyrrolidin diskutiert. Die wasserstoffarme Verbindung Pyridin zeigt oberhalb von 260 K eine Dehydrierung und die Bildung einer α-Pyridylspezies. Diese Verbindung wird bei Erwärmung oberhalb von 290 K weiter zu einem α,α-Pyridyl dehydriert, das an beiden Kohlenstoffatomen in α-Position zum Stickstoffatom dehydriert ist. Die Abspaltung eines Wasserstoffatoms in γ-Position zum Stickstoff wurde in einem konsekutiven Dehydrierungsschritt oberhalb von 380 K beobachtet, gefolgt von einem Zerfall in Fragmente oberhalb 410 K. Das wasserstoffreiche LOHC-Gegenstück Piperidin zeigt eine gleichzeitige Dehydrierung zu Pyridin und α-Pyridyl oberhalb von 290 K. Allerdings wurden oberhalb dieser Temperatur auch Ringöffnungsprodukte gefunden, die mit den gewünschten Reaktionsprodukten einhergingen und 12 % der gesamten Oberflächenbedeckung ausmachten. Es wird erwartet, dass die Ringöffnung an der C-N-Bindung des sechsgliedrigen Rings stattfindet. Ein weiteres Erhitzen über 380 K führt zur Bildung eines anderen Ringöffnungsprodukts, das wahrscheinlich durch eine Dissoziation einer C-C-Bindung verursacht wird. Die vollständige Fragmentierung wurde beim Heizexperiment oberhalb von 490 K beobachtet. Die Experimente des wasserstoffarmen LOHC Moleküls Pyrrol und des wasserstoffreichen Gegenstücks Pyrrolidin ergaben zum Teil identische

Reaktionsprodukte. Pyrrol wird bei relativ niedrigen Temperaturen am Stickstoffatom dehydriert. Kleine Mengen des Reaktionsprodukts wurden bereits während der Adsorption bei 130 K beobachtet. In einem folgenden Dehydrierschritt, welcher bei 270 K beginnt, wird ein Kohlenstoffatom in α-Position zum Stickstoffatom abgespalten und eine α-Pyrrolylverbindung gebildet. In einem weiteren Dehydrierungsschritt oberhalb von 400 K wird ein α,α-Pyrrolyl gebildet, da ein weiteres Wasserstoffatom in α-Position zum Stickstoffatom abgespalten wird. Die Fragmentierung des fünfgliedrigen Rings ist oberhalb von 450 K zu beobachten. Das wasserstoffreiche LOHC-Molekül Pyrrolidin reagiert oberhalb von 270 K direkt zu α-Pyrrolyl ohne weitere Zwischenprodukte, da die Dehydrierung am Stickstoffatom und an den Kohlenstoffatomen gleichzeitig erfolgt. Bemerkenswert ist, dass die Dehydrierung der wasserstoffreichen Verbindung ohne die Bildung von Ringöffnungsprodukten erfolgt, die bei der Dehydrierung von Piperidine beobachtet wurden. Oberhalb von 350 K wird die gleiche α,α-Pyrrolylspezies nachgewiesen, die bereits im Reaktionspfad von Pyrrol identifiziert wurde. Vor der Zersetzung oberhalb von 470 K wurden keine weiteren Reaktionsprodukte nachgewiesen. Der Vergleich der wasserstoffreichen Verbindungen Piperidin und Pyrrolidin zeigt, dass Pyrrolidin in LOHC-Systemen auf Nickelkatalysatoren in Bezug auf die thermische Stabilität der bessere Kandidat sein könnte. Der Nachteil eines LOHC Systems auf Basis von Pyrrolidin ist jedoch die etwas geringere Wasserstoffspeicherkapazität.

Die O-heterozyklischen LOHC-Systeme Furan/THF und Benzofuran/Dihydrobenzofuran auf Pt(111) wurden am Ende dieser Arbeit diskutiert. Das wasserstoffarme Molekül Furan zeigt bereits bei 210 K eine unerwünschte Ringöffnung. Bei weiterem Erhitzen über 240 K wurde die Bildung eines allylischen Zwischenprodukts beobachtet, während CO vom Ringöffnungsprodukt abgespalten wurde. Die allylische Spezies reagierte bei etwa 270 K zu einem C_3H_4-Fragment und wurde oberhalb von 390 K weiter zu einer C_3H_2-Spezies dehydriert. Das wasserstoffreiche LOHC-Gegenstück THF zeigte eine partielle Dehydrierung und eine Bildung von H_x-Furan, die bei etwa 140 K begann. Über die Anzahl der abgespaltenen Wasserstoffatome kann keine eindeutige Aussage gemacht werden. Der folgende Reaktionsweg von H_x-Furan beinhaltet ähnliche Reaktionsprodukte bei ähnlichen Temperaturen wie die Reaktion von Furan, mit Ausnahme der allylischen Spezies. Oberhalb von 200 K wird durch die Dissoziation einer C-O-Bindung ein Ringöffnungsprodukt gebildet. Bei weiterem Erhitzen über 260 K kommt es zur

Abspaltung von CO, während gleichzeitig die Bildung von C_3H_4 zu beobachten ist. Eine weitere Dehydrierung der C_3H_4-Verbindung zu einer C_3H_2-Spezies wird oberhalb von 390 K beobachtet. Im darauffolgenden Abschnitt wurden die Reaktionen der LOHC-Verbindungen Benzofuran und Dihydrobenzofuran, die eine ähnliche Struktur wie Indol und Indolin aufweisen, diskutiert. Das wasserstoffarme Molekül Benzofuran durchläuft eine unerwünschte Ringöffnungsreaktion am Fünfring oberhalb von 205 K auf Pt(111). Dieser Reaktion folgt eine Dissoziation von CO und die Bildung eines Carben-Zwischenprodukts bei 240 K. Die Carben-Spezies wird anschließend bei 270 K zu einer C_7H_6-Verbindung dehydriert. Eine weitere Dehydrierung dieser Verbindung konnte beobachtet werden, die bei 370 K zur Bildung von C_7H_4 führt. Dihydrobenzofuran, das am Fünfring hydriert wird, wird bei 150 K zu einem H_1-Benzofuran-Zwischenprodukt nur partiell dehydriert. Nach einer unerwünschten Ringöffnungsreaktion bei 200 K und der CO-Abspaltung bei 270 K wurde die verbleibende C_7H_6-Spezies zu C_7H_4 dehydriert. Die vollständige Dehydrierung von THF und Dihydrobenzofuran zu den wasserstoffarmen LOHC-Spezies Furan und Benzofuran konnte auf Pt(111) aufgrund einer unerwünschten Ringöffnung bei relativ niedrigen Temperaturen nicht erreicht werden. Daher sind diese Verbindungen wahrscheinlich keine geeigneten LOHC-Kandidaten für die platinkatalysierte Dehydrierung.

Insgesamt konzentriert sich diese Arbeit auf die Dehydrierung und die Reaktionsmechanismen von flüssigen organischen Wasserstoffträgersystemen auf wohldefinierten katalytischen Oberflächen unter Ultrahochvakuumbedingungen. Die Dehydrierreaktionen von N- und O-heterozyklischen LOHC-Materialien wurden an Nickel- und Platinkatalysatoren untersucht. Die Ergebnisse können zur Entwicklung künftiger LOHC-Materialien mit verbesserten Eigenschaften und ihrer Wechselwirkung mit verschiedenen katalytischen Oberflächen unter realkatalytischen Bedingungen beitragen. Damit kann ein Beitrag zur Entwicklung einer nachhaltigen und sicheren Form der Energiespeicherung für erneuerbare Energien geleistet werden.

11. References

1. Gerland, P.; Raftery Adrian, E.; Ševčíková, H.; Li, N.; Gu, D.; Spoorenberg, T.; Alkema, L.; Fosdick Bailey, K.; Chunn, J.; Lalic, N.; Bay, G.; Buettner, T.; Heilig Gerhard, K.; Wilmoth, J., World population stabilization unlikely this century. *Science* **2014,** *346* (6206), 234-237.
2. Liddle, B., Impact of population, age structure, and urbanization on carbon emissions/energy consumption: evidence from macro-level, cross-country analyses. *Population and Environment* **2014,** *35* (3), 286-304.
3. Fulkerson, W.; Judkins, R. R.; Sanghvi, M. K., Energy from Fossil Fuels. *Scientific American* **1990,** *263* (3), 128-135.
4. Armaroli, N.; Balzani, V., The Legacy of Fossil Fuels. *Chemistry – An Asian Journal* **2011,** *6* (3), 768-784.
5. Judkins, R. R.; Fulkerson, W.; Sanghvi, M. K., The dilemma of fossil fuel use and global climate change. *Energy Fuels* **1993,** *7* (1), 14-22.
6. Lashof, D. A.; Ahuja, D. R., Relative contributions of greenhouse gas emissions to global warming. *Nature* **1990,** *344* (6266), 529-531.
7. Wallington, T. J.; Srinivasan, J.; Nielsen, O. J.; Highwood, E. J., Greenhouse gases and global warming. *Environ Ecol Chem* **2009,** *1*, 36.
8. Letcher, T. M., 1 - Why do we have global warming? In *Managing Global Warming*, Letcher, T. M., Ed. Academic Press: 2019; pp 3-15.
9. Al-Ghussain, L., Global warming: review on driving forces and mitigation. *Environmental Progress & Sustainable Energy* **2019,** *38* (1), 13-21.
10. Company, B. P., Statistical Review of World Energy. **2020,** *69*.
11. Clémençon, R., The Two Sides of the Paris Climate Agreement: Dismal Failure or Historic Breakthrough? *The Journal of Environment & Development* **2016,** *25* (1), 3-24.
12. Jernnäs, M.; Linnér, B.-O., A discursive cartography of nationally determined contributions to the Paris climate agreement. *Global Environmental Change* **2019,** *55*, 73-83.
13. Jacobs, M., High pressure for low emissions: How civil society created the Paris climate agreement. *Juncture* **2016,** *22* (4), 314-323.

14. DeConto, R. M.; Pollard, D.; Alley, R. B.; Velicogna, I.; Gasson, E.; Gomez, N.; Sadai, S.; Condron, A.; Gilford, D. M.; Ashe, E. L.; Kopp, R. E.; Li, D.; Dutton, A., The Paris Climate Agreement and future sea-level rise from Antarctica. *Nature* **2021,** *593* (7857), 83-89.

15. Borchiellini, R.; Minuto, F. D., What Is Our Point of View on "Energy Independence and Research for Economic and Environmental Sustainability"? *Tecnica Italiana-Italian Journal of Engineering Science* **2020,** *64*, 60-62.

16. Jewell, J.; Vinichenko, V.; McCollum, D.; Bauer, N.; Riahi, K.; Aboumahboub, T.; Fricko, O.; Harmsen, M.; Kober, T.; Krey, V.; Marangoni, G.; Tavoni, M.; van Vuuren, D. P.; van der Zwaan, B.; Cherp, A., Comparison and interactions between the long-term pursuit of energy independence and climate policies. *Nature Energy* **2016,** *1* (6), 16073.

17. Inglesi-Lotz, R., The impact of renewable energy consumption to economic growth: A panel data application. *Energy Economics* **2016,** *53*, 58-63.

18. Ntanos, S.; Skordoulis, M.; Kyriakopoulos, G.; Arabatzis, G.; Chalikias, M.; Galatsidas, S.; Batzios, A.; Katsarou, A., Renewable Energy and Economic Growth: Evidence from European Countries. *Sustainability* **2018,** *10* (8).

19. Leonard, M. D.; Michaelides, E. E.; Michaelides, D. N., Energy storage needs for the substitution of fossil fuel power plants with renewables. *Renewable Energy* **2020,** *145*, 951-962.

20. Mulder, F. M., Implications of diurnal and seasonal variations in renewable energy generation for large scale energy storage. *Journal of Renewable and Sustainable Energy* **2014,** *6* (3), 033105.

21. Converse, A. O., Seasonal Energy Storage in a Renewable Energy System. *Proceedings of the IEEE* **2012,** *100* (2), 401-409.

22. Sun, Y.; Zhao, Z.; Yang, M.; Jia, D.; Pei, W.; Xu, B., Overview of energy storage in renewable energy power fluctuation mitigation. *CSEE Journal of Power and Energy Systems* **2020,** *6* (1), 160-173.

23. Teichmann, D.; Arlt, W.; Wasserscheid, P.; Freymann, R., A future energy supply based on Liquid Organic Hydrogen Carriers (LOHC). *Energ. Environ. Sci.* **2011,** *4* (8), 2767-2773.

24. Gençer, E.; Agrawal, R., A commentary on the US policies for efficient large scale renewable energy storage systems: Focus on carbon storage cycles. *Energy Policy* **2016,** *88*, 477-484.

25. Nagaraju, G.; Sekhar, S. C.; Ramulu, B.; Yu, J. S., An Integrated Approach Toward Renewable Energy Storage Using Rechargeable Ag@Ni0.67Co0.33S-Based Hybrid Supercapacitors. *Small* **2019,** *15* (16), 1805418.

26. Wang, S.; Wei, T.; Qi, Z. In *Supercapacitor Energy Storage Technology and its Application in Renewable Energy Power Generation System*, Proceedings of ISES World Congress 2007 (Vol. I – Vol. V), Berlin, Heidelberg, 2009//; Goswami, D. Y.; Zhao, Y., Eds. Springer Berlin Heidelberg: Berlin, Heidelberg, 2009; pp 2805-2809.

27. Chandra, A., Supercapacitors: An Alternate Technology for Energy Storage. *Proceedings of the National Academy of Sciences, India Section A: Physical Sciences* **2012,** *82* (1), 79-90.

28. He, S.; Hu, X.; Chen, S.; Hu, H.; Hanif, M.; Hou, H., Needle-like polyaniline nanowires on graphite nanofibers: hierarchical micro/nano-architecture for high performance supercapacitors. *J. Mater. Chem.* **2012,** *22* (11), 5114-5120.

29. Biswas, S.; Drzal, L. T., Multilayered Nano-Architecture of Variable Sized Graphene Nanosheets for Enhanced Supercapacitor Electrode Performance. *ACS Appl. Mater. Interfaces* **2010,** *2* (8), 2293-2300.

30. Qie, L.; Chen, W.; Xu, H.; Xiong, X.; Jiang, Y.; Zou, F.; Hu, X.; Xin, Y.; Zhang, Z.; Huang, Y., Synthesis of functionalized 3D hierarchical porous carbon for high-performance supercapacitors. *Energ. Environ. Sci.* **2013,** *6* (8), 2497-2504.

31. Dubey, R.; Guruviah, V., Review of carbon-based electrode materials for supercapacitor energy storage. *Ionics* **2019,** *25* (4), 1419-1445.

32. Zhang, F.; Zhang, T.; Yang, X.; Zhang, L.; Leng, K.; Huang, Y.; Chen, Y., A high-performance supercapacitor-battery hybrid energy storage device based on graphene-enhanced electrode materials with ultrahigh energy density. *Energ. Environ. Sci.* **2013,** *6* (5), 1623-1632.

33. Doughty, D. H.; Butler, P. C.; Akhil, A. A.; Clark, N. H.; Boyes, J. D., Batteries for Large-Scale Stationary Electrical Energy Storage. *The Electrochemical Society Interface* **2010,** *19* (3), 49-53.

34. Hameer, S.; van Niekerk, J. L., A review of large-scale electrical energy storage. *International Journal of Energy Research* **2015,** *39* (9), 1179-1195.

35. Koohi-Fayegh, S.; Rosen, M. A., A review of energy storage types, applications and recent developments. *Journal of Energy Storage* **2020,** *27*, 101047.
36. Dehghani-Sanij, A. R.; Tharumalingam, E.; Dusseault, M. B.; Fraser, R., Study of energy storage systems and environmental challenges of batteries. *Renewable and Sustainable Energy Reviews* **2019,** *104*, 192-208.
37. Eftekhari, A., On the Theoretical Capacity/Energy of Lithium Batteries and Their Counterparts. *ACS Sustainable Chemistry & Engineering* **2019,** *7* (4), 3684-3687.
38. Delmas, C., Sodium and Sodium-Ion Batteries: 50 Years of Research. *Advanced Energy Materials* **2018,** *8* (17), 1703137.
39. Buttler, A.; Spliethoff, H., Current status of water electrolysis for energy storage, grid balancing and sector coupling via power-to-gas and power-to-liquids: A review. *Renewable and Sustainable Energy Reviews* **2018,** *82*, 2440-2454.
40. Yan, Z.; Hitt, J. L.; Turner, J. A.; Mallouk, T. E., Renewable electricity storage using electrolysis. *Proceedings of the National Academy of Sciences* **2020,** *117* (23), 12558.
41. Chi, J.; Yu, H., Water electrolysis based on renewable energy for hydrogen production. *Chinese Journal of Catalysis* **2018,** *39* (3), 390-394.
42. Mittelsteadt, C. K., PEM Electrolysis: Ready for Impact. *ECS Trans.* **2015,** *69* (17), 205-211.
43. Barbir, F., PEM electrolysis for production of hydrogen from renewable energy sources. *Solar Energy* **2005,** *78* (5), 661-669.
44. Müller, B.; Müller, K.; Teichmann, D.; Arlt, W., Energiespeicherung mittels Methan und energietragenden Stoffen – ein thermodynamischer Vergleich. *Chem. Ing. Tech.* **2011,** *83* (11), 2002-2013.
45. Makowski, P.; Thomas, A.; Kuhn, P.; Goettmann, F., Organic materials for hydrogen storage applications: from physisorption on organic solids to chemisorption in organic molecules. *Energ. Environ. Sci.* **2009,** *2* (5), 480-490.
46. Dillon, A. C.; Jones, K. M.; Bekkedahl, T. A.; Kiang, C. H.; Bethune, D. S.; Heben, M. J., Storage of hydrogen in single-walled carbon nanotubes. *Nature* **1997,** *386* (6623), 377-379.
47. Tozzini, V.; Pellegrini, V., Prospects for hydrogen storage in graphene. *Phys. Chem. Chem. Phys.* **2013,** *15* (1), 80-89.

48. Sakintuna, B.; Lamari-Darkrim, F.; Hirscher, M., Metal hydride materials for solid hydrogen storage: A review. *Int. J. Hydrogen Energy* **2007,** *32* (9), 1121-1140.

49. Niermann, M.; Beckendorff, A.; Kaltschmitt, M.; Bonhoff, K., Liquid Organic Hydrogen Carrier (LOHC) – Assessment based on chemical and economic properties. *Int. J. Hydrogen Energy* **2019,** *44* (13), 6631-6654.

50. Brückner, N.; Obesser, K.; Bösmann, A.; Teichmann, D.; Arlt, W.; Dungs, J.; Wasserscheid, P., Evaluation of Industrially Applied Heat-Transfer Fluids as Liquid Organic Hydrogen Carrier Systems. *ChemSusChem* **2014,** *7* (1), 229-235.

51. Zou, Y.-Q.; von Wolff, N.; Anaby, A.; Xie, Y.; Milstein, D., Ethylene glycol as an efficient and reversible liquid-organic hydrogen carrier. *Nature Catalysis* **2019,** *2* (5), 415-422.

52. Fikrt, A.; Brehmer, R.; Milella, V.-O.; Müller, K.; Bösmann, A.; Preuster, P.; Alt, N.; Schlücker, E.; Wasserscheid, P.; Arlt, W., Dynamic power supply by hydrogen bound to a liquid organic hydrogen carrier. *Appl. Energy* **2017,** *194*, 1-8.

53. Hu, P.; Fogler, E.; Diskin-Posner, Y.; Iron, M. A.; Milstein, D., A novel liquid organic hydrogen carrier system based on catalytic peptide formation and hydrogenation. *Nature Communications* **2015,** *6* (1), 6859.

54. Zhong, H.; Iguchi, M.; Chatterjee, M.; Himeda, Y.; Xu, Q.; Kawanami, H., Formic Acid-Based Liquid Organic Hydrogen Carrier System with Heterogeneous Catalysts. *Advanced Sustainable Systems* **2018,** *2* (2), 1700161.

55. Rao, P. C.; Yoon, M., Potential Liquid-Organic Hydrogen Carrier (LOHC) Systems: A Review on Recent Progress. *Energies* **2020,** *13* (22).

56. Jorschick, H.; Geißelbrecht, M.; Eßl, M.; Preuster, P.; Bösmann, A.; Wasserscheid, P., Benzyltoluene/dibenzyltoluene-based mixtures as suitable liquid organic hydrogen carrier systems for low temperature applications. *Int. J. Hydrogen Energy* **2020,** *45* (29), 14897-14906.

57. Dong, Y.; Yang, M.; Li, L.; Zhu, T.; Chen, X.; Cheng, H., Study on reversible hydrogen uptake and release of 1,2-dimethylindole as a new liquid organic hydrogen carrier. *Int. J. Hydrogen Energy* **2019,** *44* (10), 4919-4929.

58. Chen, Z.; Yang, M.; Zhu, T.; Zhang, Z.; Chen, X.; Liu, Z.; Dong, Y.; Cheng, G.; Cheng, H., 7-ethylindole: A new efficient liquid organic hydrogen carrier with fast kinetics. *Int. J. Hydrogen Energy* **2018,** *43* (28), 12688-12696.

59. Geburtig, D.; Preuster, P.; Bösmann, A.; Müller, K.; Wasserscheid, P., Chemical utilization of hydrogen from fluctuating energy sources – Catalytic transfer hydrogenation from charged Liquid Organic Hydrogen Carrier systems. *Int. J. Hydrogen Energy* **2016,** *41* (2), 1010-1017.

60. Zhou, Q.-Q.; Zou, Y.-Q.; Ben-David, Y.; Milstein, D., A Reversible Liquid-to-Liquid Organic Hydrogen Carrier System Based on Ethylene Glycol and Ethanol. *Chem. Eur. J.* **2020,** *26* (67), 15487-15490.

61. Jang, M.; Jo, Y. S.; Lee, W. J.; Shin, B. S.; Sohn, H.; Jeong, H.; Jang, S. C.; Kwak, S. K.; Kang, J. W.; Yoon, C. W., A High-Capacity, Reversible Liquid Organic Hydrogen Carrier: H2-Release Properties and an Application to a Fuel Cell. *ACS Sustainable Chemistry & Engineering* **2019,** *7* (1), 1185-1194.

62. Kumar, A.; Janes, T.; Espinosa-Jalapa, N. A.; Milstein, D., Selective Hydrogenation of Cyclic Imides to Diols and Amines and Its Application in the Development of a Liquid Organic Hydrogen Carrier. *J. Am. Chem. Soc.* **2018,** *140* (24), 7453-7457.

63. Lee, S.; Kim, T.; Han, G.; Kang, S.; Yoo, Y.-S.; Jeon, S.-Y.; Bae, J., Comparative energetic studies on liquid organic hydrogen carrier: A net energy analysis. *Renewable and Sustainable Energy Reviews* **2021,** *150*, 111447.

64. Oh, J.; Jeong, K.; Kim, T. W.; Kwon, H.; Han, J. W.; Park, J. H.; Suh, Y.-W., 2-(N-Methylbenzyl)pyridine: A Potential Liquid Organic Hydrogen Carrier with Fast H2 Release and Stable Activity in Consecutive Cycles. *ChemSusChem* **2018,** *11* (4), 661-665.

65. Tang, C.; Fei, S.; Lin, G. D.; Liu, Y., Natural liquid organic hydrogen carrier with low dehydrogenation energy: A first principles study. *Int. J. Hydrogen Energy* **2020,** *45* (56), 32089-32097.

66. Garg, N.; Sarkar, A.; Sundararaju, B., Recent developments on methanol as liquid organic hydrogen carrier in transfer hydrogenation reactions. *Coord. Chem. Rev.* **2021,** *433*, 213728.

67. Shi, L.; Qi, S.; Qu, J.; Che, T.; Yi, C.; Yang, B., Integration of hydrogenation and dehydrogenation based on dibenzyltoluene as liquid organic hydrogen energy carrier. *Int. J. Hydrogen Energy* **2019,** *44* (11), 5345-5354.

68. Markiewicz, M.; Zhang, Y. Q.; Bösmann, A.; Brückner, N.; Thöming, J.; Wasserscheid, P.; Stolte, S., Environmental and health impact assessment of Liquid Organic

Hydrogen Carrier (LOHC) systems – challenges and preliminary results. *Energ. Environ. Sci.* **2015,** *8* (3), 1035-1045.

69. Markiewicz, M.; Zhang, Y.-Q.; Empl, M. T.; Lykaki, M.; Thöming, J.; Steinberg, P.; Stolte, S., Hazard assessment of quinaldine-, alkylcarbazole-, benzene- and toluene-based liquid organic hydrogen carrier (LOHCs) systems. *Energ. Environ. Sci.* **2019,** *12* (1), 366-383.
70. Papp, C.; Wasserscheid, P.; Libuda, J.; Steinrück, H.-P., Liquid Organic Hydrogen Carriers: Surface Science Studies of Carbazole Derivatives. *The Chemical Record* **2014,** *14* (5), 879-896.
71. Amende, M.; Gleichweit, C.; Werner, K.; Schernich, S.; Zhao, W.; Lorenz, M. P. A.; Höfert, O.; Papp, C.; Koch, M.; Wasserscheid, P.; Laurin, M.; Steinrück, H.-P.; Libuda, J., Model Catalytic Studies of Liquid Organic Hydrogen Carriers: Dehydrogenation and Decomposition Mechanisms of Dodecahydro-N-ethylcarbazole on Pt(111). *ACS Catal.* **2014,** *4* (2), 657-665.
72. Kiermaier, S.; Lehmann, D.; Bösmann, A.; Wasserscheid, P., Dehydrogenation of perhydro-N-ethylcarbazole under reduced total pressure. *Int. J. Hydrogen Energy* **2021,** *46* (29), 15660-15670.
73. Feng, Z.; Chen, X.; Bai, X., Catalytic dehydrogenation of liquid organic hydrogen carrier dodecahydro-N-ethylcarbazole over palladium catalysts supported on different supports. *Environmental Science and Pollution Research* **2020,** *27* (29), 36172-36185.
74. Amende, M.; Gleichweit, C.; Schernich, S.; Höfert, O.; Lorenz, M. P. A.; Zhao, W.; Koch, M.; Obesser, K.; Papp, C.; Wasserscheid, P.; Steinrück, H.-P.; Libuda, J., Size and Structure Effects Controlling the Stability of the Liquid Organic Hydrogen Carrier Dodecahydro-N-ethylcarbazole during Dehydrogenation over Pt Model Catalysts. *The Journal of Physical Chemistry Letters* **2014,** *5* (8), 1498-1504.
75. Sievi, G.; Geburtig, D.; Skeledzic, T.; Bösmann, A.; Preuster, P.; Brummel, O.; Waidhas, F.; Montero, M. A.; Khanipour, P.; Katsounaros, I.; Libuda, J.; Mayrhofer, K. J. J.; Wasserscheid, P., Towards an efficient liquid organic hydrogen carrier fuel cell concept. *Energ. Environ. Sci.* **2019,** *12* (7), 2305-2314.
76. Peters, R.; Deja, R.; Fang, Q.; Nguyen, V. N.; Preuster, P.; Blum, L.; Wasserscheid, P.; Stolten, D., A solid oxide fuel cell operating on liquid organic hydrogen carrier-

based hydrogen – A kinetic model of the hydrogen release unit and system performance. *Int. J. Hydrogen Energy* **2019,** *44* (26), 13794-13806.

77. Dürr, S.; Zilm, S.; Geißelbrecht, M.; Müller, K.; Preuster, P.; Bösmann, A.; Wasserscheid, P., Experimental determination of the hydrogenation/dehydrogenation - Equilibrium of the LOHC system H0/H18-dibenzyltoluene. *Int. J. Hydrogen Energy* **2021,** *46* (64), 32583-32594.
78. Modisha, P.; Bessarabov, D., Stress tolerance assessment of dibenzyltoluene-based liquid organic hydrogen carriers. *Sustainable Energy & Fuels* **2020,** *4* (9), 4662-4670.
79. Balerna, A.; Mobilio, S., Introduction to Synchrotron Radiation. In *Synchrotron Radiation: Basics, Methods and Applications*, Mobilio, S.; Boscherini, F.; Meneghini, C., Eds. Springer Berlin Heidelberg: Berlin, Heidelberg, 2015; pp 3-28.
80. Codling, K., Applications of synchrotron radiation (ultraviolet spectral light source). *Reports on Progress in Physics* **1973,** *36* (5), 541-624.
81. Patterson, B. D., A simplified approach to synchrotron radiation. *American Journal of Physics* **2011,** *79* (10), 1046-1052.
82. Povh, B.; Rith, K.; Scholz, C.; Zetsche, F.; Rodejohann, W., *Teilchen und Kerne: eine Einführung in die physikalischen Konzepte*. Springer-Verlag: 2013.
83. Brown, G.; Halbach, K.; Harris, J.; Winick, H., Wiggler and undulator magnets — A review. *Nuclear Instruments and Methods in Physics Research* **1983,** *208* (1), 65-77.
84. Chavanne, J.; Elleaume, P., Undulator and wiggler shimming. *Synchrotron Radiation News* **1995,** *8* (1), 18-22.
85. Gudat, W.; Pflüger, J., Undulator-wiggler magnets for low energy storage rings. *Zeitschrift für Physik B Condensed Matter* **1985,** *61* (4), 483-491.
86. Murphy, J. B.; Pellegrini, C., Generation of high-intensity coherent radiation in the soft-x-ray and vacuum-ultraviolet region. *Journal of the Optical Society of America B* **1985,** *2* (1), 259-264.
87. Miles, A. J.; Wallace, B. A., Synchrotron radiation circular dichroism spectroscopy of proteins and applications in structural and functional genomics. *Chem. Soc. Rev.* **2006,** *35* (1), 39-51.
88. Meuli, R.; Hwu, Y.; Je, J. H.; Margaritondo, G., Synchrotron radiation in radiology: radiology techniques based on synchrotron sources. *European Radiology* **2004,** *14* (9), 1550-1560.

89. Dietrich, P. M.; Glamsch, S.; Ehlert, C.; Lippitz, A.; Kulak, N.; Unger, W. E. S., Synchrotron-radiation XPS analysis of ultra-thin silane films: Specifying the organic silicon. *Appl. Surf. Sci.* **2016,** *363*, 406-411.

90. Carravetta, V.; Iucci, G.; Ferri, A.; Russo, M. V.; Stranges, S.; de Simone, M.; Polzonetti, G., Synchrotron radiation photoemission study of some π-conjugated alkynes in the gas phase: Experiment and theory. *Chem. Phys.* **2001,** *264* (2), 175-186.

91. Sivkov, V. N.; Petrova, O. V.; Nekipelov, S. V.; Obiedkov, A. M.; Kaverin, B. S.; Kirillov, A. I.; Semenov, N. M.; Domrachev, G. A.; Egorov, V. A.; Gusev, S. A.; Vyalikh, D. V.; Molodtsov, S. L., NEXAFS Study of the Composite Materials MWCNTs—Pyrolytic Metals by Synchrotron Radiation. *Fullerenes, Nanotubes and Carbon Nanostructures* **2015,** *23* (1), 17-19.

92. Yannoulis, P.; Dudde, R.; Frank, K. H.; Koch, E. E., Orientation of aromatic hydrocarbons on metal surfaces as determined by nexafs. *Surf. Sci.* **1987,** *189-190*, 519-528.

93. Rosenbaum, G.; Holmes, K. C.; Witz, J., Synchrotron Radiation as a Source for X-ray Diffraction. *Nature* **1971,** *230* (5294), 434-437.

94. Hertz, H., Ueber einen Einfluss des ultravioletten Lichtes auf die electrische Entladung. *Annalen der Physik* **1887,** *267* (8), 983-1000.

95. Wheaton, B. R., Photoelectric Effect. In *Compendium of Quantum Physics*, Greenberger, D.; Hentschel, K.; Weinert, F., Eds. Springer Berlin Heidelberg: Berlin, Heidelberg, 2009; pp 472-475.

96. Einstein, A., *Ann. Phys.* **1905,** *322*, 132-148.

97. Niaz, M.; Klassen, S.; McMillan, B.; Metz, D., Reconstruction of the history of the photoelectric effect and its implications for general physics textbooks. *Science Education* **2010,** *94* (5), 903-931.

98. Kobayashi, K., Hard X-ray photoemission spectroscopy. *Nuclear Instruments and Methods in Physics Research Section A: Accelerators, Spectrometers, Detectors and Associated Equipment* **2009,** *601* (1), 32-47.

99. Wertheim, G. K., X-Ray Photoelectron Spectroscopy of Solids. In *Electron and Ion Spectroscopy of Solids*, Fiermans, L.; Vennik, J.; Dekeyser, W., Eds. Springer US: Boston, MA, 1978; pp 192-229.

100. Pettersson, L.; Nordgren, J.; Selander, L.; Nordling, C.; Siegbahn, K.; Ågren, H., Core-electron binding energies in the soft X-ray range obtained in X-ray emission. *J. Electron Spectrosc. Relat. Phenom.* **1982,** *27* (1), 29-37.

101. Hüfner, S., *Photoelectron Spectroscopy: Principles And Applications*. Springer: Berlin-Heidelberg, **2013**.

102. Siegbahn, K.; Nordling, C.; Fahlman, A.; Nordberg, H.; Hamrin, K.; Hedman, J.; Johannson, G.; Bergmark, T.; Karlsson, S. E.; Lindgren, J.; Lindberg, B., *Electron Spectroscopy for Chemical Analysis; Atomic, Molecular and Solid State Structure Studies by means of Electron Spectroscopy*. Almquist and Wiksells: Stockholm, **1967**.

103. Seah, M. P.; Dench, W. A., *Surf. Interface Anal.* **1979,** *1*, 2-11.

104. Heide, P. v. d., *Photoelectron Spectroscopy: An introduction to Prinicples and Particles*. Wiley, : 2011.

105. Mårtensson, N.; Nilsson, A., Core-Level line shapes of adsorbates: effects of electronic and vibrational excitations. *J. Electron Spectrosc. Relat. Phenom.* **1990,** *52*, 1-46.

106. Brundle, C. R.; Crist, B. V., X-ray photoelectron spectroscopy: A perspective on quantitation accuracy for composition analysis of homogeneous materials. *Journal of Vacuum Science & Technology A* **2020,** *38* (4), 041001.

107. Brisk, M. A.; Baker, A. D., Shake-up satellites in X-ray photoelectron spectroscopy. *J. Electron Spectrosc. Relat. Phenom.* **1975,** *7* (3), 197-213.

108. Papp, C.; Steinrück, H.-P., In situ high-resolution X-ray photoelectron spectroscopy – Fundamental insights in surface reactions. *Surf. Sci. Rep.* **2013,** *68* (3), 446-487.

109. Föhlisch, A.; Hasselström, J.; Karis, O.; Menzel, D.; Mårtensson, N.; Nilsson, A., Vibrational fine structure in core level photoelectron lines of adsorbed molecules: System dependent effects. *J. Electron Spectrosc. Relat. Phenom.* **1999,** *101-103*, 303-308.

110. Sutter, P.; Sadowski, J. T.; Sutter, E., Graphene on Pt(111): Growth and substrate interaction. *Phys. Rev. B* **2009,** *80* (24), 245411.

111. Dhez, O.; Ade, H.; Urquhart, S. G., Calibrated NEXAFS spectra of some common polymers. *J. Electron Spectrosc. Relat. Phenom.* **2003,** *128* (1), 85-96.

112. Watts, B.; Thomsen, L.; Dastoor, P. C., Methods in carbon K-edge NEXAFS: Experiment and analysis. *J. Electron Spectrosc. Relat. Phenom.* **2006,** *151* (2), 105-120.

113. Chen, J. G., NEXAFS investigations of transition metal oxides, nitrides, carbides, sulfides and other interstitial compounds. *Surf. Sci. Rep.* **1997,** *30* (1), 1-152.

114. Stöhr, J., *NEXAFS spectroscopy*. Springer Science & Business Media: 1992; Vol. 25.

115. Breuer, T.; Klues, M.; Witte, G., Characterization of orientational order in π-conjugated molecular thin films by NEXAFS. *J. Electron Spectrosc. Relat. Phenom.* **2015,** *204*, 102-115.

116. Stöhr, J., Principles, Techniques, and Instrumentation of NEXAFS. In *NEXAFS Spectroscopy*, Stöhr, J., Ed. Springer Berlin Heidelberg: Berlin, Heidelberg, 1992; pp 114-161.

117. Falconer, J. L.; Schwarz, J. A., Temperature-Programmed Desorption and Reaction: Applications to Supported Catalysts. *Catal. Rev.* **1983,** *25* (2), 141-227.

118. Cvetanović, R. J.; Amenomiya, Y., Application of a Temperature-Programmed Desorption Technique to Catalyst Studies. In *Adv. Catal.*, Eley, D. D.; Pines, H.; Weisz, P. B., Eds. Academic Press: 1967; Vol. 17, pp 103-149.

119. Miller, J. T.; Meyers, B. L.; Modica, F. S.; Lane, G. S.; Vaarkamp, M.; Koningsberger, D. C., Hydrogen Temperature-Programmed Desorption (H2 TPD) of Supported Platinum Catalysts. *J. Catal.* **1993,** *143* (2), 395-408.

120. Elliott, J. A. W.; Ward, C. A., Temperature programmed desorption: A statistical rate theory approach. *J. Chem. Phys.* **1997,** *106* (13), 5677-5684.

121. Rakić, V.; Damjanović, L., Temperature-Programmed Desorption (TPD) Methods. In *Calorimetry and Thermal Methods in Catalysis*, Auroux, A., Ed. Springer Berlin Heidelberg: Berlin, Heidelberg, 2013; pp 131-174.

122. Muhler, M.; Nielsen, L. P.; Törnqvist, E.; Clausen, B. S.; Topsøe, H., Temperature-programmed desorption of H2 as a tool to determine metal surface areas of Cu catalysts. *Catal. Lett.* **1992,** *14* (3), 241-249.

123. Castro, F. J.; Meyer, G., Thermal desorption spectroscopy (TDS) method for hydrogen desorption characterization (I): theoretical aspects. *J. Alloys Compd.* **2002,** *330-332*, 59-63.

124. Feulner, P.; Menzel, D., *J. Vac. Sci. Technol.* **1980,** *17*, 662–663.

125. Niemantsverdriet, J. W., *Spectroscopy in Catalysis: An Introduction*. Wiley: 2007.

126. Redhead, P. A., Thermal desorption of gases. *Vacuum* **1962,** *12* (4), 203-211.

127. Hubbard, A. T., *The Handbook of Surface Imaging and Visualization*. Taylor & Francis: 1995.

128. Parastaev, A.; Hoeben, W. F. L. M.; van Heesch, B. E. J. M.; Kosinov, N.; Hensen, E. J. M., Temperature-programmed plasma surface reaction: An approach to determine plasma-catalytic performance. *Applied Catalysis B: Environmental* **2018,** *239*, 168-177.

129. de Jong, A. M.; Niemantsverdriet, J. W., Thermal desorption analysis: Comparative test of ten commonly applied procedures. *Surf. Sci.* **1990,** *233* (3), 355-365.

130. Chou, T. Y.; Hwang, C. P.; Yeh, C. T., Graphic determination of kinetic parameters in temperature-programmed desorption of oxygen from alumeva-supported PdO. *J. Therm. Anal.* **1996,** *46* (1), 305-315.

131. Miller, J. B.; Siddiqui, H. R.; Gates, S. M.; Russell, J. N.; Yates, J. T.; Tully, J. C.; Cardillo, M. J., Extraction of kinetic parameters in temperature programmed desorption: A comparison of methods. *J. Chem. Phys.* **1987,** *87* (11), 6725-6732.

132. Rudzinski, W.; Borowiecki, T.; Panczyk, T.; Dominko, A., On the applicability of Arrhenius plot methods to determine surface energetic heterogeneity of adsorbents and catalysts surfaces from experimental TPD spectra. *Adv. Colloid Interface Sci.* **2000,** *84* (1), 1-26.

133. Denecke, R.; Kinne, M.; Whelan, C. M.; Steinrück, H. P., In-situ core-level photoelectron spectroscopy of adsorbates on surfaces involving a molecular beam — General setup and first experiments. *Surf. Rev. Lett.* **2002,** *09* (02), 797-801.

134. Gleichweit, C., Dehydrogenation of Liquid Organic Hydrogen Carriers on Model Catalyst Surfaces. Ph. D. thesis, Universität Erlangen-Nürnberg. **2015**.

135. Odahara, G.; Otani, S.; Oshima, C.; Suzuki, M.; Yasue, T.; Koshikawa, T., In-situ observation of graphene growth on Ni(111). *Surf. Sci.* **2011,** *605* (11), 1095-1098.

136. Bachmann, P.; Düll, F.; Späth, F.; Bauer, U.; Steinrück, H.-P.; Papp, C., A HR-XPS study of the formation of h-BN on Ni(111) from the two precursors, ammonia borane and borazine. *J. Chem. Phys.* **2018,** *149* (16), 164709.

137. Auwärter, W.; Kreutz, T. J.; Greber, T.; Osterwalder, J., XPD and STM investigation of hexagonal boron nitride on Ni(111). *Surf. Sci.* **1999,** *429* (1), 229-236.

138. Toyoshima, R.; Yoshida, M.; Monya, Y.; Suzuki, K.; Amemiya, K.; Mase, K.; Mun, B. S.; Kondoh, H., A high-pressure-induced dense CO overlayer on a Pt(111) surface: a

chemical analysis using in situ near ambient pressure XPS. *Phys. Chem. Chem. Phys.* **2014,** *16* (43), 23564-23567.

139. Kinne, M.; Fuhrmann, T.; Whelan, C. M.; Zhu, J. F.; Pantförder, J.; Probst, M.; Held, G.; Denecke, R.; Steinrück, H. P., Kinetic parameters of CO adsorbed on Pt(111) studied by in situ high resolution x-ray photoelectron spectroscopy. *J. Chem. Phys.* **2002,** *117* (23), 10852-10859.
140. Bach, W., Fossil fuel resources and their impacts on environment and climate. *Int. J. Hydrogen Energy* **1981,** *6* (2), 185-201.
141. Nicoletti, G.; Arcuri, N.; Nicoletti, G.; Bruno, R., A technical and environmental comparison between hydrogen and some fossil fuels. *Energy Conversion and Management* **2015,** *89*, 205-213.
142. Shafiee, S.; Topal, E., When will fossil fuel reserves be diminished? *Energy Policy* **2009,** *37* (1), 181-189.
143. Hall, P. J., Energy storage: The route to liberation from the fossil fuel economy? *Energy Policy* **2008,** *36* (12), 4363-4367.
144. Eberle, U.; Felderhoff, M.; Schüth, F., Chemical and Physical Solutions for Hydrogen Storage. *Angew. Chem. Int. Ed.* **2009,** *48* (36), 6608-6630.
145. Teichmann, D.; Arlt, W.; Wasserscheid, P., *Int. J. Hydrogen Energy* **2012,** *37*, 18118.
146. Li, L.; Yang, M.; Dong, Y.; Mei, P.; Cheng, H., Hydrogen storage and release from a new promising Liquid Organic Hydrogen Storage Carrier (LOHC): 2-methylindole. *Int. J. Hydrogen Energy* **2016,** *41* (36), 16129-16134.
147. Teichmann, D.; Arlt, W.; Wasserscheid, P., Liquid Organic Hydrogen Carriers as an efficient vector for the transport and storage of renewable energy. *Int. J. Hydrogen Energy* **2012,** *37* (23), 18118-18132.
148. Yang, M.; Dong, Y.; Fei, S.; Pan, Q.; Ni, G.; Han, C.; Ke, H.; Fang, Q.; Cheng, H., Hydrogenation of N-propylcarbazole over supported ruthenium as a new prototype of liquid organic hydrogen carriers (LOHC). *RSC Adv.* **2013,** *3* (47), 24877-24881.
149. Bachmann, P.; Steinhauer, J.; Späth, F.; Düll, F.; Bauer, U.; Eschenbacher, R.; Hemauer, F.; Scheuermeyer, M.; Bösmann, A.; Büttner, M.; Neiß, C.; Görling, A.; Wasserscheid, P.; Steinrück, H.-P.; Papp, C., Dehydrogenation of the liquid organic hydrogen carrier system 2-methylindole/2-methylindoline/2-methyloctahydroindole on Pt(111). *J. Chem. Phys.* **2019,** *151* (14), 144711.

150. Gleichweit, C.; Amende, M.; Schernich, S.; Zhao, W.; Lorenz, M. P. A.; Höfert, O.; Brückner, N.; Wasserscheid, P.; Libuda, J.; Steinrück, H. P.; Papp, C., *ChemSusChem* **2013,** *6*, 974.

151. Bachmann, P.; Schwarz, M.; Steinhauer, J.; Späth, F.; Düll, F.; Bauer, U.; Nascimento Silva, T.; Mohr, S.; Hohner, C.; Scheuermeyer, M.; Wasserscheid, P.; Libuda, J.; Steinrück, H. P.; Papp, C., Dehydrogenation of the Liquid Organic Hydrogen Carrier System Indole/Indoline/Octahydroindole on Pt(111). *J. Phys. Chem. C* **2018,** *122* (8), 4470-4479.

152. Schwarz, M.; Bachmann, P.; Silva, T. N.; Mohr, S.; Scheuermeyer, M.; Späth, F.; Bauer, U.; Düll, F.; Steinhauer, J.; Hohner, C.; Döpper, T.; Noei, H.; Stierle, A.; Papp, C.; Steinrück, H.-P.; Wasserscheid, P.; Görling, A.; Libuda, J., Model Catalytic Studies of Novel Liquid Organic Hydrogen Carriers: Indole, Indoline and Octahydroindole on Pt(111). *Chem. Eur. J.* **2017,** *23* (59), 14806-14818.

153. Ahmed, K.; Chowdhury, H. M., Dehydrogenation of cyclohexane and cyclohexene over supported nickel and platinum catalysts. *The Chemical Engineering Journal* **1992,** *50* (3), 165-168.

154. Uemichi, Y.; Sakai, T.; Kanazuka, T., Dehydrogenation of Cyclohexanol to Cyclohexanone on Supported Nickel Catalysts. *Chem. Lett.* **1989,** *18* (5), 777-780.

155. Lorenz, M. P. A.; Fuhrmann, T.; Streber, R.; Bayer, A.; Bebensee, F.; Gotterbarm, K.; Kinne, M.; Tränkenschuh, B.; Zhu, J. F.; Papp, C.; Denecke, R.; Steinrück, H. P., Ethene adsorption and dehydrogenation on clean and oxygen precovered Ni(111) studied by high resolution x-ray photoelectron spectroscopy. *J. Chem. Phys.* **2010,** *133* (1), 014706.

156. Papp, C.; Denecke, R.; Steinrück, H. P., Adsorption and Reaction of Cyclohexene on a Ni(111) Surface. *Langmuir* **2007,** *23* (10), 5541-5547.

157. Papp, C.; Fuhrmann, T.; Tränkenschuh, B.; Denecke, R.; Steinrück, H. P., Site selectivity of benzene adsorption on Ni(111) studied by high-resolution x-ray photoelectron spectroscopy. *Phys. Rev. B* **2006,** *73* (23), 235426.

158. Mohsenzadeh, A.; Bolton, K.; Richards, T., DFT study of the adsorption and dissociation of water on Ni(111), Ni(110) and Ni(100) surfaces. *Surf. Sci.* **2014,** *627*, 1-10.

159. Beebe, T. P.; Goodman, D. W.; Kay, B. D.; Yates, J. T., Kinetics of the activated dissociative adsorption of methane on the low index planes of nickel single crystal surfaces. *J. Chem. Phys.* **1987,** *87* (4), 2305-2315.

160. Kishi, K.; Ehara, Y., Interaction of acetic acid with ethylenediamine on a Ni(111) surface studied by XPS. *Surf. Sci.* **1986,** *176* (3), 567-577.

161. Smykalla, L.; Shukrynau, P.; Mende, C.; Lang, H.; Knupfer, M.; Hietschold, M., Photoelectron spectroscopy investigation of the temperature-induced deprotonation and substrate-mediated hydrogen transfer in a hydroxyphenyl-substituted porphyrin. *Chem. Phys.* **2015,** *450-451*, 39-45.

162. Christmann, K.; Schober, O.; Ertl, G.; Neumann, M., Adsorption of hydrogen on nickel single crystal surfaces. *J. Chem. Phys.* **1974,** *60* (11), 4528-4540.

163. Cohen, M. R.; Merrill, R. P., Adsorption of pyridine on Ni(111): A high-resolution electron energy loss spectroscopy, angular-resolved UV photoemission, and x-ray photoelectron spectroscopy study. **1990**.

164. Ouma, C. N. M.; Modisha, P. M.; Bessarabov, D., Catalytic dehydrogenation of the liquid organic hydrogen carrier octahydroindole on Pt (1 1 1) surface: Ab initio insights from density functional theory calculations. *Appl. Surf. Sci.* **2019,** *471*, 1034-1040.

165. Dean, D.; Davis, B.; Jessop, P. G., The effect of temperature, catalyst and sterics on the rate of N-heterocycle dehydrogenation for hydrogen storage. *New J. Chem.* **2011,** *35* (2), 417-422.

166. Trapnell, B. M. W., Specificity in catalysis by metals. *Quarterly Reviews, Chemical Society* **1954,** *8* (4), 404-421.

167. He, T.; Pei, Q.; Chen, P., Liquid organic hydrogen carriers. *Journal of Energy Chemistry* **2015,** *24* (5), 587-594.

168. Artyushkova, K., Misconceptions in interpretation of nitrogen chemistry from x-ray photoelectron spectra. *Journal of Vacuum Science & Technology A* **2020,** *38* (3), 031002.

169. Wöckel, C.; Eilert, A.; Welke, M.; Schöppke, M.; Steinrück, H.-P.; Denecke, R., Pyridine on flat Pt(111) and stepped Pt(355)—An in situ HRXPS investigation of adsorption and thermal evolution. *J. Chem. Phys.* **2016,** *144* (1), 014702.

170. Zuo, C.; Jagodzinski, P. W., Surface-Enhanced Raman Scattering of Pyridine Using Different Metals: Differences and Explanation Based on the Selective Formation of

α-Pyridyl on Metal Surfaces. *The Journal of Physical Chemistry B* **2005,** *109* (5), 1788-1793.

171. Connolly, M.; Somers, J.; Bridge, M. E.; Lloyd, D. R., Angular resolved photoemission studies of pyridine on Pt(111)—Evidence for an α-pyridyl species. *Surf. Sci.* **1987,** *185* (3), 559-568.
172. Harradine, D.; Campion, A., Surface Raman spectroscopy without enhancement: pyridine adsorbed on Ni(111) and Ni(100). *Chem. Phys. Lett.* **1987,** *135* (6), 501-505.
173. Sasse, W. H. F.; Whittle, C. P., Synthetical Applications of Activated Metal Catalysts. XVI. The Role of Hydrogen in the Formation of 2,2'-Bipyridyl from Pyridine under the Influence of Degassed Raney Nickel. *Aust. J. Chem.* **1963,** *16* (1), 14-19.
174. Winkler, A.; Rendulic, K. D., Adsorption kinetics for hydrogen adsorption on nickel and coadsorption of hydrogen and oxygen. *Surf. Sci.* **1982,** *118* (1), 19-31.
175. Gleichweit, C.; Amende, M.; Höfert, O.; Xu, T.; Späth, F.; Brückner, N.; Wasserscheid, P.; Libuda, J.; Steinrück, H.-P.; Papp, C., Surface Reactions of Dicyclohexylmethane on Pt(111). *J. Phys. Chem. C* **2015,** *119* (35), 20299-20311.
176. Xu, C.; Koel, B. E.; Newton, M. A.; Frei, N. A.; Campbell, C. T., Dehydrogenation of Methylcyclohexane on Pt(111). *J. Phys. Chem.* **1995,** *99* (45), 16670-16675.
177. Steinhauer, J.; Bachmann, P.; Freiberger, E. M.; Bauer, U.; Steinrück, H. P.; Papp, C., Model Catalytic Studies of Liquid Organic Hydrogen Carriers: Indole/Indoline/Octahydroindole on Ni(111). *J. Phys. Chem. C* **2020,** *124* (41), 22559-22567.
178. Bockris, J., Energy: the solar-hydrogen alternative. *nyhp* **1975**.
179. Crabtree, R. H., Hydrogen storage in liquid organic heterocycles. *Energ. Environ. Sci.* **2008,** *1* (1), 134-138.
180. Fisher, G. B.; Gland, J. L., The interaction of water with the Pt(111) surface. *Surf. Sci.* **1980,** *94* (2), 446-455.
181. Ogasawara, H.; Brena, B.; Nordlund, D.; Nyberg, M.; Pelmenschikov, A.; Pettersson, L. G. M.; Nilsson, A., Structure and Bonding of Water on Pt(111). *Phys. Rev. Lett.* **2002,** *89* (27), 276102.
182. Kliewer, C. J.; Aliaga, C.; Bieri, M.; Huang, W.; Tsung, C.-K.; Wood, J. B.; Komvopoulos, K.; Somorjai, G. A., Furan Hydrogenation over Pt(111) and Pt(100) Single-Crystal Surfaces and Pt Nanoparticles from 1 to 7 nm: A Kinetic and Sum Frequency

Generation Vibrational Spectroscopy Study. *J. Am. Chem. Soc.* **2010,** *132* (37), 13088-13095.

183. Kinne, M.; Fuhrmann, T.; Zhu, J. F.; Tränkenschuh, B.; Denecke, R.; Steinrück, H. P., Coadsorption of D2O and CO on Pt(111) Studied by in Situ High-Resolution X-ray Photoelectron Spectroscopy. *Langmuir* **2004,** *20* (5), 1819-1826.
184. Kinne, M.; Fuhrmann, T.; Zhu, J. F.; Whelan, C. M.; Denecke, R.; Steinrück, H. P., Kinetics of the CO oxidation reaction on Pt(111) studied by in situ high-resolution x-ray photoelectron spectroscopy. *J. Chem. Phys.* **2004,** *120* (15), 7113-7122.
185. Henn, F. C.; Diaz, A. L.; Bussell, M. E.; Hugenschmidt, M. B.; Domagala, M. E.; Campbell, C. T., Decomposition of cyclohexene on platinum (111): a BPTDS and HREELS study. *J. Phys. Chem.* **1992,** *96* (14), 5965-5974.
186. Vasiliou, A.; Nimlos, M. R.; Daily, J. W.; Ellison, G. B., Thermal Decomposition of Furan Generates Propargyl Radicals. *The Journal of Physical Chemistry A* **2009,** *113* (30), 8540-8547.
187. Yang, M.-L.; Zhu, Y.-A.; Fan, C.; Sui, Z.; Chen, D., DFT study of propane dehydrogenation on Pt catalyst: Effects of step sites. *Physical chemistry chemical physics : PCCP* **2011,** *13*, 3257-67.
188. Fichthorn, K. A.; Balan, P. G.; Chen, Y., Simulation and analysis of the motion of n-butane on Pt(111). *Surf. Sci.* **1994,** *317* (1), 37-44.
189. Zhang, R.; Hensley, A. J.; McEwen, J.-S.; Wickert, S.; Darlatt, E.; Fischer, K.; Schöppke, M.; Denecke, R.; Streber, R.; Lorenz, M.; Papp, C.; Steinrück, H.-P., Integrated X-ray photoelectron spectroscopy and DFT characterization of benzene adsorption on Pt(111), Pt(355) and Pt(322) surfaces. *Phys. Chem. Chem. Phys.* **2013,** *15* (47), 20662-20671.

Appendix

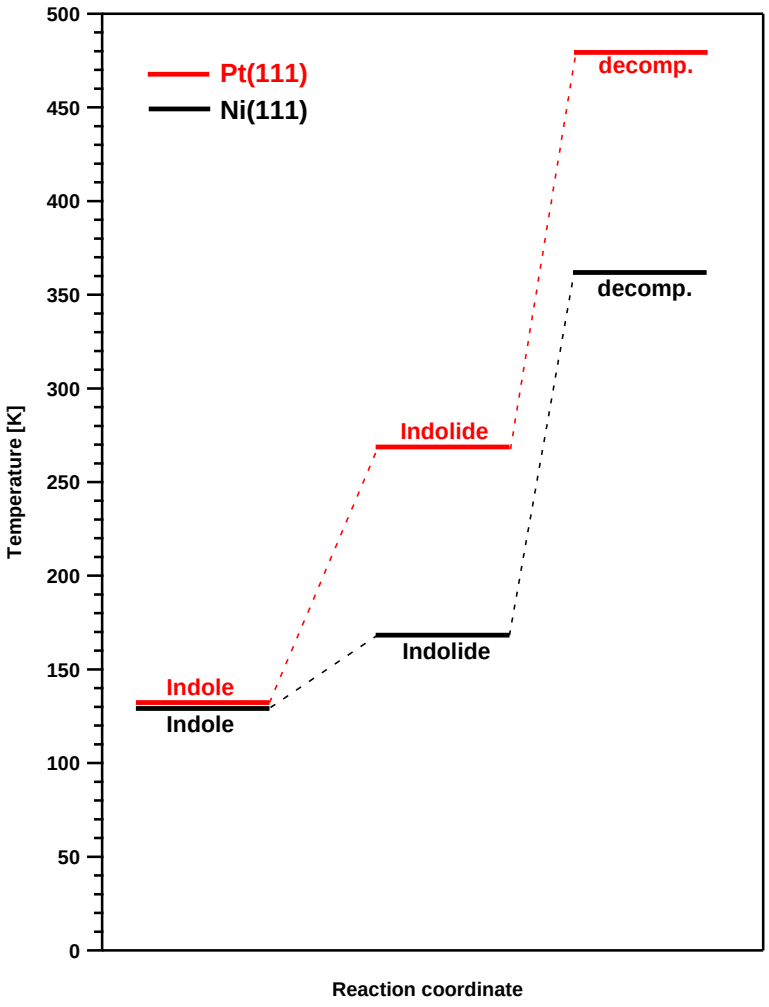

Figure A 1: Comparison between the reaction pathways of indole on Ni(111) and Pt(111).

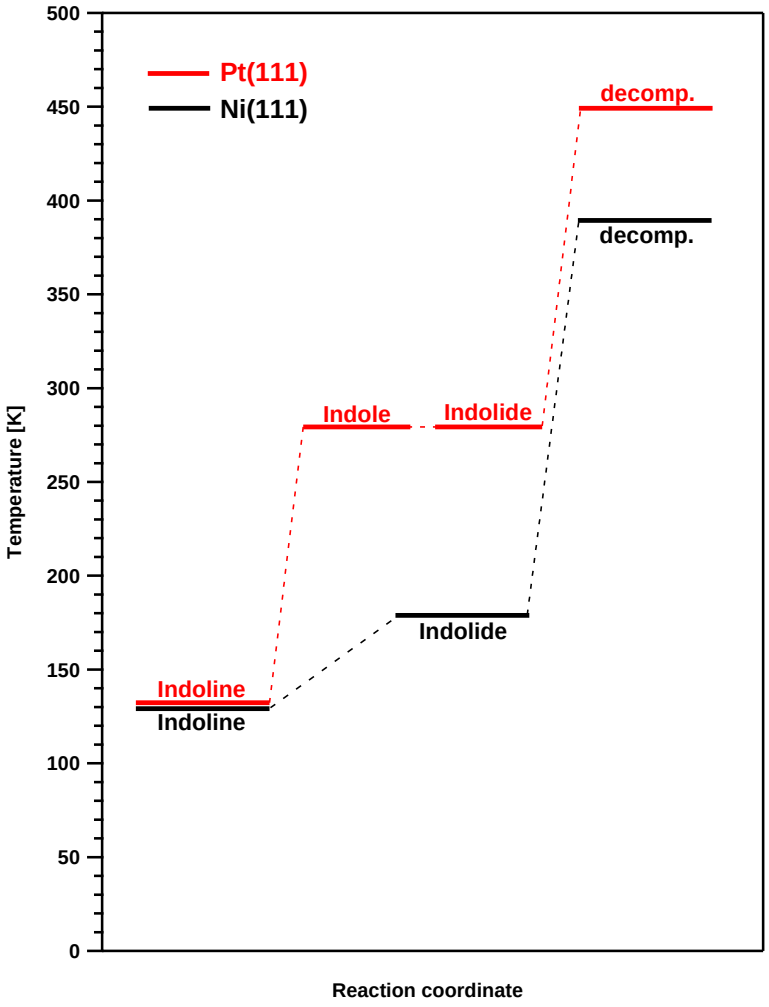

Figure A 2: Comparison between the reaction pathways of indoline on Ni(111) and Pt(111).

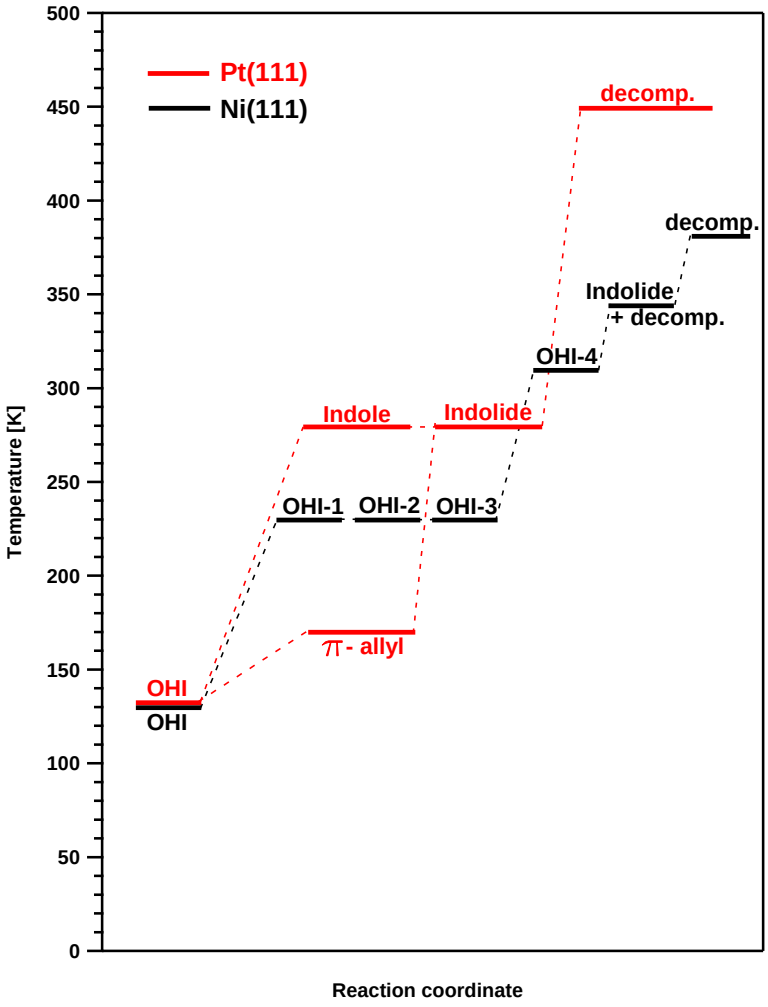

Figure A 3: Comparison between the reaction pathways of octahydroindole on Ni(111) and Pt(111).

Substance	C 1s signals [eV]	N 1s signals [eV]	O 1s signals [eV]	Surface
Indole	284.36, 285.04	400.25		**Ni(111)**
Indoline	284.17, 284.63, 285.36, 285.81	400.09		**Ni(111)**
Octahydroindole	284.80, 285.24	399.71		**Ni(111)**
Indole[A]	284.5, 285.4, 286.0	399.0		**Pt(111)**
Indoline[A]	284.3, 285.4, 285.9	399.5		**Pt(111)**
Octahydroindole[A]	284.4, 285.4	399.5		**Pt(111)**
2,2'-Bipyridyl	284.30, 284.84, 285.24	398.12		**Ni(111)**
2,2'-Bipiperidine	284.34, 285.06, 285.75	399.72		**Ni(111)**
Pyridine	284.25 284.89	398.12 (flat), 400.18 (upright)		**Ni(111)**
Piperidine	284.89, 285.51	399.62		**Ni(111)**
Pyrrole	284.40, 285.12	400.21		**Ni(111)**
Pyrrolidine	285.02, 285.60	399.69		**Ni(111)**
Furan	284.2, 285.1, 285.3		532.2	**Pt(111)**
THF	284.2, 285.5		532.3	**Pt(111)**
Benzofuran	284.2, 285.1, 285.5		532.5	**Pt(111)**
Dihydrobenzofuran	284.4, 285.7		532.4	**Pt(111)**

Table A 1: Binding energies of the presented LOHC compounds on Ni(111) and Pt(111) after adsorption at ~130 K. Experiments on Ni(111) are highlighted in blue and experiments on Pt(111) in orange.

*[A] Bachmann et al., Dehydrogenation of the Liquid Organic Hydrogen Carrier System Indole/Indoline/Octahydroindole on Pt(111). J. Phys. Chem. C **2018**, 122 (8), 4470-4479.*

Acknowledgements – Danksagung

Ich möchte mich an dieser Stelle bei allen Personen, die mich während der Dissertation begleitet und unterstützt haben, bedanken.

Großer Dank gilt insbesondere Prof. Hans-Peter Steinrück, der mir die Möglichkeit gegeben hat, in seinem Arbeitskreis diese Dissertation anzufertigen. Hervorzuheben ist sein stets respektvoller Umgang mit allen Kolleginnen und Kollegen, was Die Arbeitsatmosphäre im gesamten Arbeitskreis sehr angenehm gestaltet hat. Die Organisation aller Arbeitsabläufe im Arbeitskreis war hervorragend.

Einen großen Dank möchte ich auch an meinen Betreuer PD Dr. Christian Papp aussprechen. Dieser war die erste Anlaufstelle, wenn es um die Planung, Durchführung und Auswertung von Experimenten ging. Er lieferte viele wertvolle Ideen, wenn es um die Interpretation von Messdaten ging. Zudem war er jederzeit erreichbar und nahm sich auch an Wochenenden die Zeit, Daten und Ergebnisse mit einem zu diskutieren.

Dr. Philipp Bachmann danke ich für die Einarbeitung in die messtechnischen Anlagen der Synchrotron-Gruppe, die Arbeitsabläufe am Synchrotron und das Thema LOHCs im Allgemeinen. Er betreute bereits meine Masterarbeit und hatte bei technischen Problemen stets pragmatische und zum Teil unkonventionelle Lösungen parat.

Ein Dankeschön möchte ich an die Kollegen Dr. Udo Bauer, Dr. Florian Späth, Dr. Fabian Düll, Felix Hemauer, Marie Freiberger, Valentin Schwaab und Natalie Waleska aus der Synchrotron-Gruppe aussprechen, ohne die ein Gelingen dieser Dissertation nicht möglich wäre. Ihre Hilfe war bei der Arbeit am Synchrotron in Berlin unerlässlich. Nur im Team war es möglich, die Logistik und den Aufbau der Messinstrumente stemmen und die für diese Dissertation nötigen Experimente durchzuführen. Rund um die Uhr waren diese Kollegen am Synchrotron im Einsatz und wirkten bei allen Experimenten diszipliniert mit, selbst an Feiertagen und zum Teil trotz großer Müdigkeit während langen Nachtschichten.

Bedanken möchte ich mich auch bei unserem Elektroniker Hans-Peter Bäumler, der für die Wartung und Instandhaltung von Messinstrumenten jederzeit zur Verfügung stand. Überdies danke ich Herrn Bernd Kreß, der ein Experte auf dem Gebiet der UHV Komponenten ist und bei Umbaumaßnahmen oder Störungen immer der erste

Ansprechpartner war. Dank gebührt auch Herrn Friedhold Wölfel aus der Mechanikwerkstatt, welcher zahlreiche UHV-Komponenten gewartet und Ersatzteile in höchster Präzision angefertigt hat.

Meinen herzlichen Dank möchte ich meiner Familie aussprechen, die mich während der gesamten universitären Ausbildung unterstützt und motiviert hat. Большое спасибо!